# MECHANISTIC STUDY OF CYSTEINE DIOXYGENASE, A NON-HEME MONONUCLEAR IRON ENZYME

by

WEI LI

Presented to the Faculty of the Graduate School of
The University of Texas at Arlington in Partial Fulfillment
of the Requirements
for the Degree of

DOCTOR OF PHILOSOPHY

THE UNIVERSITY OF TEXAS AT ARLINGTON

August 2014

Acknowledgements

I would like to thank Dr. Pierce for your mentoring, guidance and patience over the five years. I cannot go all the way through this without your help. Your intelligence and determination has been and will always be an example for me.

I would like to thank my committee members Dr. Dias, Dr. Heo and Dr. Jonhson-Winters for the directions and invaluable advice.

I also would like to thank all my lab mates, Josh, Bishnu ,Andra, Priyanka, Eleanor, you all helped me so I could finish my projects.

I would like to thank the Department of Chemistry and Biochemistry for the help with my academic and career.

At Last, I would like to thank my lovely wife and beautiful daughter who made my life meaningful and full of joy.

July 11, 2014

Abstract

MECHANISTIC STUDY OF CYSTEINE DIOXYGENASE

A NON-HEME MONONUCLEAR IRON ENZYME

Wei Li, PhD

The University of Texas at Arlington, 2014

Supervising Professor: Brad Pierce

Cysteine dioxygenase (CDO) is an non-heme mononuclear iron enzymes that catalyzes the O2-dependent oxidation of L-cysteine (Cys) to produce cysteine sulfinic acid (CSA). CDO controls cysteine levels in cells and is a potential drug target for some diseases such as Parkinson's and Alzhermer's. Several crystal structures of CDO have been determined and they reveal a ferrous iron active site coordinated by three histidine residues. This feature is divergent from the monoanionic 2-histidine-1-carboxylate coordination typically observed within the non-heme mononuclear iron super family of oxidase/oxygenase enzymes. Furthermore, within 3.3 Å of the CDO active site iron is an unusual covalently crosslinked cysteine-tyrosine pair (C93-Y157). To date, only 3 other enzymes have been identified with a similar Cys-Tyr post-transitional modification and the role of this modification in CDO is still unknown. Due to the lack of structural evidence of oxygen-bound intermediates, the mechanism of CDO remains unclear. In this work, a transient intermediate $Fe^{III}$-superoxo was discovered by chemical rescue reaction and characterized using UV-vis, EPR and resonance Mossbauer. To probe the influence of second-sphere enzyme-substrate interaction, the steady-state kinetics and

$O_2$/CSA coupling were measured for wild-type CDO and selected active site variants (Y157F, C93A, H155A). In additional, using $CN^-$ as a probe, the influence of the C93-T157 pair to the active site is investigated on EPR. Key substrate-enzyme interaction was also investigated by substrate specificity of CDO. Selected thiol-containing compounds were incubated with CDO for steady-state kinetic analysis using NMR. LC-MS confirmed the presence of products and dioxygenase activity.

Table of Contents

List of Illustrations

List of Tables

List of Schemes

# Chapter 1

## Introduction of Non-heme Mononuclear Iron Enzyme and Cysteine Dioxygenase

Oxygen is the second abundant element in atmosphere, and it is essential for most of the organisms. Dioxygen is required in most of the bioprocesses in living cells such as respiration and biosynthesis in which many enzymes are involved. In human body, oxygen is transferred to where it is needed by metalloenzymes that are specifically designed to do that. (Hemoglobin and Myoglobin) Besides that, many metalloenzymes that are able to utilize molecular in biosynthesis and biodegradation have been created. These enzymes are incredibly versatile and catalyze a wide range of reactions from aliphatic desaturation to oxidative ring cyclizations [1].

Cysteine dioxygenase (CDO) is an enzyme that belongs to this non-heme mononuclear iron enzyme family. It was discovered about 40 years ago as the main enzyme that regulates cellular cysteine concentrations by converting cysteine to cysteine sulfinic acid[4]. Recently, considerable research effort has been focused on CDO due to implications in cellular sulfur metabolism and neurodegenerative disorders. Over the past decade, multiple high resolution crystal structures of mammalian CDO have been determined revealing a $\beta$-barrel fold typical of the cupin superfamily [2]. The active site coordination of CDO is comprised of mononuclear iron ligated by the N$\varepsilon$- atoms of His86, His88, and His140, representing a new facial triad variant [2]. While uncommon, deviations from the canonical 2-His-1-carboxylate motif are often observed within the cupin family of protein folds[3-5].

CDO also contains a covalently cross-linked cysteine-tyrosine cofactor (C93–Y157) within 3.3 Å of the iron active site. An analogous post-transcriptional modification has also been observed in the copper-radical enzyme, galactose oxidase [100]. Based on this similarity and the proximity of the C93–Y157 pair to the active site, it has been

proposed that a tyrosine radical may be generated during the oxidation of cysteine. However, there is currently no evidence for the role of this covalent modification.

Within the 2-His-1-carboxylate family of non-heme diiron enzymes a general mechanism for catalysis has emerged based on extensive spectroscopic and crystallographic characterization[4-6]. Based on this model, the reaction mechanism was proposed in which L-cysteine provides bidentate coordination to the ferrous site through the thiolate and amino groups and will be discussed later. This exact bidentate coordination was recently confirmed by co-crystallization of the enzyme in the presence of substrate [7]. The resulting distorted trigonal bipyramidal geometry of the substrate-bound active site places the carboxylate group of L-cysteine within hydrogen bonding distance (2.3 Å) to the guanidinium group of Arg60. This ternary interaction between L-cysteine and the enzyme active site effectively explains the high substrate specificity demonstrated by CDO. However, despite the availability of multiple crystal structures, mechanistic details and its significance to human health remain unresolved. To provide context to the work provided here, a survey of each of the five classes of non-heme mononuclear iron enzymes is provided in the following section.

## Mononuclear Non-heme Iron Containing Enzyme: The 2-His-1-carboxyglate Facial Triad

Most mononuclear non-heme iron containing enzyme utilized molecular oxygen as electron sources. According to the numbers of oxygen atoms transferred to substrate(s), they can be categorized as monoygenase or dioxygenases [5, 8-10]. There's also enzymes that oxidize substrate by reducing molecular oxygen to water molecules, such as isopenicillin N synthase which catalyzes a ring-closure reaction [11]. The mononuclear non-heme iron enzymes have drew the most attention because the explosion of available crystal structures available recently and the diverse reactions that

they are able to catalyze [3, 4, 12]. Studies on the structures of these enzymes have revealed a new common structural motif in which the metal is bound to two histidine residues and a carboxylic acid side chain of either a glutamate or aspartate residue [13, 14]. This special structure motif has been named the "2-His-1-carboxylate facial triad" (Figure 1.1). Very few exceptions are found in mononuclear non-heme iron containing enzymes that don't have this 2-His/1-carboxylate motif, such as the aliphatic halogenase enzyme (SyrB2) [15, 16] and the enzyme we are interested in, cysteine dioxygenase (CDO) [17-19], which will be discussed later.

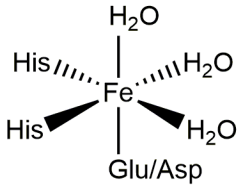


Figure 1-1 2-His/1-carboxylate motif.

*Obligated Substrate Binding and Oxygen-activating/substrate-activating Pathway*

Although the 2-His/1-carboxylate containing enzymes catalyze a wide range of reactions, there are some common mechanistic features shared by all of them [3-5, 20]. First, resting state of the enzyme has a six-coordinate metal center and is normally unreactive towards dioxygen. The subsequent binding of substrate and/or cofactor results in the formation of an unsaturated, five-coordinate metal center, which is able to bind and activate molecular oxygen [20]. This obligated binding of oxygen is a protective mechanism for the enzyme to avoid self-oxidation/self-inactivation. From the point the oxygen bound to the iron center, proposed mechanism for different enzymes diverge [5]. In most cases, the O-O bond is broken and a high-valent iron-oxo(IV or V) specie is formed. The high-valent iron-oxo species is proposed to be the actual oxidizeing species. The direct evidence for the existence of the high-valent iron-oxo species has

been reported for taurine/α-ketoglutaruate dioxygenases (TauD) [21, 22], prolyl-4-hydorxylase (P4H) [23], and halogenase CytC3 [24]. In the other proposed mechanism, there's no high-valent iron-oxo species involved. Instead, an iron(III)-superoxide species is generated and considered as the oxidizing species. For example, isopenicillin N synthase (IPNS) undergoes such a mechanism which is normally noted as the "substrate-activating" mechanism. In this case, the formation of the dioxygen bridged binding and the subsequent high-valent iron-oxo species is prevented by the formation of the superoxide which is stabilized by the thiolate-bound substrate [25].

## Enzyme Groups that Contain the 2-His-1-carboxylate Facial Triad

### *α-Ketoglutarate-dependent Enzymes*

This is the largest subfamily of non-heme iron containing enzymes with the 2-His/1-caboxylate motif and they have been studied extensively [4]. They utilize α-ketoglurarate (2-oxoglurarate) as a cofactor to catalyze the oxygen dependent oxidation of substrate (Scheme 1-1). α-ketoglurarate is converted to carbon dioxide and succinate by oxidative decarboxylation [4]. This subfamily are very versatile and catalyze a wide range of reactions in biosystems. Reactions include substrate hydroxylation, substrate halogenation, desaturation, ring closure/expansion and many more others. These enzymes are involved in DNA/RNA repair, oxygen sensing, transcription regulation and the biosynthesis of antibiotics [4]. The most common reaction for the subfamily of enzymes is substrate monoxygenation to give hydroxylated products performed by the α-ketoglurarate dependent dioxygenases (α-KDD). α-ketoglurarate dependent halogenases (α-KDH) which couples decarboxylation of α-ketoglurarate with substrate halogenation share a similar function and catalytic mechanism with α-KDD.

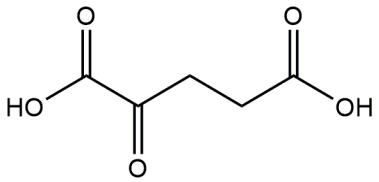


Scheme 1-1 Structure of α-ketoglurarate.

Mechanism

The mechanism of the α-ketoglurarate dependent oxygenases has been studied and understood well [26, 27]. In the ferrous iron resting state, the metal is coordinated by two histidine residues and a carboxylic acid side chain (Asp/Glu), leaving The opposite octahedral face of the meatal coordination sphere vacant. Bidentate coordination of the α-ketoglurarate (α-KG) cosubstrate leaves one open site for $O_2$-coodination following substrate binding. Substrate binding in the α-ketoglurarate dependent oxidases is unique compared to other enzymes. In these enzymes, the substrate doesn't bind directly to the metal. Instead, it binds within the active site near the metal. However, upon substrate binding, a coordinated water molecule is displaced opening up a coordination site for molecular oxygen. Rapid charge transfer between the reduced iron and the bound oxygen molecule result in formation of a ferric-superoxo species. A bicyclic ring-structure is formed as the results of the attraction to the α-keto position of α-KG by the terminal oxygen atom of the superoxo intermediate. Subsequent cleavage of the dioxygen O-O bond releases carbon dioxide and produces succinate and a high-valent iron (iv)-oxo species. Hydrogen atom abstraction from the substrate gives rise to a Fe(III)-hydroxo species with a bound substrate radical. Rapid rebound of the hydroxyl group with the substrate radical produces the hydroxylated product and returns the enzyme to its resting ferrous oxidation state. Product is released from the metal center completes the catalytic cycle (Scheme 1-2).

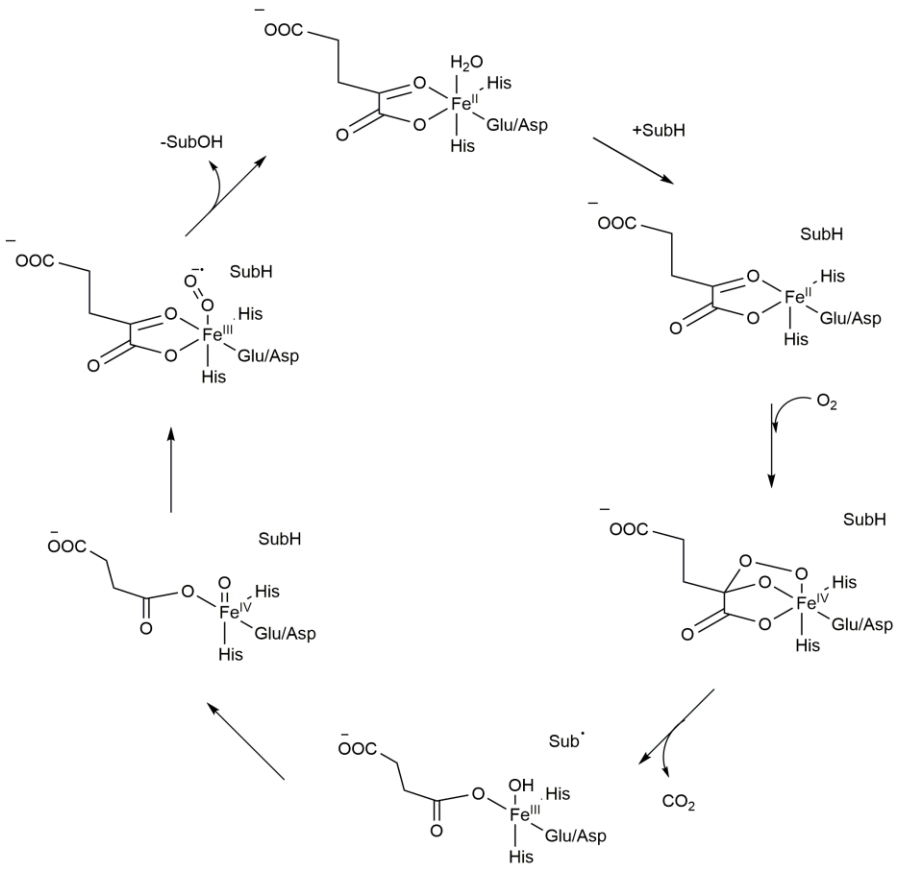


Scheme 1-2 Propose mechanism for α-Ketoglutarate dependent dixoygenase.

*Taurine/α-Ketoglutarate Dioxygenase (TauD).* TauD is probably the most extensively studied mononuclear non-heme iron dioxygenase.TauD catalyzes the $O_2$ dependent oxidation of taurine and alpha-ketogluterate to produce inorganic sulfite, aminoacetaldehyde, and succinate (Scheme 1-3) [28]. The existence of the high-valent iron (iv)-oxo intermediate has been confirmed by Mössbauer, resonance Raman and X-ray absorption spectroscopy [22, 29, 30]. TauD was considered as the template for mononuclear non-heme iron enzymes and has inspired many studies.

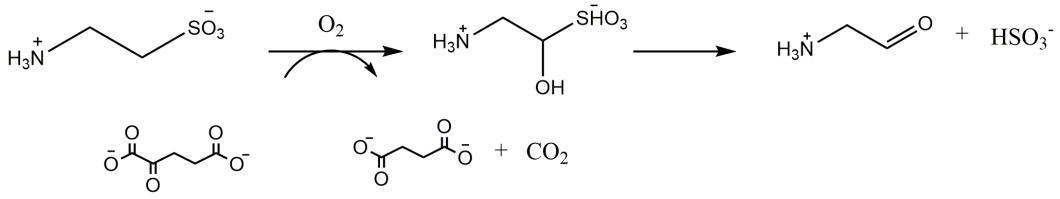

Scheme 1-3 Reaction catalyzed by TauD.

*AlkB Repair Enzymes.* AlkB repair enzymes have been identified to belong to the α-ketoglurarate dependent dioxygenases family recently [31, 32]. These enzymes are able to repair DNA/RNA bases that are methylated by intra- or extracellular alkylating agents (Scheme 1-4). For example, $N^3$-methyladenine is a common methylation product which is generated by compounds such as methyl methanesulfonate and methyl halides. DNA damages by methylation blocks replication by preventing the formation of Watson-Crick base-pairing. This can have significant consequences physiologically and thus AlkB catalyze the remove of the methyl group from the $N^3$-methyladenine-containing DNA [33]. Human AlkB repair enzymes have been characterized and repair methylated and ethylated DNA strands and release formaldehyde and acetaldehyde, espectively [34]. X-ray crystal structures of these enzymes demonstrate that this family of enzymes belongs to the α-KD-dependent dioxygenase enzymes which contain a mononuclear ferrous iron site coordinated by a 2-His/1-Asp facial triad motif [35]

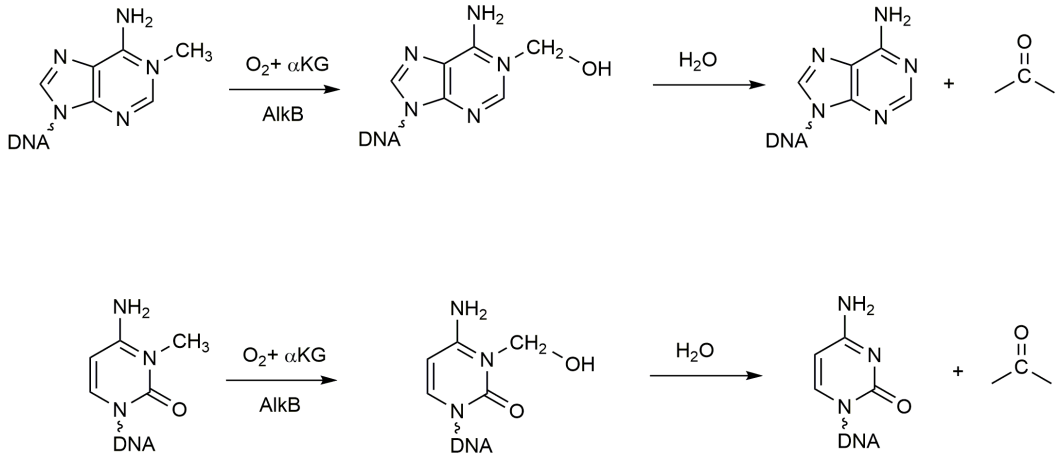


Scheme 1-4 Reactions catalyzed by AlkB.

*Prolyl-4-hydroxylase (P4H).* Another well characterized α-ketoglurarate dependent dioxygenase is prolyl-4-hydroxylase (P4H). This enzyme is involved in the hydroxylation of proline groups on the $C^4$ position (Scheme 1-5) [36]. These enzymes are utilized in the cross-linking of collagen helices and the cellular response to hypoxia through the hypoxia inducible factor (HIF) [37-40]. Repeated triads of proline-proline-glycine exist in the cross-linking strand in collagen. The second amino acid residue of this repeated triads, proline, is often hydroxylated by P4H [41]. The inhibition of P4H has been shown could protect against neurotoxicity, which makes it a potential target for the treatment of Parkinson's disease [42].

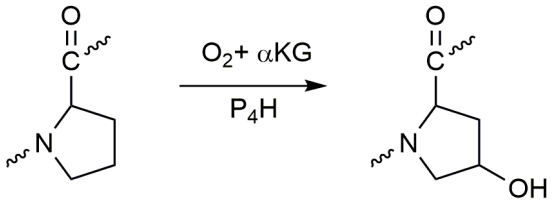


Scheme 1-5 Reaction catalyzed by P4H.

*Extradiol and Intradiol Dioxygenase*

Catechol, an intermediate on bacterial aromatic degradation pathway is oxidatively cleaved by extradiol dioxygenases and intradiol dioxygenases [43, 44]. Extrodiol dioxygenases cleaves the C-C bond next to the two hydroxyl groups while intradiol dioyxgenases cleaves the C-C bond between the two hydroxyl groups [4, 5]. In both cases, both atoms of the molecular oxygen are incorporated into the substrate. Although catalyzing similar reactions, the metal at their active sites have different oxidation states. In extradiol dioxygenases, a non-heme iron (II) center is present while in intradiol dioxygenases, a Fe(III) iron is utilized [45]. Of the two class of enzymes, extradiol dioxygenases exhibit greater diversity in the accommodation of substrates. For example, they can frequently accommodate non-native substrates other than catechol, such as salicylate, hydroquinone, gentisate and 2-aminophenol [46].

Extradiol dioxygenases

As illustrated in (Scheme 1-6), the extradiol dioxygenases catalyze the oxidatively cleavage of the C-C bond next to the two hydroxyl groups to give a 2-hydroxymuconaldehyde product using ferrous iron as a cofactor. They have a 2-His/1-Glu motif at the active site and the substrate bidentately binds to the iron as a monoanion ligand. Molecular oxygen then binds to initiate the enzymatic reaction [47].

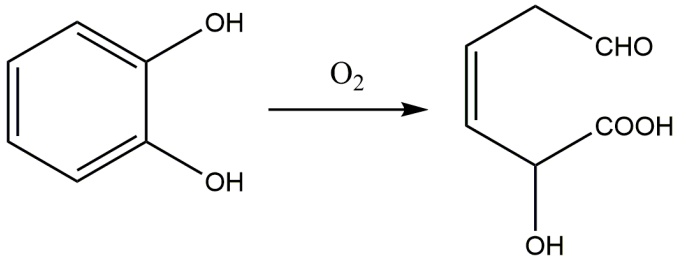


Scheme 1-6 Reaction catalyzed by extrodiol dioxygenases.

Studies indicate that unlike α-ketoglurarate dependent dioxygenases, extradiol dioxygenases undergo the “substrate-activating” mechanism and there’s no high-valent iron-oxo species involved. It’s proposed that the iron (III)-superoxide and generated and the substrate is activated as a semiquinone radical [48]. Evidence for this semiquinone radical has been obtained using substrate analogues. Superoxide attacks the activated substrate and the formation of the C-O bond gives a proximal hydroperoxide intermediate. This intermediate has been directly observed in the crystal structure of homoprotocatechuate 2,3-dioxygenase (2,3-HPCD) when a substrate analogue 4-nitrocatechol is present [49]. Then the proximal hydroperoxide undergoes Criegee rearrangement and generates a seven-membered α-keto-lactone intermediate. $^{18}O$ labeling studies on 2,3-dihydroxyphenylpropionate 1,2-dioxygenase (MhpB) was used to demonstrate the presence of this intermediated [50]. This seven-membered ring is then hydrolyzed to give the final product (Scheme 1-7).

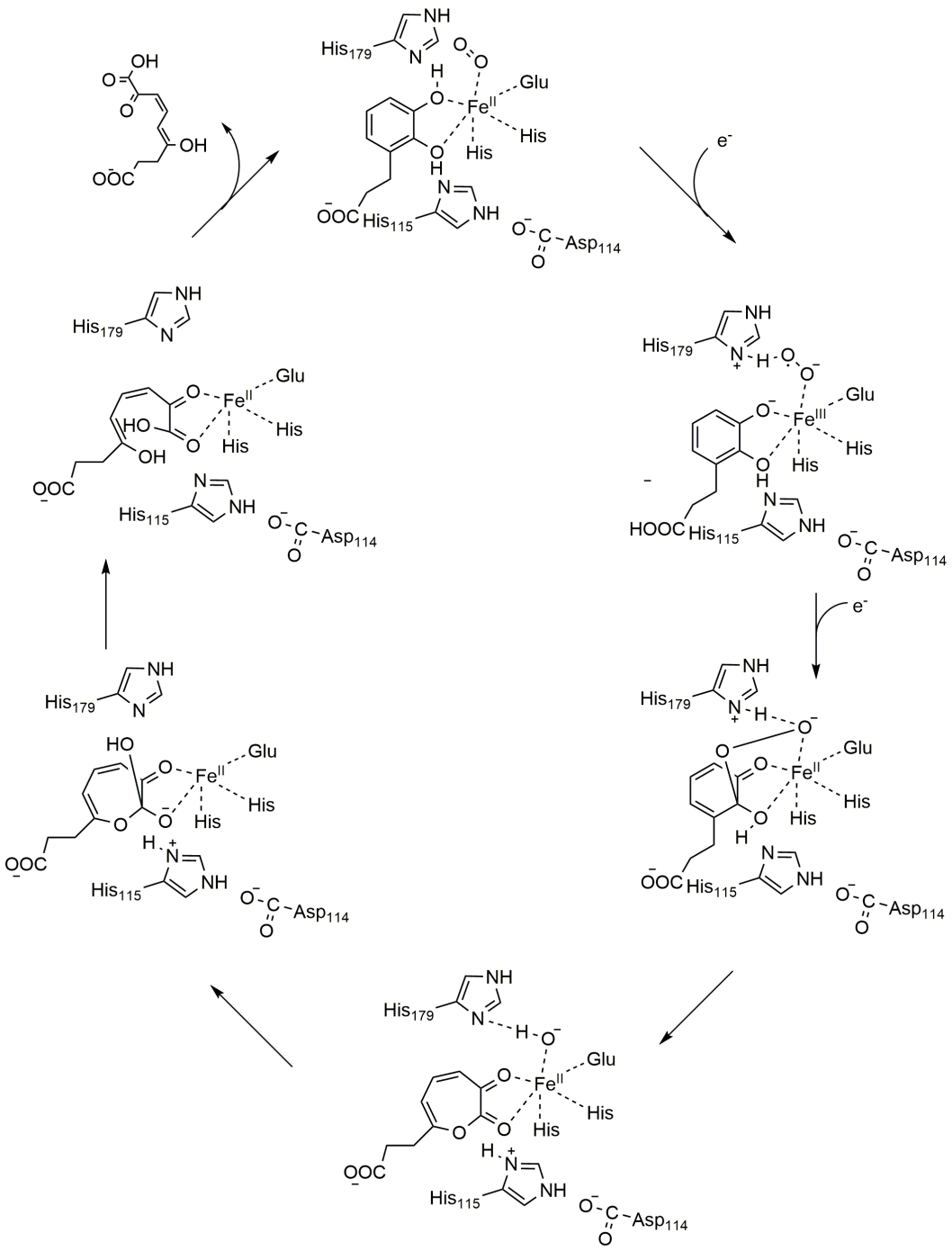


Scheme 1-7 Proposed mechanism for extradiol dioxygenases (numbering for *Escherichia coli* MhpB).

Intradiol dioxygenases

Unlike extrodiol dioxygenases, in the resting state the active site of intradiol dioxygenases contain an unusual 2-His/2-Tyr motif with a ferric iron incorporated where the carboxylic acid amino acid (Asp/Glu) is replaced by a tyrosine residue [51]. Also, differs from extrodiol dioxygenases, substrate binds the ferric iron as a semiquinone instead of a monoanion [52]. Upon the binding of substrate, the axial tyrosine and water ligand are replaced and the bidendate substrate complex is formed with a 2-His/1-Tyr motif [53, 54]. Molecular oxygen does not bind to iron initially, instead, it reacts with the semiquinone and forms a hydroperoxide intermediate to initiate the enzymatic reaction. The transient hydroperoxide species is believed undergoes a Criegee rearrangement to give the final product [55].

However, recent studies provided evidence that the hydroperoxide intermediate may undergo a mechanism involving O-O bond hemolysis instead of a Criegee rearrangement (Scheme 1-8) [56].

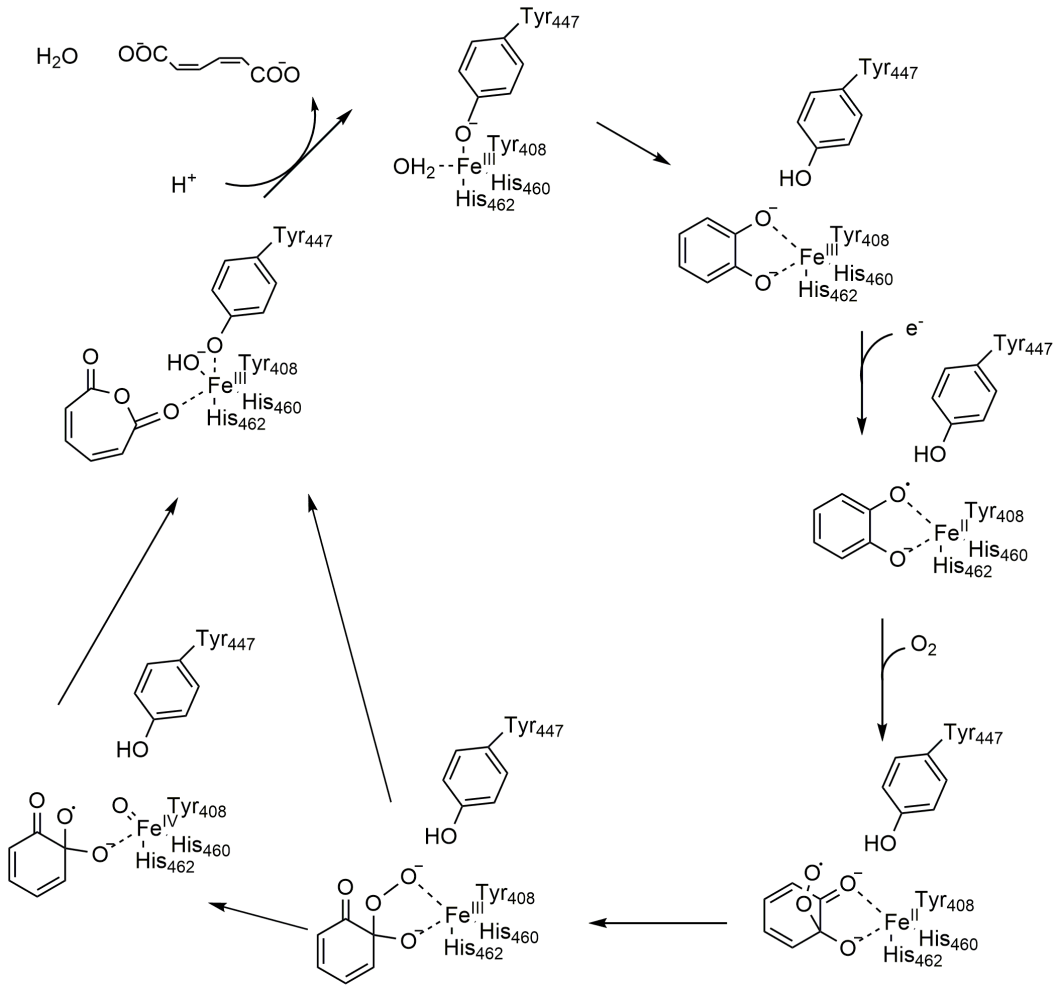


Scheme 1-8 Proposed mechanism for intradiol dixoygenases (numbering for 3,4-PCD).

*Rieske Dioxygenases*

Aromatic hydrocarbons are one of the major contaminants in soil and groundwater. Aromatic ring cleavage represents a significant thermodynamic barrier resulting in their high environmental persistence. However, Rieske dioxygenases or aromatic dihydroxylating dixoygenases found in soil bacteria are able to catalyze the efficinet *cis*-dihydroxylation of arene substrates with a high turnover number, resulting in

an efficient pathway for the biodegradation of aromatic compounds [4, 44]. Given the importance in environmental and biocatalytic functions, much research has been done to this class of enzymes. Indeed, some Rieske dioxygenases have been identified that are capable of catalyzing a varieity of useful oxidation reactions such as sulfoxidation, desaturation, monohydroxylation, O- and N- dealkylation and amine oxidation (Scheme 1-9) [4, 57-60].

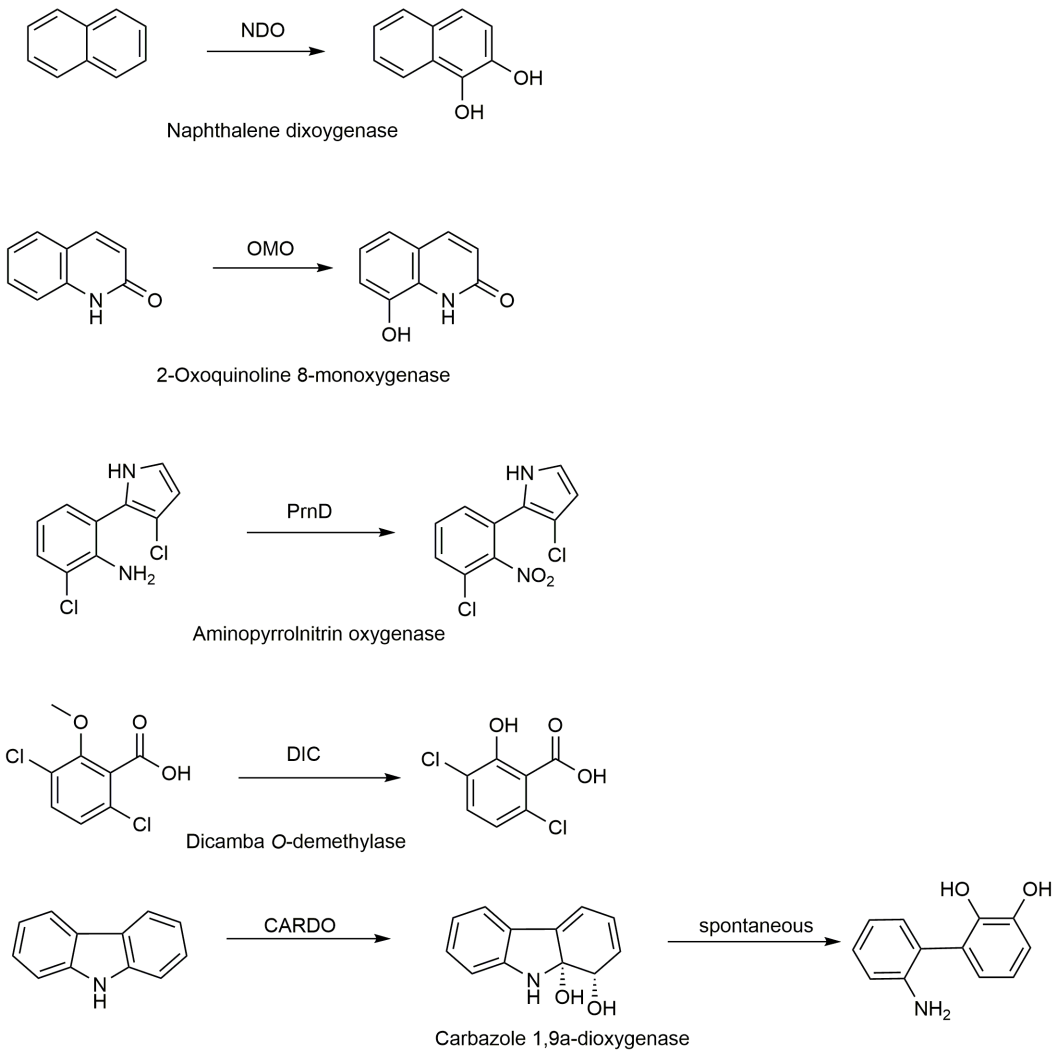


Scheme 1-9 Different reactions catalyzed by Rieske dioxygenases.

In contrast to the other mononuclear iron dioxygenases mentioned above, the Rieske dioxygenases are typically comprised of multiple protein components. Generally speaking, Rieske dioxygenases contain an oxygenase component, a reductase component and in some instances, a ferredoxin component [61-64]. The oxygenases component has the mononuclear non-heme iron active site and a Rieske-type [2Fe-2S] cluster located nearby. Two external electrons provided by a nicotinamide adenine nucleotide (NAD(P)H) cofactor are shuttled via the [2Fe-2S] cluster to the active site for the reaction to complete. Within the same subunit, the Rieske cluster is too far from the mononuclear iron site (~ 45 Å) for electron transfer to occur. However, the distance from the cluster to the center iron in the adjacent subunit is only 12 Å and they are bridged by an aspartic acid residue which is ascribed to be involved in the electron transfer between the [2Fe-2S] cluster and the center iron. Single point mutation of the aspartic acid resulted in the loss of catalytic activity [65-67].

Naphthalene dioxygenase (NDO)

Naphthalene dioxygenase is the most studied enzyme in the Rieske dioxygenase family [68, 69]. It contains a Rieske oxygenase component which has both a mononuclear iron(II) active site and two [2Fe:2S] clusters, an NADH-dependent flavorprotein reductase component and a ferredoxin component that contains two [2Fe:2S] iron-sulfur clusters (Scheme 1-10).

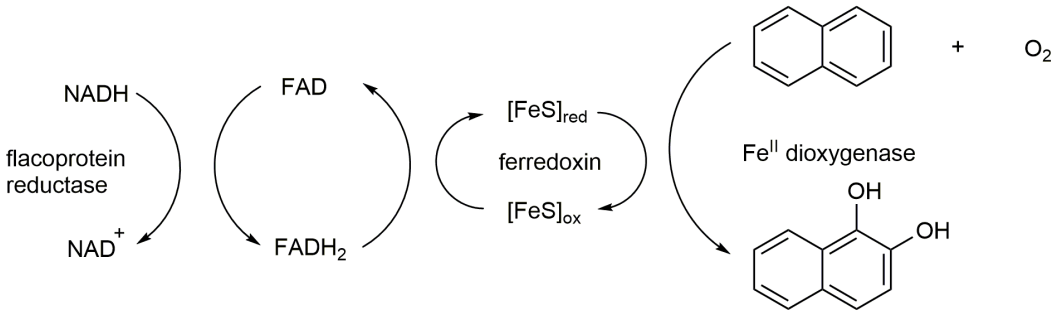


Scheme 1-10 Electron transfer in NDO.

X-ray crystal structures demonstrate that the active site 2-His/1-Asp motif within NDO enyzmes is slightly deviant as compared to other non-heme mononuclear iron enyzmes. Within the active site of NDO enzymes, the aspartic acid residue exhibits a bidentate coordination to the iron center [69]. Furthermore, the Aryl substrate does not directly bind to the iron site. Instead, substrate binding occurs 5-6 Å away from the mononuclear iron site. Oxygen binding is controlled by both substrate binding and by the redox state of the Rieske cofactor. Substrate binding leads to the conversion of active site from six-coordinate to five-coordinate, which leaves a coordination site for oxygen to bind [20]. Reduction of the Rieske cluster results in the conformational at the active site and opens a channel for oxygen to come in and bind. Another usual feature of NDO enyzmes is that unlike the more common end-on coordination, molecular oxygen binds to the iron center side-on ($\eta^2$) to yield a Fe(III)-( $\eta^2$-hydro)peroxide complex [68]. Different mechanisms have been proposed for how this enzymatic reaction proceeds. On the basis of computational modeling, direct attack of the iron(iii)-(hydro)peroxide on the substrate leads to the formation of an arene radical, followed by the transfer of second oxygen to the substrate, which is favored by the computational studies [65]. Alternatively, the O-O bond cleavage could lead to the formation of a high valent HO-Fe(v)=O intermediate which could then oxidize substrate and leads to the formation of final

product [70]. Support for this later mechanism has been provided by selected isotope labelling experiments (Scheme 1-11) [4].

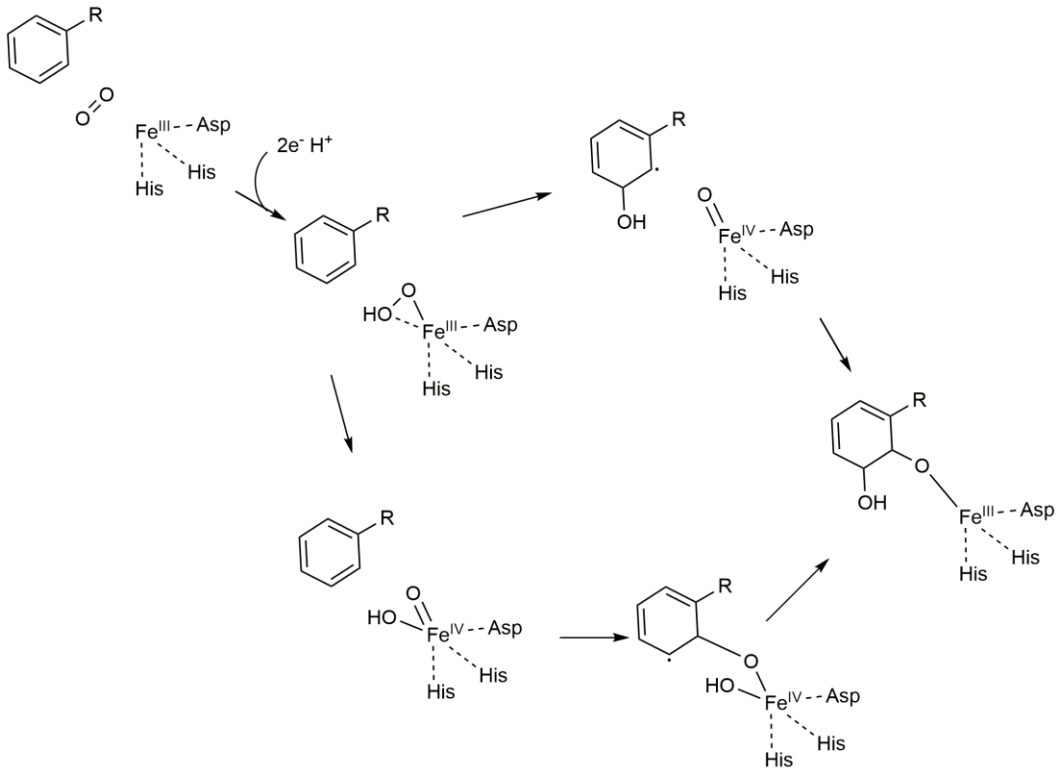


Scheme 1-11 Proposed mechanism for NDO.

*Pterin-dependent Hydroxylases*

A small subset of non-heme mononuclear iron enzymes that requires a tetrahydrobiopterin ($BH_4$) as a cofactor to hydroxylate aromatic amino acids (Figure 1-2, Scheme 1-12) [4, 12]. Members of this essential enzyme family include phenylalanine hydroxylase (PheH), tyrosine hydroxylase (TyrH) and tryptophan hydroxylase (TrpH). These enzymes are involved in the biosynthesis of essential amino acids and represent the initial step in the biosynthesis of catecholamine neurotransmitters. For example, PheH, TYRH, AND TRPH catalyzes the biosynthesis of tyrosine, 3,4-

dihydroxylphenylalanine (DOPA), and 5-hydroxytrptophan (A serotonin precursor), respectively. These three enzymes have received much attention since they are implicated in several neurological and physiological disorders [4, 12, 29]. X-ray crystal structures of these enzymes show that they share similar structures especially at the active site. All enzymes in this family contain the typical 2-His/1-carboxylate facial triad with an Fe(II) metal center and three water molecules bound in the resting state [71-73]. Studies also indicate that these three enzymes work via the similar mechanism [74].

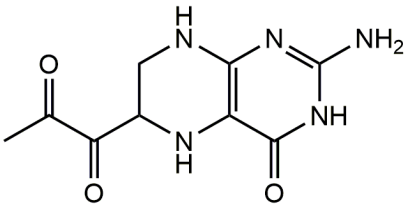

Figure 1-2 Structure of tetrahydrobiopterin

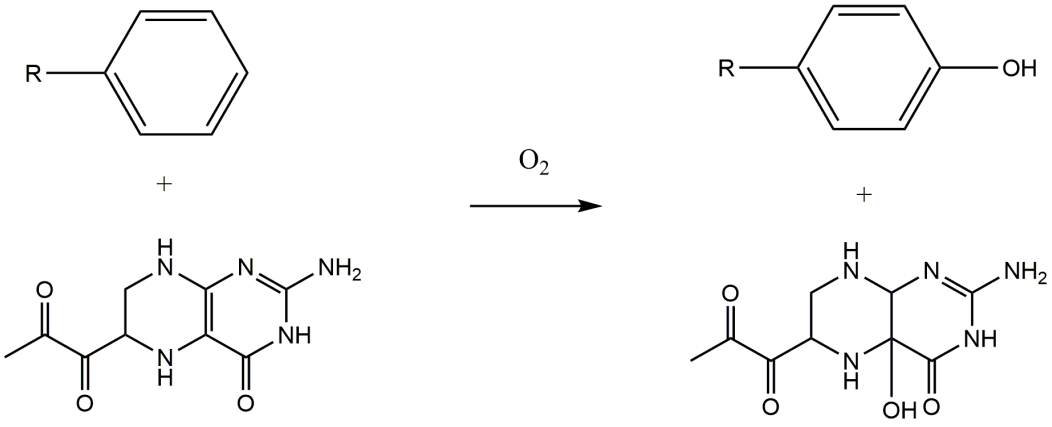

Scheme 1-12 Reaction catalyzed by Pterin-dependent hydroxylases.

Phenylalanine hydroxylase (PheH)

Unlike TryH and TrpH, which are only found in eukaryotes, PheH has also been identified in prokaryotes [4]. In contrast to other subfamilies, neither the substrate (aromatic amino acid) nor the cofactor ($BH_4$) binds directly to the Fe [75]. Upon pterin

and substrate binding, large conformational change occurs to facilitate the $O_2$-binding. In the resting state, it has a typical 2-His/1-Glu first coordination sphere is observed surrounding the mononuclear iron site. In this state , the Glu-coordination takes on the typical monodentate coordination. However, substrate induces a conformational change resulting in a bidentate coordination of the Glu residue to the Fe-site. It has also been proposed that bound water molecules are displace upon substrate binding, opening up a coordination site for molecular oxygen and moving the pterin cofactor closer to the active site [76].

In the propose mechanism, oxygen binds to the substrate/cofactor-bound PheH and forms a putative pteringperoxo-iron(ii) intermediate [74]. The O-O bond breaks heterolytically and gives rise to a reactive iron(iv)-oxo intermediate. This high-valent iron-oxo species then attacks the substrate and produces a cationic intermediate. The final product is formed through NIH-shift and tautomeriztion (Scheme 1-13).

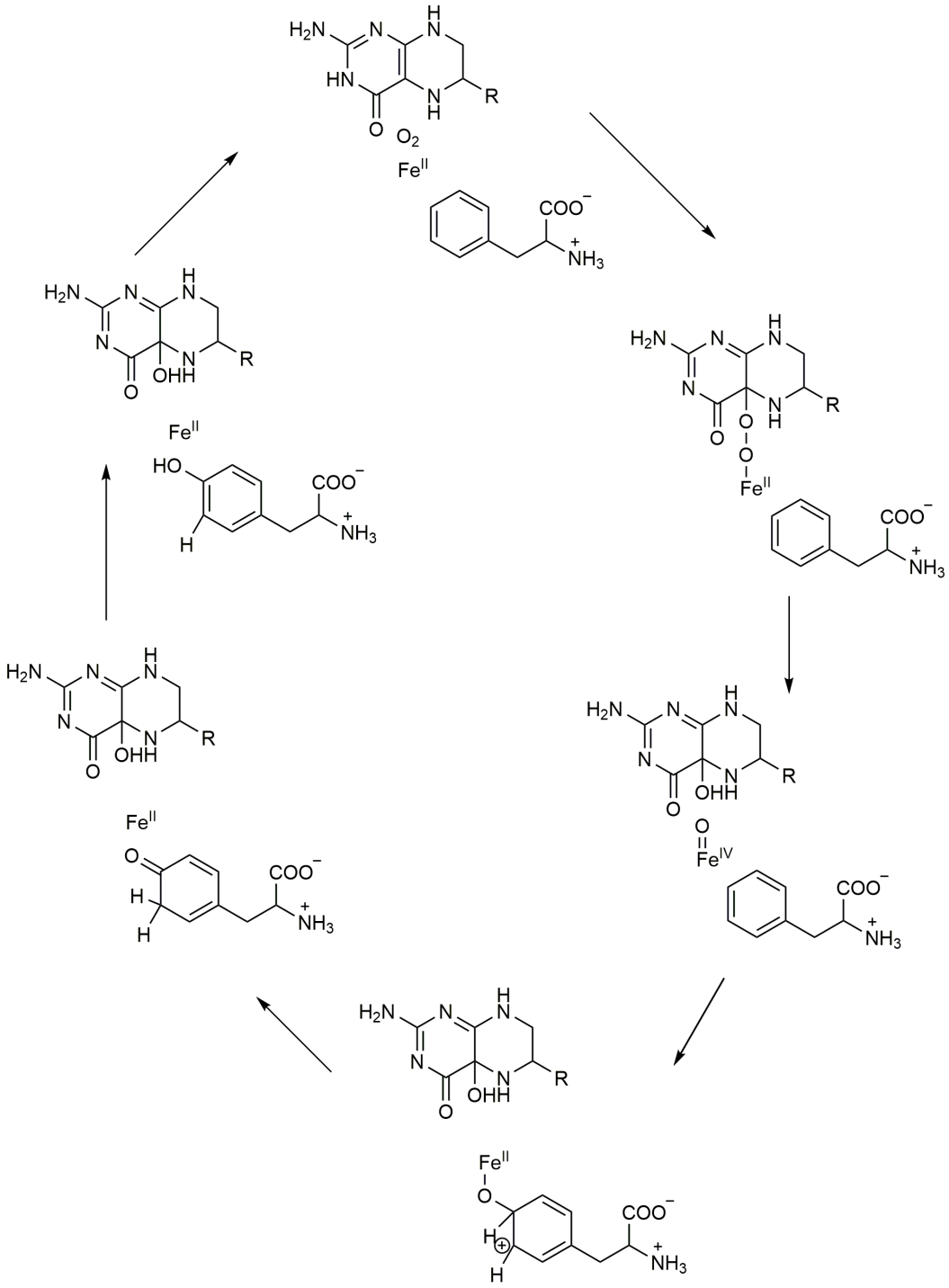

Scheme 1-13 Proposed mechanism for PheH.

*Isopenicillin N Synthase (IPNS) and 1-aminocyclopropane-1-carboxylic Acid Oxidase (ACCO)*

Among the mononuclear non-heme iron enzymes, there are enzymes that don't fall in any of the mentioned subclasses based on their requirements for catalysis. Isopenicillin N synthase (IPNS) and 1-aminocyclopropane-1-carboxylic acid oxidase (ACCO) are two examples that have been studied.

Isopenicillin N Synthase (IPNS)

Isopenicillin N Synthase (IPNS) is a mononuclear non-heme enzyme found in fungi and bacteria that converts the tripeptide δ-(L-α-aminoadipoyl)-L-cysteinyl-D-valine (AVC) to the bicyclic isopenicillin N (IPN), the precursor of all penicillins and cephalosporins, through an oxidative ring closure reaction (Scheme 1-14) [77]. It has the typical 2-His/1-Asp motif with a ferrous iron coordinated at the active stie [78]. Although IPNS shows a high sequence homology to the α-ketoglurarate dependent dioxygenases discussed above, it neither requires α-ketoglurarate as a cofactor to provide electrons to function, nor incorporates molecular oxygen atoms to the product. The electrons needed to reduce oxygen to water are all provided by the substrate [4].

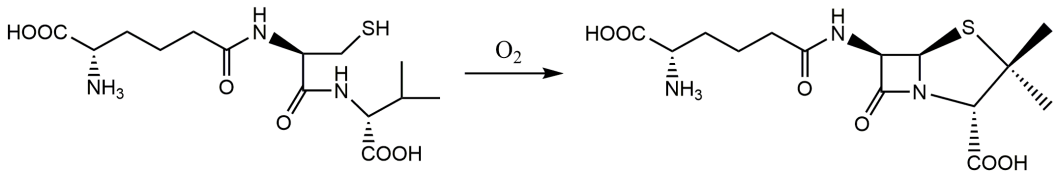


Scheme 1-14 Reaction catalyzed by IPNS.

In the study of IPNS, nitric oxide (NO) is often used as a non-reactive surrogate for oxygen to investigate the mechanism. Crystal structures that may representing intermediated in different stages have been identified [78-80]. Based on the information provided by the available structures, a mechanism was proposed [11]. In the first step of

this proposed mechanism, AVC binds the iron center via the thiolate. Molecular oxygen then binds the iron in the end-on fashion and forms a Fe(III)-superoxide intermediate which is stabilized by the bound substrate. This Fe(III)-superoxide intermediated transforms to an iron(IV)-peroxide species and attracts a hydrogen from the carbon next to the sulfur forming an iron(II)-hydroperoxide intermediate. The iron(II)-hydroperoxide attracts another hydrogen from the nitrogen resulting in the first ring closure and the formation of a high-valent iron(IV)-oxo species. The high-valent iron(IV)-oxo species attacks the carbon, producing a substrate radical and subsequently the oxidatve closure of the thiazolidine ring (Scheme 1-15).

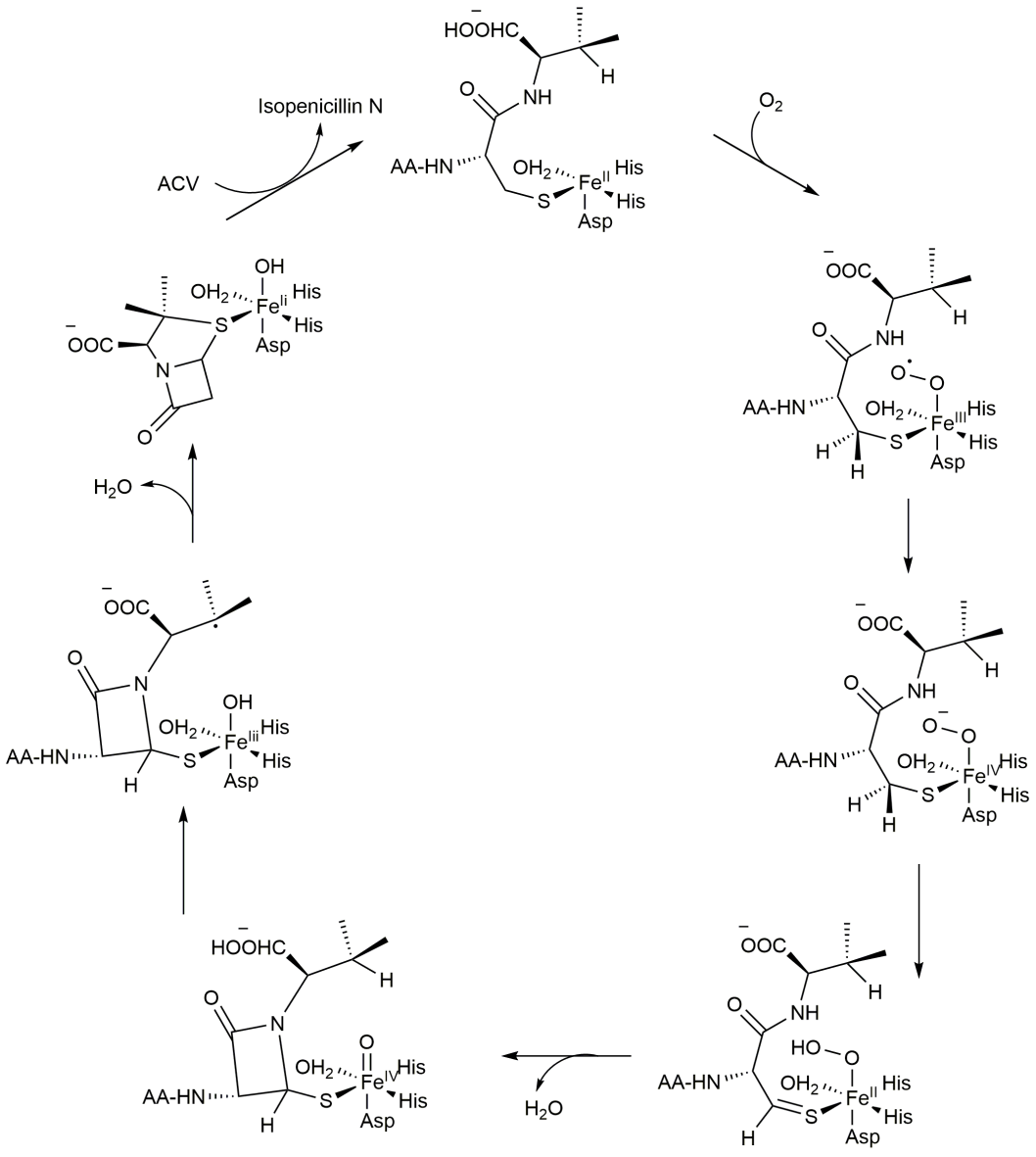


Scheme 1-15 Proposed mechanism for IPNS.

1-aminocyclopropane-1-carboxylic acid oxidase (ACCO)

Another enzymes that doesn't fall in any of the subfamilies mentioned above is 1-aminocyclopropane-1-carboxylic acid oxidase (ACCO). This enzymes catalyzes the final step in the ethylene biosynthesis in plants (Scheme 1-17). Ethylene is a plant hormone

that participates and regulates in many stages of plant growth and development, such as responses to environmental stress and fruit ripening. ACCO converts the unusual amino acid 1-aminocyclopropane-1-carboxylic acid (ACC) to ethylene, $CO_2$ and HCN while reducing dioxygen to two water molecules [81]. Like IPNS, ACCO also has the common 2-His/1-Asp motif coordinating a iron(II) at the active site. And ACCO also shows high sequence homology to α-ketoglurarate dependent dioxygenases but neither requires α-ketoglurarate as a cofactor nor incorporate oxygen atoms to final product [82]. However, the presence of both ascorbate and bicarbonate, which do not bind to the center iron, are required for this enzyme to function [83]. Study indicates that bicarbonate stimulates catalysis of ACCO and protects it from oxidative deactivation [83], while Ascorbate must present to convert the Fe(ii) site from six- to five-coordinate so oxygen could bind [83], presumably binds at a specific (remote) effector site to facilitate oxygen binding (Scheme 1-16).

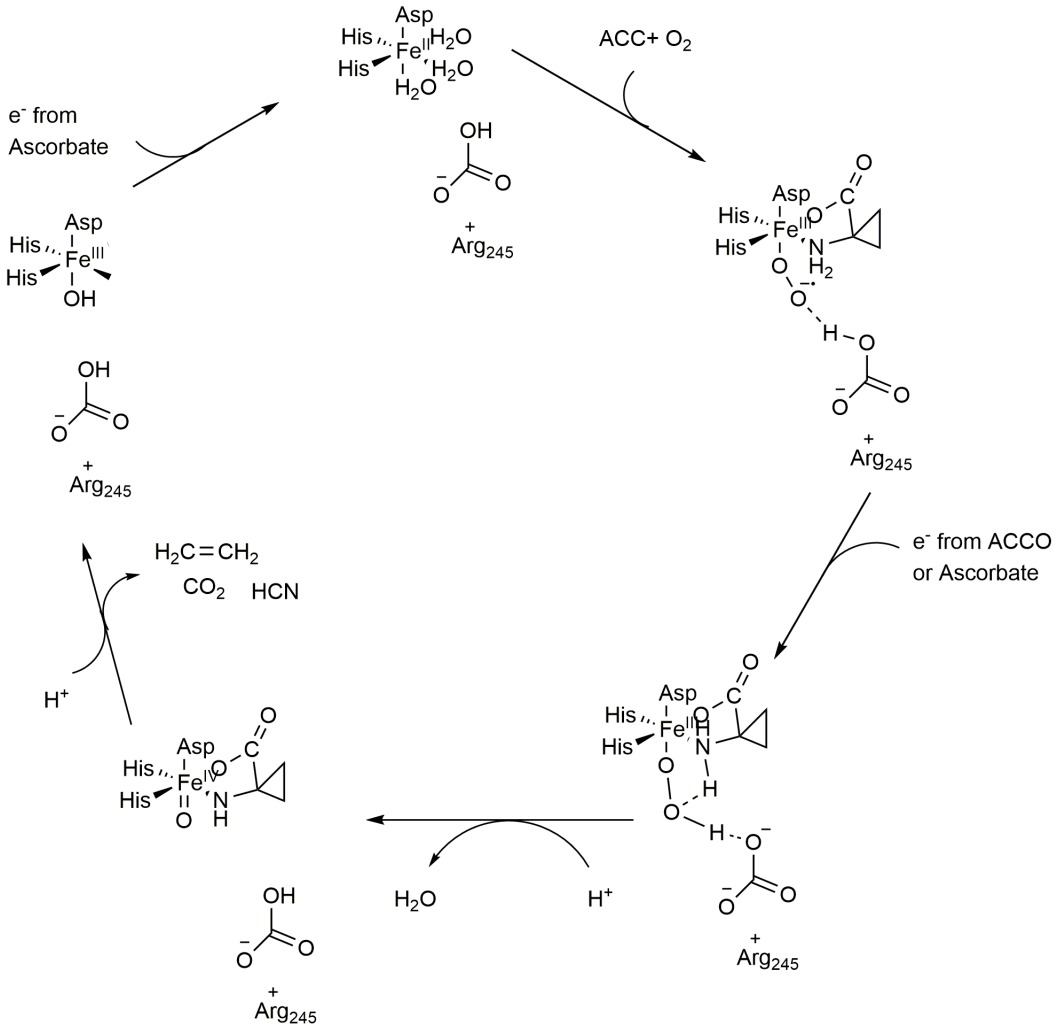


Scheme 1-16 Reaction catalyzed by ACCO.

Due to the lack of crystal structures and complexity of the system, the mechanism for ACCO is not fully understood [84, 85]. Based on a single-turnover study, a mechanism was proposed [83]. In this mechanism, substrate (ACC) displaces two water molecules and bidendate binds to the iron with its amine and carboxylate groups. Dioxygen binds to iron and forms a Fe(III)-superoxide intermediate. One electron transferring from ascorbate leads to the formation of Fe(III)-hydroperoxide. Abstraction of

a hydrogen atom from the amine by the Fe(III)-hydroperoxide produces a nitrogen radical. Rapid radical rearrangement happens next and result in ring cleavage and product formation.

## Cysteine Dioxygenase

### *L-Cysteine*

Sulfur is one of the essential elements in all living cells. In human beings, sulfur is mainly present in methionine and cysteine, two sulfur containing amino acids out of the twenty common amino acids. Sulfur containing compounds play important roles in human bodies. They are utilized in many ways to accomplish cellular needs. In addition to basic building blocks for proteins, sulfur containing compounds also serve as redox-active signaling molecules and cofactors to protect cells from reactive oxygen species [86]. When involved in redox chemistry, sulfur normally presents in the form of thiols or part of the inorganic iron-sulfur cluster in proteins such as ferrodoxins which serve as electron shuttles in cells [87].

Many of the sulfur containing compounds in eukaryotic organisms are products from cysteine metabolism. In humans beings, cysteine is either digested from food or synthesized from methionine [86]. The most important role of cysteine is as the building block of primary structures in proteins. The thiol groups of cysteine have pKa values close to neutrality when incorporated in proteins, so normally they are in the thiolate form, which is highly reactive and are easily oxidized. The thiol group of cysteine is used to carry out a variety of biologic functions due to this high reactivity [86, 88]. Disulfide bond can be formed between cysteine residues during protein folding and the reaction is catalyzed by protein disulfide isomerases. The formation of these covalent bonds are critical for proteins to fold properly and they also provide toughness and rigidity to the protein structure. Cysteine thiolate group often serves as an anchor for different

functional groups, such as flavin factors as well as iron sulfur clusters and metals such as iron, zinc, copper and manganese in metalloenzymes.[89] Besides, in the catalytic mechanism of many enzymes, cysteine residue also acts as general acids or bases and is able to stabilize both cationic and anionic intermediate depending on the pKa of the thiol group [90].

In human beings, cysteine is synthesized by the transferring of sulfur atom derived from methionine to the hydroxyl group of serine [86]. Methionine is converted to S-adenosylmethionine (SAM) in the presence of adenosine triphosphate (ATP) by methionine adonosyltransferase. SAM is the major methyl group donor and many methyltransferases utilize it as the cofactor to methylate nucleic acids, proteins and membrane phospholipids. After the removal of methyl group from SAM by a methyltransferase, the resulting S-asenosylhomocysteine is converted to homocysteine and adenosine by adenosylhomocysteinase. A condensation reaction which combines homocysteine with serine is then catalyzed by the pyridoxal phosphate-dependent cystathionine synthase. The product cystathionine is hydrolyzed by another pyridoxal phosphate dependent enzyme cystathionase to give α-ketobutyrate, ammonia and cysteine. When energy is needed instead of cysteine, homocysteine is converted to α-Ketobutyrate, ammonia and hydrogen sulfide by homocysteine desulfhydrase (Scheme 1-17).

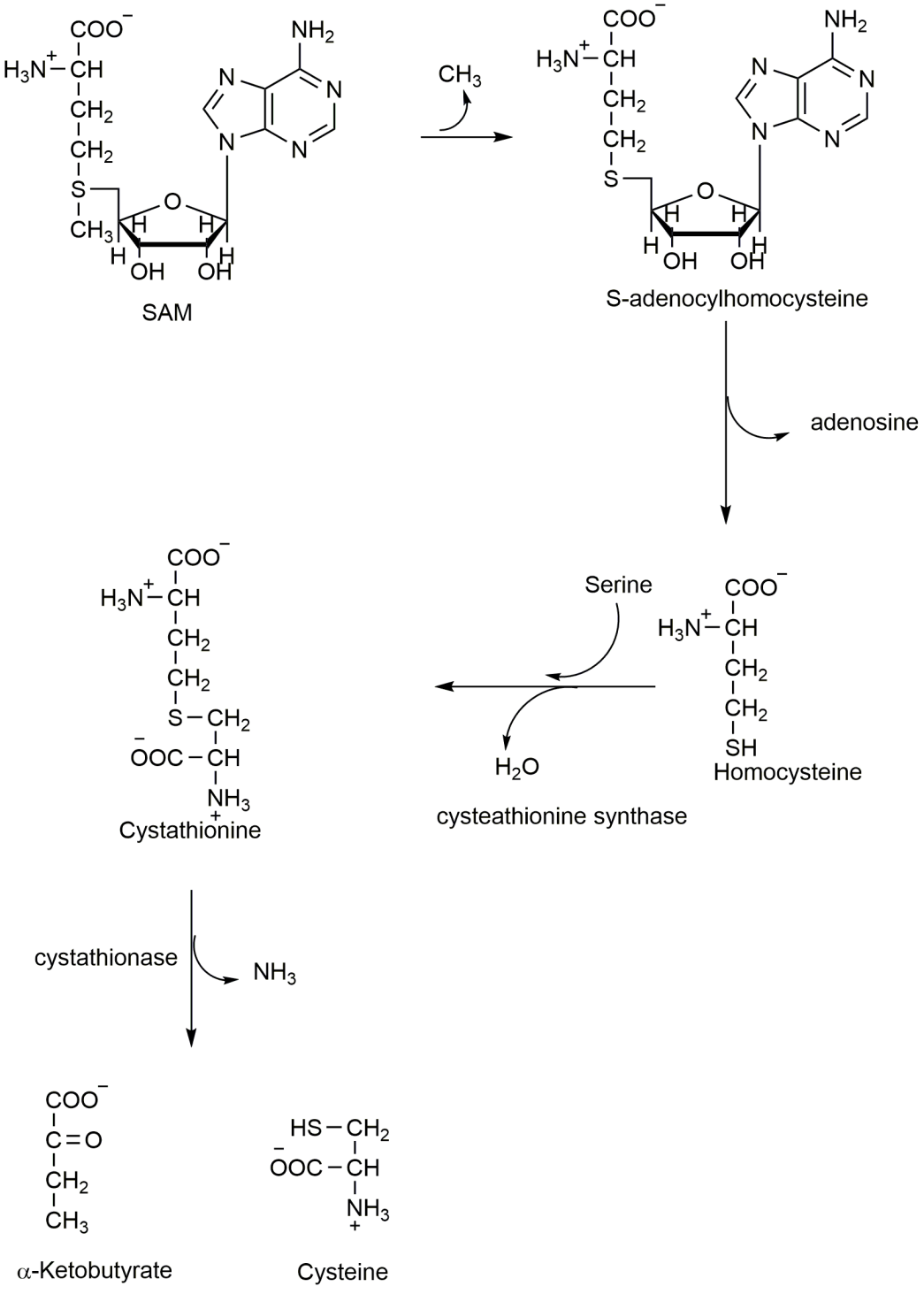
SAM
CH3
S-adenocylhomocysteine
adenosine
Serine
H2O
Homocysteine
cysteathionine synthase
Cystathionine
cystathionase
NH3
α-Ketobutyrate
Cysteine

Scheme 1-17 Biosynthesis of cysteine form SAM.

Dependent on what the cells need, cysteine can be metabolized in many different ways (Scheme 1-18) [86]. The major metabolite is cysteine sulfinic acid (CSA), which is the $O_2$ dependent thiol oxidation product of cysteine catalyzed by cysteine dioxygenase. As a branch point in cysteine metabolism, from here, CSA is either converted to pyruvate and inorganic sulfate or taurine. As one of the substrates for aspartate aminotransferase, CSA is transfomed to 3-sulfinylpyruvate while α-ketobutyrate is converted to glutamate.

3-sulfinylpyruvate is decomposed to pyruvate and bisulfite by 3-sulfinylpyruvate

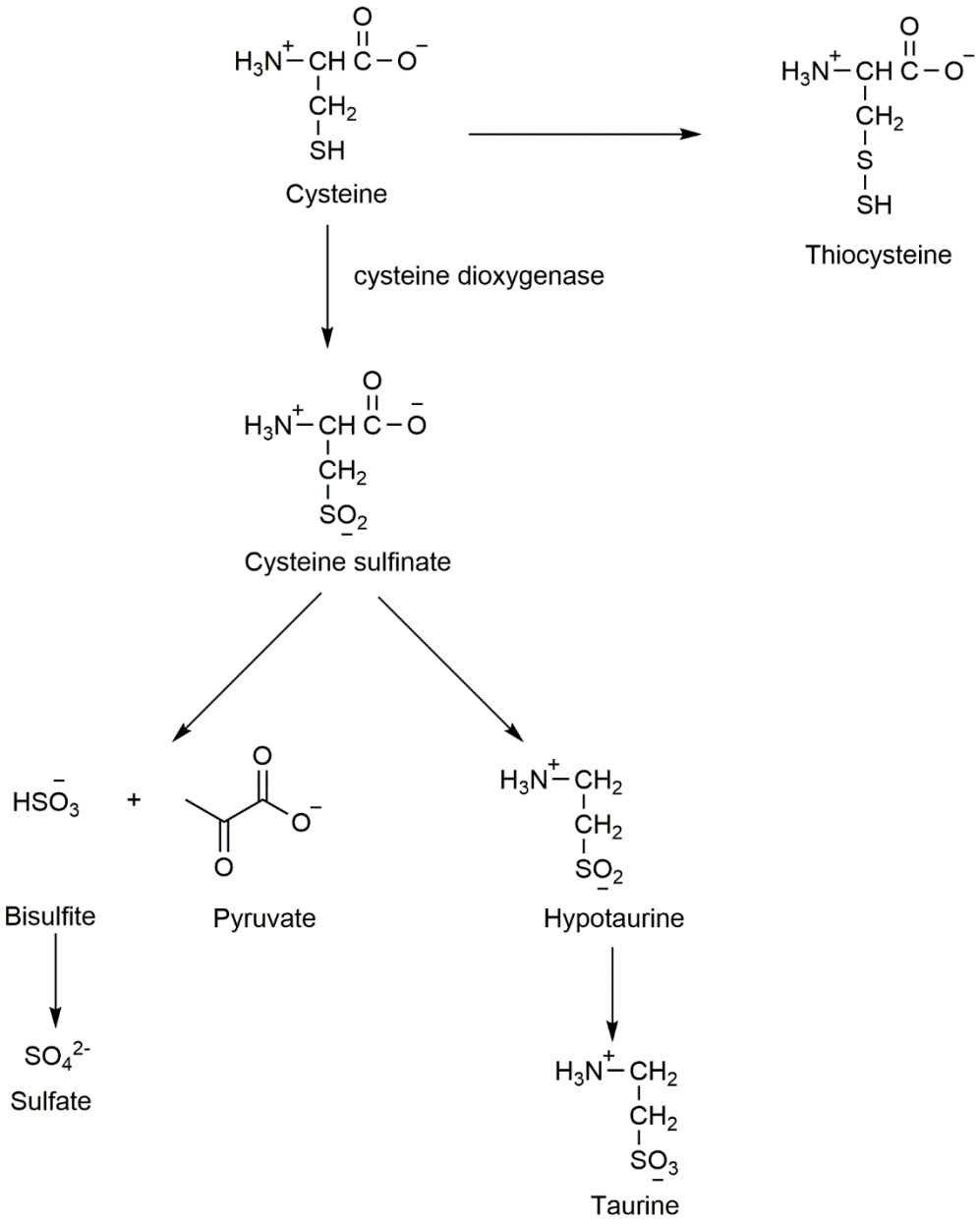


sulfurtransferase. Bisulfite is further oxidized to inorganic sulfate by sulfite oxidase.

Scheme 1-18 Cysteine metabolism.

In the other branch of cysteine metabolism, the carboxylic group of CSA is removed by the pyridoxal phosphate-dependent enzyme cysteine sulfinate

decarboxylase to give hypotaurine. Taurine is synthesized from hypotaurine by the $NAD^+$ dependent enzyme hypotaurine dehydrogenase.

Taurine is the most abundant intracellular free amino acid in mammalian systems with a concentration of 50 mM in leukocytes [91]. Although it doesn't have the carboxylic acid group in most amino acids, it has a sulfonic acid functional group. Hence it's considered as an amino acid but it does not incorporate into proteins. Due to its hydrophilicity, taurine is unable to diffuse through cellular membranes. The concentration of cellular taurine is regulated by taurine transporter, which is affected by ionic environment, electrochemical charge, and post-translational and transcriptional factors [86]. Taurine has many importance biological roles such as antioxidation, osmoregulation, membrane stabilization and modulation of calcium signaling. It plays an important role in brain development. It is also essential for cardiovascular function, and development and function of skeletal muscle. Taurine forms conjugates with bile acids and enhances bile flow and increases cholesterol clearance by liver [86].

In another cysteine metabolism, sulfur is transferred from one cysteine to another by cystathionase to form thiocysteine, which is involved in the detoxification reaction of cyanide catalyzed by rhodanese (Scheme 1-19) [86].

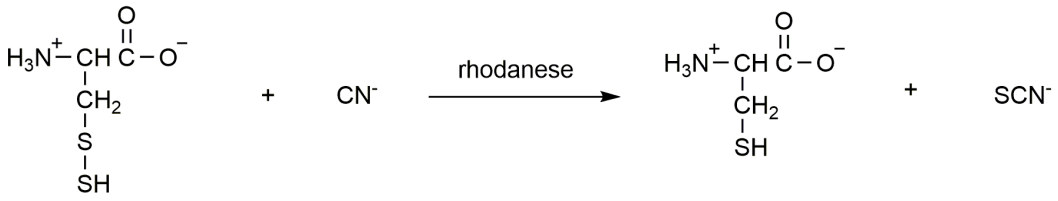


Thiocysteine + $CN^-$ → Cysteine + $SCN^-$

Scheme 1-19 Detoxification of cyanide by thiocysteine.

The synthesis of glutathione is largely regulated by cysteine concentration. Glutathione (GSH) is a tripeptide synthesized from glutamate, cysteine and glycine (γ-

glutamylcysteinylglycine). Glutathione has many important functions. It is part of some leukotriene structrures, is involved in the transportation of amino acids across cell membranes, works as a cofactor in some enzymatic reactions, participates in the rearrangement of disulfide bonds and is conjugated with drugs to make them more water soluble [86]. As a reductant, its sulfhydryl group reacts with many small reactive species associated with oxidative stress in cells including peroxides and peroxynitrite. It maintains the stability of erythrocyte membranes by reducing the peroxides formed during oxygen transport. When oxidized, two molecules of GSH joins together by a disulfide bond and exists as a dimer (GSSG). GSSG is reduced by glutathione reductase to two GSH molecules with the help of NADPH (Figure 1-3, 1-4) [86].

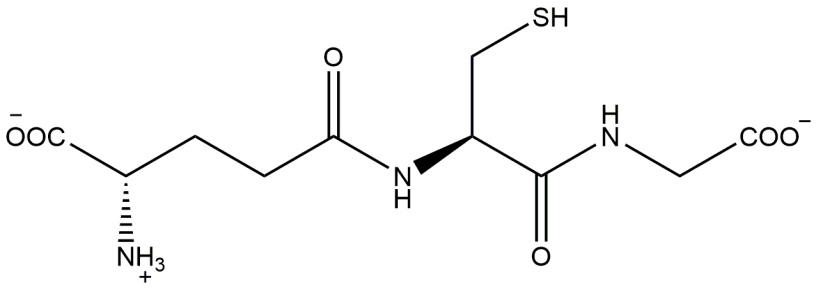


Figure 1-3 Reduced form of glutathione.

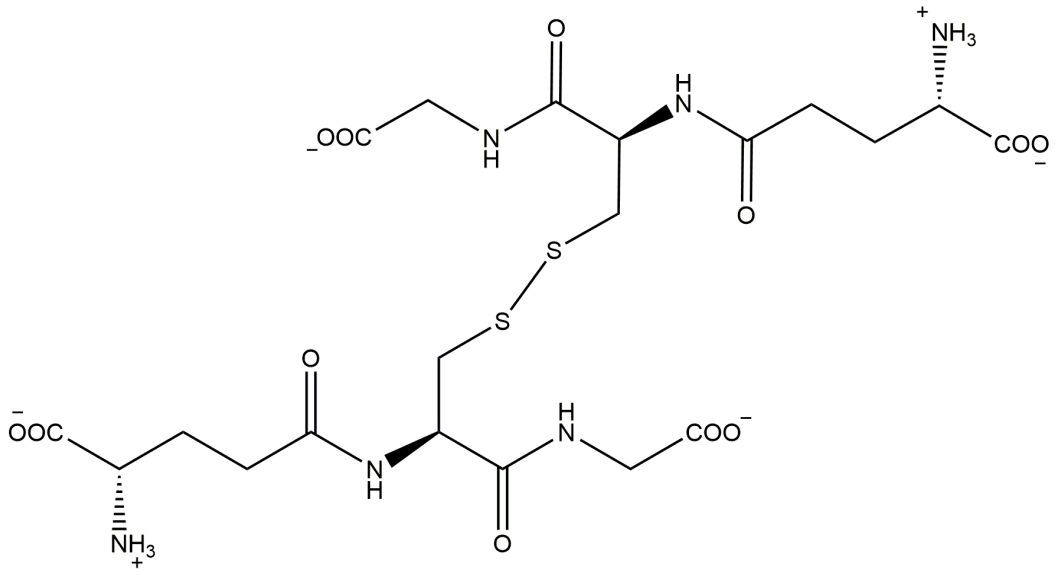


Figure 1-4 Oxidized form of glutathione.

Free cysteine can also form cystine molecules through the formation of a disulfide bond. Unlike GSSG, cystine is insoluble in cellular environment and has cytotoxicity. Hence the cysteine concentration is regulated. The concentrations of cysteine and glutathione in cellular environment are in equilibrium which is regulated via two metabolic processes [86, 92]. Synthesis of glutathione from cysteine is carried out by glutamate-cysteine ligase resulting in the formation of L-γ-glutamyl cysteine, which is then combined with glycine by glutathione synthase to produce glutathione (Scheme 1-20). On the other hand, glutathione-cysteine transhydrogenase catalyzes disulfide exchange reactions between cystine and GSSG which helps to regulate the cellular cysteine concentration (Scheme 1-21).

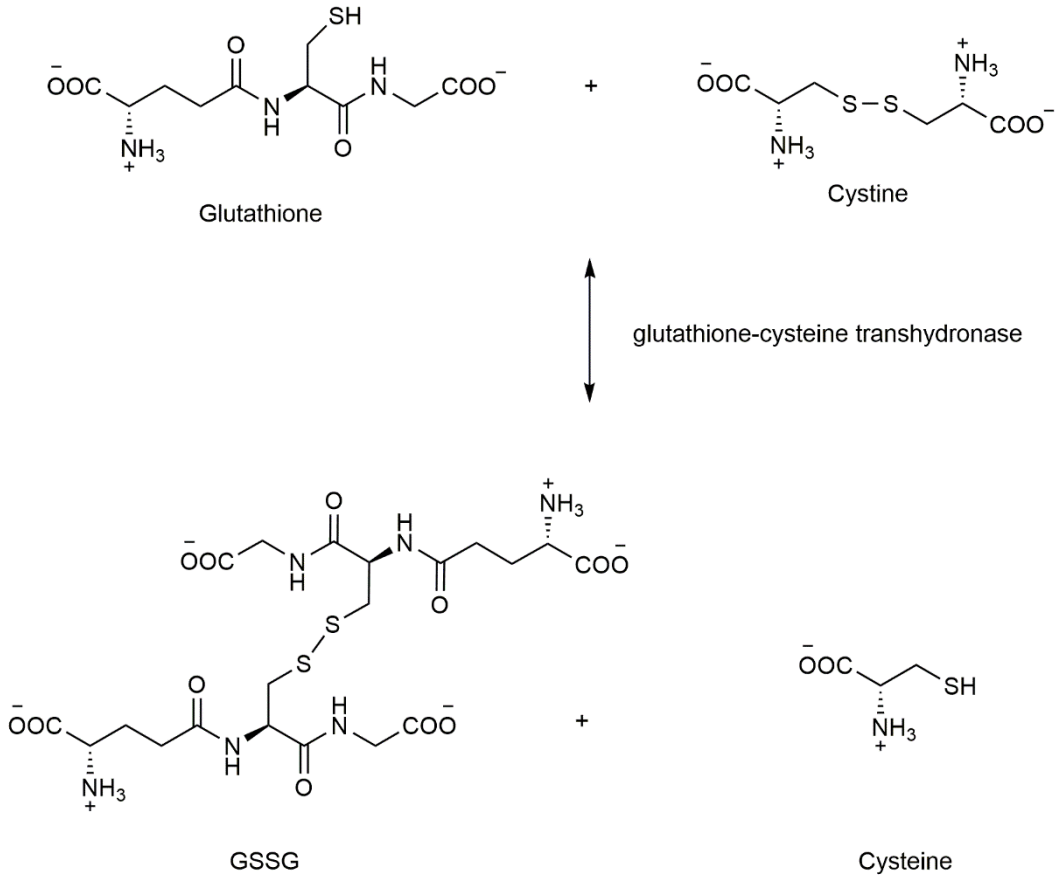


Scheme 1-20 Biosynthesis of glutathione with cysteine.

Scheme 1-21 Equilibrium between cysteine and glutathione.

Free cellular cysteine is also involved in the biosynthesis of coenzyme A (CoA), which is essential for various metabolic pathways such as TCA cycle [86]. Cysteine comes into play in the second step of CoA synthesis, in which 4-phosphopantothenate is condensed with cysteine catalyzed by phosphopantothenoylcysteine synthetase. The carboxylic acid group of the cysteine residue is then removed by

phosphopantothenoylcysteine decarboxylase to form 4-phosphopantotheine. If CoA is not needed, 4-phosphopantotheine is broken down to pantothenate and cysteamine. Cysteamine is the substrate of cysteamine dioxygenase (ADO), which is the only other known thiol dioxygenase in mammalian and converts it to hypotaurine (Scheme 1-22) [93].

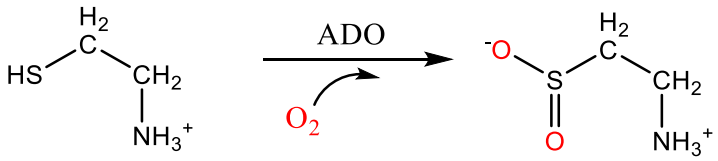


Scheme 1-22 Reaction catalyzed by ADO.

*Cysteine Dixoygenase*

Early study on CDO

Cysteine dioxygenase was discovered in crude rat liver extracts that produced cysteine sulfinic acid from cysteine [94, 95]. It was call cysteine oxidase initially. Labelling studies using $^{18}O_2$ and $H_2{}^{18}O$ showed that this enzyme incorporated both oxygen atoms from molecular oxygen into product, indicating it belonged to the dioxygenase family (Scheme 1-22) [94]. In early studies, purified CDO was in an inactive form after the conventional isolation procedures, which could be reactivated by pre-incubation with L-cysteine under anaerobic conditions [96]. The purified rat liver CDO had a molecular weight of 22.5 kDa as a single subunit protein with 0.8 moles of iron per mole of enzyme incorporated and the pI value was 5.5 [97]. It was also reported that the presence of protein-A, a cytosolic protein, is necessary for CDO to remain active which does not participate in the catalytic process.

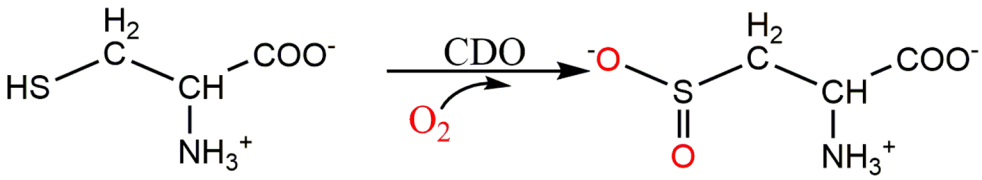


Scheme 1-23 Reaction catalyzed by CDO.

Later studies on CDO confirmed that the functional enzymes is a monomer that has a molecular weight of around 23 kDa, requires ferrous iron as a cofactor and is specific for L-cysteine [18]. However, the necessity of protein-A for CDO to remain active is disapproved. The SDS-PAGE of CDO repeatedly yield two separate species with the molecular weight of approximately 23 and 25 kDa, respectively [98, 99].

Recombinant CDO was expressed and purified either using immobilized metal affinity chromatography (IMAC, using His-tag and Ni-NTA affinity column) or without any affinity tag [2, 17, 18, 98]. No matter which method is applied, all samples of recombinant CDO had a lower iron binding rate (10 - 50%) compared to enzymes isolated for rat liver (80%) and showed as a doublet on SDS-PAGE. The two isoforms of CDO were separated by IMAC HPLC and analyzed for activity. It was reported that the species that had a lower molecular weight showed no catalytic activity while the other one was active. This implied that a post-translational modification activates CDO and regulates its activity [17].

Structure of CDO

Since the first crystal structure of CDO was published in 2006, which was of mouse CDO using Ni(ii) as a substitute for iron, many crystal structures of different types of recombinant CDO have been reported [2, 17, 98]. The study of CDO has been making huge progress with the availability of crystal structure. Crystal structures of CDO reveals that it belongs to the cupin superfamily, which have a characteristic β-barrel structure and

coordinate a mononuclear metal ion. There are two conserved sequence motifs, $G(X)_5HXH(X)_{3,4}E(X)_6G$ and $G(X)_5PXG(X)_2H(X)_3N$, that provide the ligands to coordinate the metal ion at the active site [100]. Typically two histidine residues and glutamate residues (or aspartate residue) from the first motif and the histidine residue from the second motif coordinate to the metal ion as ligands. In CDO, the glutamate residue is replaced by a cysteine residue (Cys93) and the metal center is coordinated only by three histidine residues (His86, His88 and His140) and three free water molecules forming a six-coordinate metal complex (Figure 1-5). This cysteine residue substitution is conserved in all mammalian CDOs, but is not retained in bacterial CDO, where typically a glycine residue is present. Similar to the typical 2-His/1-carboxylate motif mentioned above, the three histidine residues form a facial triad with water molecules occupy the other face of the octahedron.

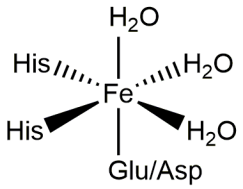


Figure 1-5 3-His facial triad of CDO.

The crystal structures also reveal another characteristic feather of CDO, which is the covalent bond forms between Cys93 and Tyr157 near the active site. Only three other enzymes have this unusual post-translational modification besides CDO [101-103]. Although it's been proposed that the formation of the covalent bond may follow the mechanism of the formation of an analog post-translational modification in galactose oxidase, it's still unknown how it is formed. It's been reported that this C93-Y157 forms over multiple enzymatic turnovers. While C93 is only conserved in mammalian CDOs, Try157 is conserved in all identified CDOs, as well as Tyr58, Arg60, Trp77, Ser153,

His155 and the three histidine residues coordinated to the metal ion [98]. Crystal structures also confirm that this C93-Y157 pair is present in all mammalian CDOs and the isoforms displayed on SDS-PAGE are corresponding to enzymes with and without this post-translational modification [17].

Characterization

Since the discovering of first CDO protein, many groups have characterized and reported kinetic parameters for CDO. The kinetic study of CDO is mainly done by determination of the product formation by HPLC using a C18 column. In the first reported assay of recombinant CDO in 2005, the ion-pairing reagent heptafluorobutyric (HFBA) acid was used in the mobile phase to retain CSA on the hydrophobic C18 column due to the high polarity and CSA was detected at 215 nm using UV detector [104]. Another method to analyze CSA using HPLC was published in 2006. In this method, o-hthalaldehyde label was added to CSA via reaction to increase the hydrophobicity [17]. Also the fluorescence property of o-phthalaldehyde, the sensitivity of detection was also increased a lot. However, the drawback for this method is that the labeling reaction is optimized in acidic conditions, which may lead to inaccurate conclusion of the optimal pH for CDO activity.

A wide range of kinetic parameters of CDO have been reported by different groups with $K_m$ ranging from 0.45 mM to 5.7 mM, which is relatively large compared to the $K_m$ values of most other enzymes [17, 18, 98]. However, it is common that enzymes that converts sulfur-containing compounds have a $K_m$ in the millimolar range [18, 105-107]. Optimal pH for CDO was determined as 6.1 when using the o-phthalaldehyde derivative method, which is significantly lower than others. This is very likely due to the acidic conditions during the process. The parameters for CDO with and without the post-translational modification were not distinguished until they were reported by our group

separately in 2011 [108]. Oxygen coupling, which is the efficiency oxygenases utilizing oxygen, was also reported by our group first in 2011.

Mechanism

Lots of effort has been done to investigate the mechanism of CDO by different groups. Since the 3-His motif at the active site is considered as a variant of the common 2-His/1-carboxylate motif found in non-heme mononuclear iron enzymes, the mechanism study is based on the known/proposed ones for non-heme mononuclear iron enzymes [3, 4].

Crystal structures of different CDOs show that in the resting state, the iron(ii) center is coordinated by the 3-His motif together with three water molecules. L-cysteine bidendate binds to the metal through its thiolate and amine group, displacing two of the water molecules with the thiolate group and the neutral amine group *trans* to $His_{88}$ and $His_{140}$, respectively. However, no oxygen-bound intermediates had been identified and characterized because they are short-lived until recently a putative ferrous iron-bound persulfenate intermediate was identified crystallographically. Using NO as a surrogate for molecular oxygen, electron paramagnetic resonance (EPR) studies show that substrate must bind first before oxygen could bind [104]. This obligated binding of oxygen is consistent with other non-heme mononuclear iron dioxygenases.

In galactose oxidase, the Cys-Tyr pair serves as an internal redox cofactor and is involved in catalysis in the form of a Cys-$Tyr^{\cdot}$ radical, which supplies one electron to produce an Fe(III)-peroxy species[109]. In Rieske dioxygenase mechanism discussed above, the reduced internal [2Fe-2S] cluster plays a similar role which provide one electron for the formation of iron(III)-peroxy intermediate. The function of Cys-Tyr in CDO has yet to be investigated. Since Cys93 is not conserved in bacteria CDO, which means

the lack of Cys-Tyr pair, it is unlikely that the Cys-Tyr pair is as essential as the one in galactose oxidase and no proof of radical character has been found so far.

Site-directed mutagenesis studies were conducted on different residues near the active site to explore the residues involved in catalysis. When Tyr157 was mutated to phenylalanine, enzymatic activity was almost diminished (~5% of wild type), indicating the importance of this residue in catalysis, which also explains why it's conserved in both mammalian and bacteria CDO. Mutation of Cys93 (to serine or alanine) reduced the enzymatic activity by ~ 50%, indicating the importance of the Cys-Tyr pair for activity. Residue Arg60 was speculated to stabilize the substrate binding through hydrogen bond, and in R60E and R60A mutants, the enzymatic activity drops only by ~ 30% [98].

Several different mechanisms have been proposed describing how the oxygen is activated [2, 17, 98, 104]. In the first mechanism, after the binding of substrate, oxygen binds to iron and forms an Fe (III)-superoxo intermediate. Distal oxygen atom attacks sulfur and forms a cyclic 4-membered Fe-O-O-S ring. Homocleavage of the O-O bond results in a sulfoxy cation and an activated oxygen atom. The activated oxygen atom then attacks the sulfur to form the sulfinate group. Product is released by the replacement of water molecules (Scheme 1-24).

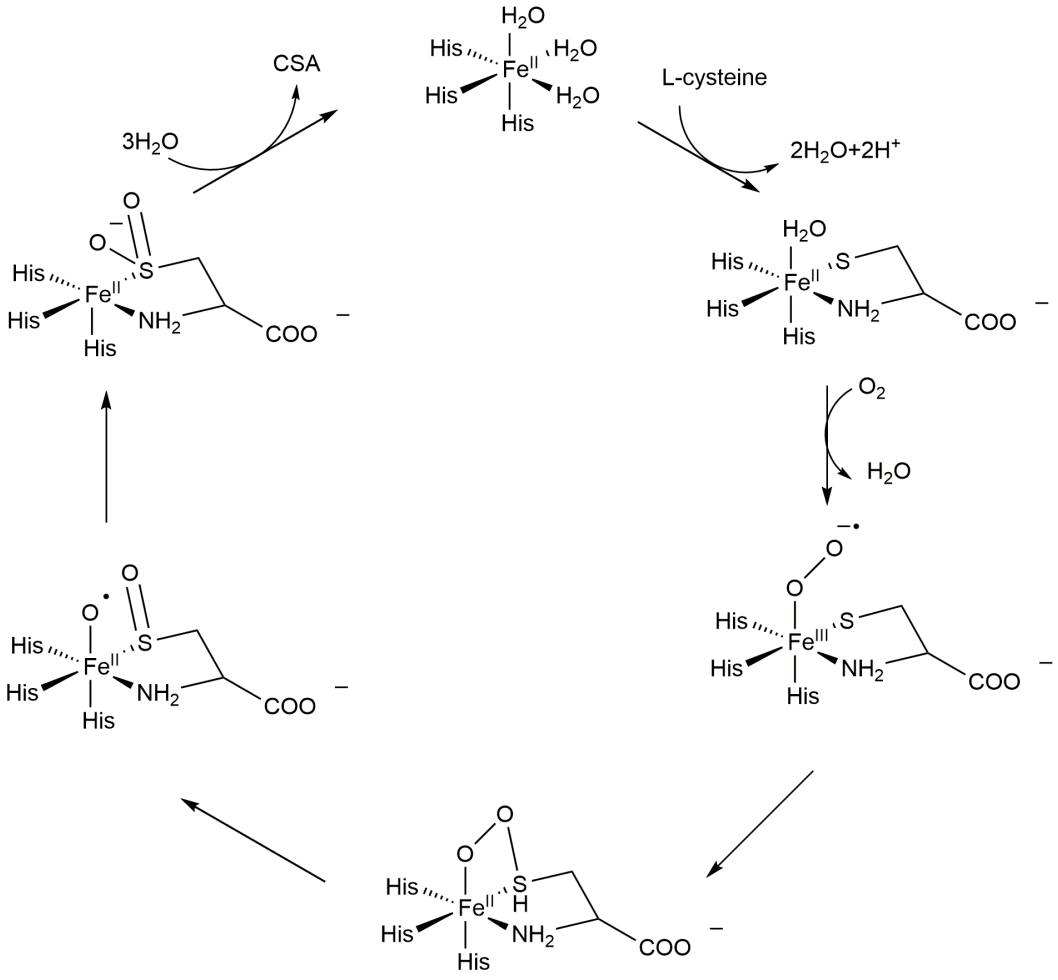


Scheme 1-24 Proposed mechanism for CDO.

In a second proposed mechanism, Try157 is involved in the catalysis (Scheme 1-24). Upon substrate binding, the carboxyl group of cysteine is coordinated to Try157 through hydrogen bond and participate in the hydrogen bonding network formed by the second coordination sphere (highly conserved residue Tyr157, Tyr58 and His155). Oxygen binds the iron in an end-on fashion. Because of the e proximity, the distal oxygen and the thiol sulfur forms a peroxo intermediate with a sulfur radical cation. Homocleavage of the O-O bond couples with the hydrogen abstraction from Tyr157,

forming a tyrosyl radical and a high-valent iron(IV)-oxo species. The radical abstracts a.hydrogen from the substrate's thiol group. The high-valent iron-oxo species attacks the sulfur and forms a single S-O bond. Reductive elimination leads to the formation of S=O and center iron returns to ferrous state. In the final step, the sulfinic acid is deprotonated and product is released. In this mechanism, cysteine binds the iron using thiol group instead of thiolate, which is not normal. However, it postulates the role of Try157 in catalysis.

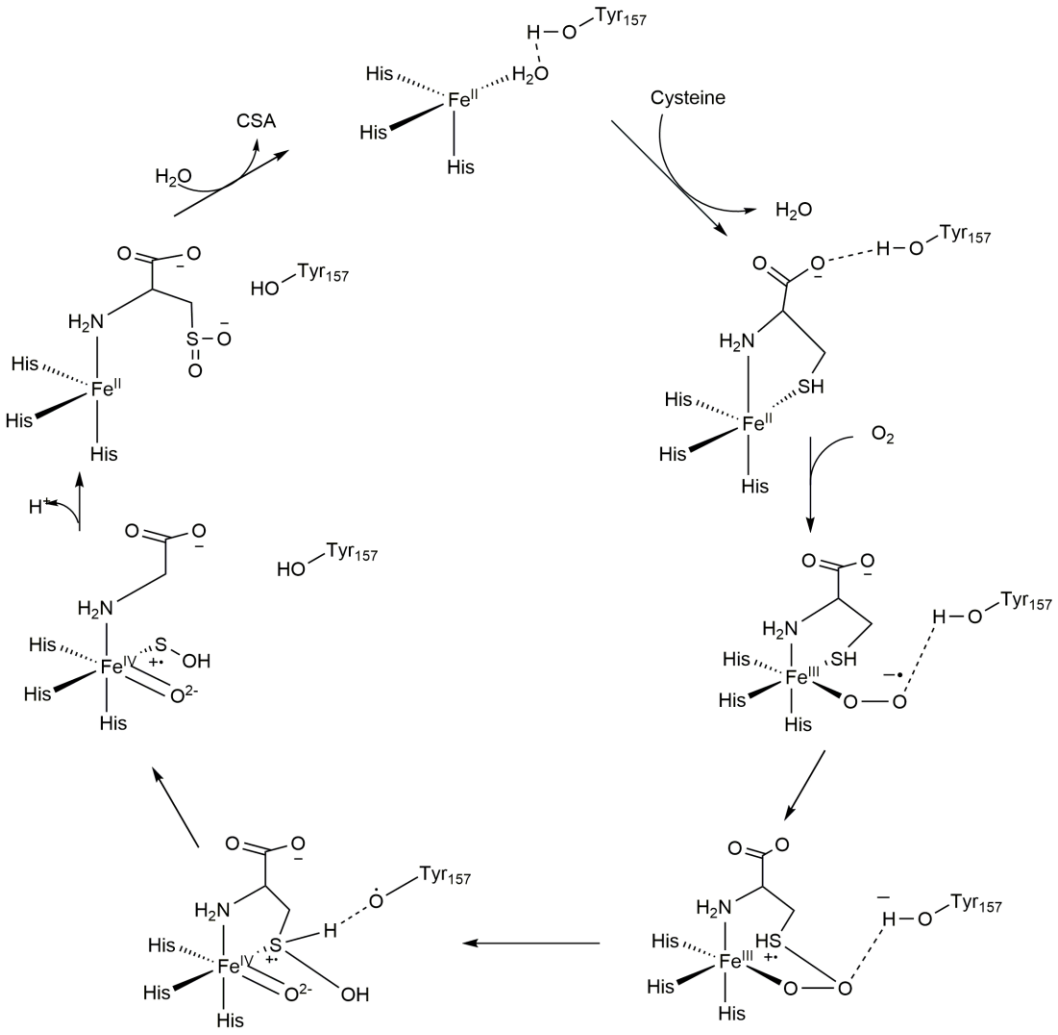


Scheme 1-25 Proposed mechanism for CDO II.

The crystallographical identification of a putative ferrous iron-bound persulfenateintermediate within CDO leads to the proposal of another mechanism (Scheme 1-26). The initial steps of this mechanism are similar to the ones in the first mechanism discussed above (Scheme 1-24). Mechanism diverging starting from the formation of the neutral Fe−O−O−S cyclic persulfenate ring. Nucleophilic attack of the proximal O atom on the S atom results in formation of a Cys-thiadioxirane ring (H). And

the heterolytic cleavage of the O−O bond leads to the formation of the CSA product and enzyme goes back to the resting state.

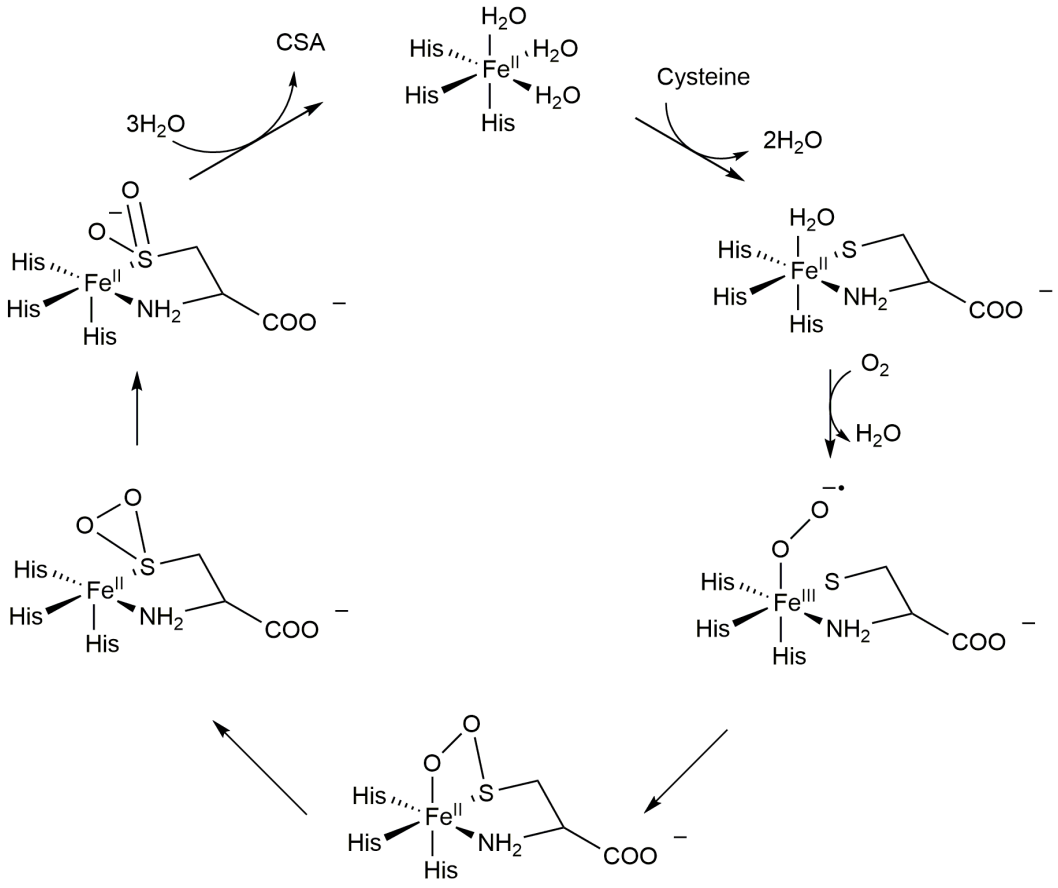


Scheme 1-26 Proposed mechanism for CDO III.

Diseases Related to Cysteine and CDO

Abnormal CDO activity has been linked to a number of diseases. Free cysteine in cells forms insoluble cystine, which will precipitate forming cystine stones [110]. It's also been postulated that cysteine contributes to the formation of reactive oxygen species which is a threat to health due to its oxidizing ability. High levels of cysteine have been associated with motor neuron disease, Alzheimer's disease and Parkinson's disease [111, 112]. In patients suffering Hallervorde-Spats disease, which is a rare neurological

disorder, CDO activity is low and accumulation of cyst(e)ine has been observed [113]. Poor sulfoxidation and reduced formation of inorganic sulfate are related to rheumatoid arthritis [114]. The reduced expression of CDO has also been observed in tumor cells [115]. In addition, as the critical enzyme in taurine synthesis, absence of CDO leads to taurine deficiency, which will cause many severe health problems [116].

## Summary

Cysteine dioxygenase is an important enzyme that regulates cysteine levels in cells. As a member of the non-heme mononuclear iron dioxyngease family, it has an unusual 3-His facial triad compared to the normal 3-His/1-carboxylate motif. Although mechanism of some of the enzyme in this family have been well studied and established, the detail of CDO catalysis remains unclear. Although several spectroscopy methods including EPR, resonance raman, Mössbauer and mass spectroscopy have been utilized, no oxygen-bound intermediate that could be the direct evidence for catalysis has been identified.

Thiol containing compounds play important roles in physiological process. CDO as one of the only two identified mammalian thiol dioxygenase is critical in the synthesis of these thiol containing compounds. The linkage of CDO activity to neurological disorders, cancer and other diseases makes it a potential drug target. Understanding the mechanism would contribute to the development of cure methods for those diseases. Following chapters will discuss efforts and findings in the investigating of CDO catalysis.

# Chapter 2

## Single Turnover of Substrate-Bound Ferric Cysteine Dioxygenase with Superoxide Anion: Enzymatic Reactivation, Product Formation, and a Transient Intermediate

### Introduction

Cysteine dioxygenase (CDO) [EC 1.13.11.20] is a mononuclear non-heme iron enzyme that catalyzes the $O_2$-dependent oxidation of L-cysteine (Cys) to produce cysteine sulfinic acid (CSA) [95, 117-119]. This enzyme catalyzes the first committed step in the catabolic dissimilation of Cys to produce inorganic sulfate, pyruvate, hypotaurine, and taurine [120]. Intracellular Cys concentration is the limiting factor in glutathione (GSH) synthesis; therefore, the activity of CDO directly competes with cellular redox buffering under conditions of low Cys availability and oxidative stress. In response to such conditions, CDO is degraded by the ubiquitin–proteasome system in a cysteine-responsive manner [121]. Recently, the study of enzymes involved in mammalian sulfur-metabolism have been of considerable medical interest due to the observation that patients suffering from neurological disorders such as autism and Down syndrome have significantly lower plasma concentration of transsulfuration pathway and methionine cycle products [Cys, homocysteine (HCY), and GSH, and *S*-adenosylmethionine (SAM)] [122, 123]. In fact, imbalances in Cys metabolism have been identified in a variety of other neurological disorders as well (motor neuron, Parkinson's, and Alzheimer's disease) [124-126]. These observations suggest a potential correlation between impaired sulfur-metabolism, oxidative stress, and neurodegenerative disease [122].

CDO exhibits high specificity for L-cysteine, displaying little or no reactivity with D-cysteine, glutathione, L-cystine, or cysteamine. While results from steady-state kinetics of recombinant CDO are available, few direct mechanistic details are known [17-19].

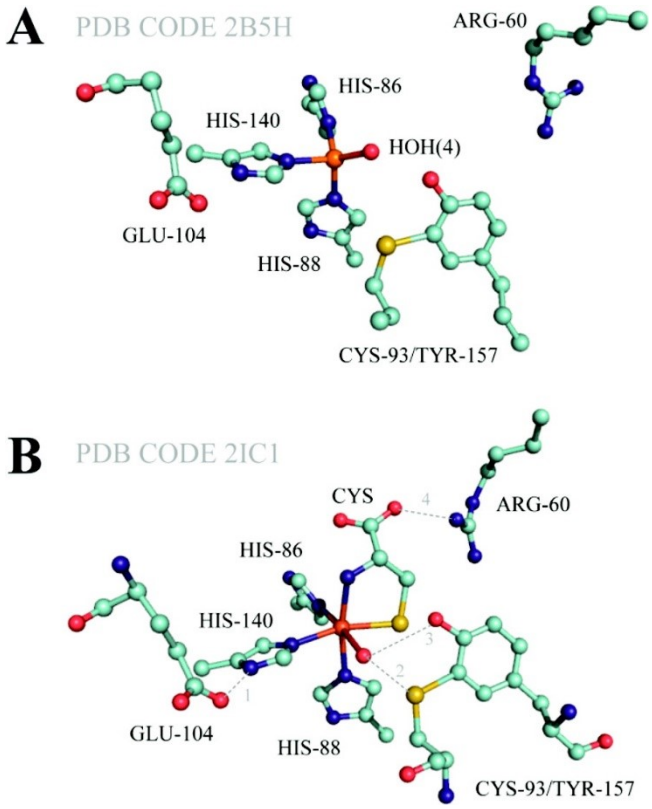


Figure 2-1 Crystal Structure of CDO.
(A) Crystal structure (1.75 Å resolution) of resting CDO (PDB entry 2ATF).(14) Active site solvent ligands are designated W1–W3. (B) Crystal structure (2.7 Å resolution) of the substrate-bound CDO active site (PDB entry 2IC1). Selected distances indicated by 1–4 are 2.70, 2.75, 2.88, and 2.27 Å, respectively.

Multiple high-resolution crystal structures of mammalian CDO have been determined (pdb codes 2ATF, 2B5H, and 2IC1) [7, 72, 98]. As illustrated in Figure 2-1 A, the active site coordination of CDO is comprised of iron ligated by the $N_{\varepsilon}$-atoms of His86, His88, and His140, representing a new 3-His (3H) variant on the classic 2-His-1-carboxylate facial triad observed in mononuclear nonheme iron enzymes [127]. To date, only two enzymes with a 3H facial triad motif (CDO and diketone dioxygenase, Dke1) have been crystallographically [128] and spectroscopically characterized [129, 130].

However, it has been proposed on the basis of sequence homology that the active site of cysteamine (2-aminoethanethiol) dioxygenase (ADO) also contains a 3H facial triad [93].

Within 3.3 Å of the non-heme iron CDO active site is a covalently cross-linked cysteine–tyrosine pair (C93–Y157). An analogous post-transcriptional modification has been observed previously in only three other enzymes [131-133]. Since one of these enzymes is the copper radical enzyme, galactose oxidase (GO), it was initially proposed that a cysteine–tyrosine radical may also be involved in the oxidation of Cys [2]. However, mutations at C93 and Y157 lower, but do not abolish, enzymatic activity [2, 25]. Moreover, the analogous C93 and Y157 residues are not conserved among putative bacterial CDO enzymes [15]. It has also been observed that addition of known radical scavengers such as hydroxyurea have no effect on steady-state kinetics of recombinant CDO [16]. On the basis of these observations, it is unlikely that the C93–Y157 pair of mammalian CDO is catalytically essential. Regardless, neither the mechanism of C93–Y157 formation nor its role in enzymatic catalysis is currently understood.

Prior to the addition of $O_2$, Cys coordinates to the mononuclear ferrous site of CDO in a bidentate fashion through a thiolate and neutral amine [2, 16, 127]. Presumably, the hydrogen bond between E104 and H140 results in a unique Cys amine binding site *trans* to H140 [104]. Additional ligation of the Cys thiol group within the trigonal plane opposite H86 and H88 positions the carboxylate group of Cys favorably for charge stabilization by the R60 guanidinium group. This ternary interaction between Cys and the enzymatic active site shown in Figure 2-1 B explains the high substrate specificity exhibited by CDO. A sixth coordination site would then be available for binding of molecular oxygen.

Within the 2-His-1-carboxylate family of non-heme iron containing oxidases and oxygenases, a general mechanism for catalysis has emerged based on extensive

synthetic, mechanistic, spectroscopic, and crystallographic characterization [4-6]. Typically, the monoanionic active site contains a 5- or 6-coordinate ferrous iron with solvent molecules serving as the non-protein ligands. In the absence of substrate and/or cofactor, the reduced active site is unreactive toward $O_2$ [4]. Similar behavior has also been observed for CDO. In experiments where nitric oxide (NO) was used as a surrogate for $O_2$ binding, CDO demonstrated an obligate-ordered binding of Cys prior to NO [104].

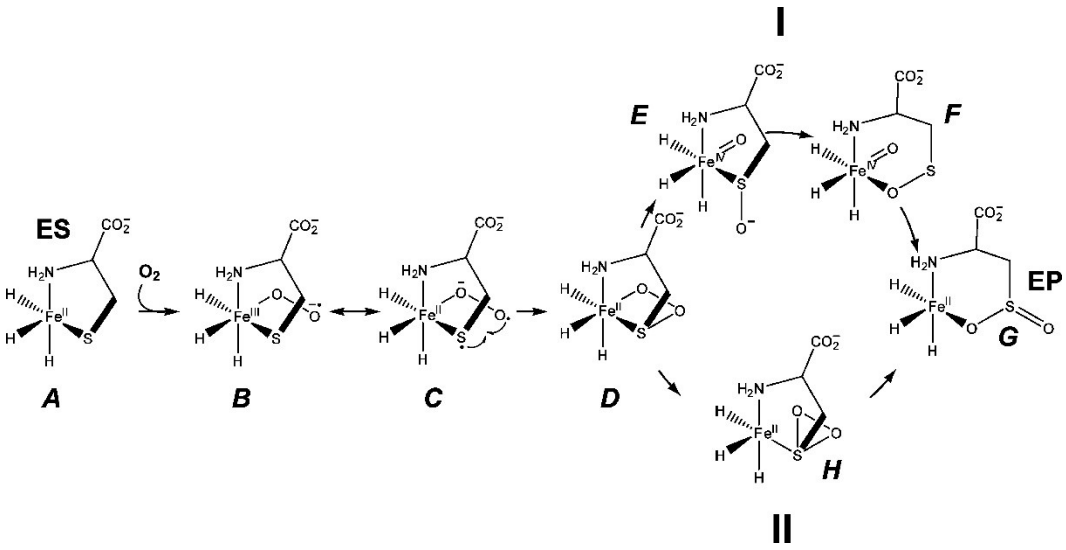


Figure 2-2 Proposed mechanistic pathways for CDO-catalyzed oxidation of Cys to produce CSA.

Based on this 2-His-1-carboxylate model, and the limited mechanistic information available, at least two reasonable reaction pathways have been proposed for CDO (Figure 2-2), which ultimately lead to the production of L-cysteine sulfinic acid and a ferrous iron resting state for the enzyme. In the first step, binding of oxygen to the substrate-bound ferrous active site (**A**) would result in an internal electron transfer producing a short-lived ferric-superoxo [$Fe^{III}$-$O_2^{\bullet-}$] species (**B**). Resonance charge transfer between the ferric iron and the bound Cys thiolate could impart transient radical

character on the S-atom (**C**), resulting in rapid recombination of bound superoxide and thiol radicals. The formation of the cyclic 4-membered Fe–O–O–S ring structure (**D**) has no precedent in 2-His-1-carboxylate enzymes; however, numerous reported DFT and QM/MM computations of CDO intermediates indicate that this structure is energetically favorable [134-136]. At this point, the reaction mechanism diverges to support the formation of two proposed intermediates. Shown in the upper pathway (**I**), heterolytic cleavage of the O–O bond would result in the formation of a transient $Fe^{IV}$-oxo species (**E**) such as those identified for a variety of $O_2$-activating 2-His-1-carboxylate oxygenase enzymes [taurine α-ketoglutarate (αKG)-dependent dioxygenase (TauD) and prolyl-4-hydroxylase (P4H)] [23, 29, 137-139]. This model is supported by DFT and QM/MM computational studies; however, no experimental evidence for such an intermediate currently exists. On the basis of computational modeling, it has been proposed that rapid rearrangement of (**E**) to favor direct coordination of the cysteine sulfenate O-atom (**F**) directly precedes final $Fe^{IV}$-oxo rebound to generate a ferrous iron bound CSA (**G**) [134-136]. Interestingly, the model proposed on the basis of DFT and QM/MM computations for the CSA-bound resting enzyme (**G**) suggests direct O-atom coordination of CSA. Typically, model complexes containing metal-bound sulfinates derived from oxidation of thiolate ligands are coordinated through the sulfinate S-atom [140-142]. Indeed, direct S-atom sulfinate coordination is also observed in the mononuclear Fe(III) active site of nitrile hydratase [143]. Another feature of this model currently debated is whether or not the neutral 3H ligand set of CDO is sufficiently π-donating to stabilize a $Fe^{IV}$–O intermediate. Moreover, the bidentate S/N-atom coordination observed for the Cys-bound active site would be less stabilizing for high valent iron–oxo intermediates as compared to α-ketoglutarate (αKG) coordination in αKG-dependent dioxygenase.

Recently, a putative ferrous iron-bound persulfenate intermediate was identified crystallographically within CDO. On this basis, an alternative mechanism for CSA formation has been proposed by Simmons et al [144]. An adaptation of this mechanism is shown in the lower pathway of Figure 2-2 (**II**). Starting from the neutral Fe–O–O–S cyclic persulfenate ring (**D**), nucleophilic attack of the proximal O-atom on the S-atom of the persulfenate would result in formation of a Cys-thiadioxirane ring (**H**). Subsequent heterolytic cleavage of the O–O bond would result in the formation of the CSA product and resting ferrous enzyme (**G**). In principle, direct nucleophilic attack of the Fe-bound thiolate on $O_2$ could bypass steps **B** through **D**, thus going directly from the substrate-bound enzyme (**A**) to the thiadioxirane (**G**). A similar reaction mechanism has been proposed in the $O_2$-dependent thiol-oxidation observed in nickel(II)–thiolate model complexes [145, 146]. Given the absence of a high-valent Fe–oxo intermediate, this lower pathway is most comparable to the "substrate-activating" reaction mechanism proposed for $Fe^{II}$-containing homoprotocatechuate 2,3-dioxygenase (2,3-HPCD) [147].

A common feature for reaction mechanisms is the formation of a transient substrate-bound $Fe^{III}$-superoxo species (**B**). Indeed, ferric-superoxide intermediates have been proposed for several 2-His-1-carboxylate non-heme mononuclear iron enzymes including isopenicillin N synthase (IPNS), 1-aminocyclopropane-1-carboxylic acid oxidase (ACCO), and hydroxyethylphosphonate dioxygenase (HEPD) [25, 148, 149]. However, to date, only one such example has been spectroscopically identified, (2,3-HPCD) [150]. Interestingly, the catalytically active, $Mn^{II}$-substituted form of 2,3-HPCD also produces a transient $Mn^{III}$-superoxo species upon addition of oxygen to the substrate-bound enzyme [151, 152]. Thus, it is possible that $Fe^{III}$-superoxo intermediate are a common mechanistic feature for both oxidase and oxygenase reactions.

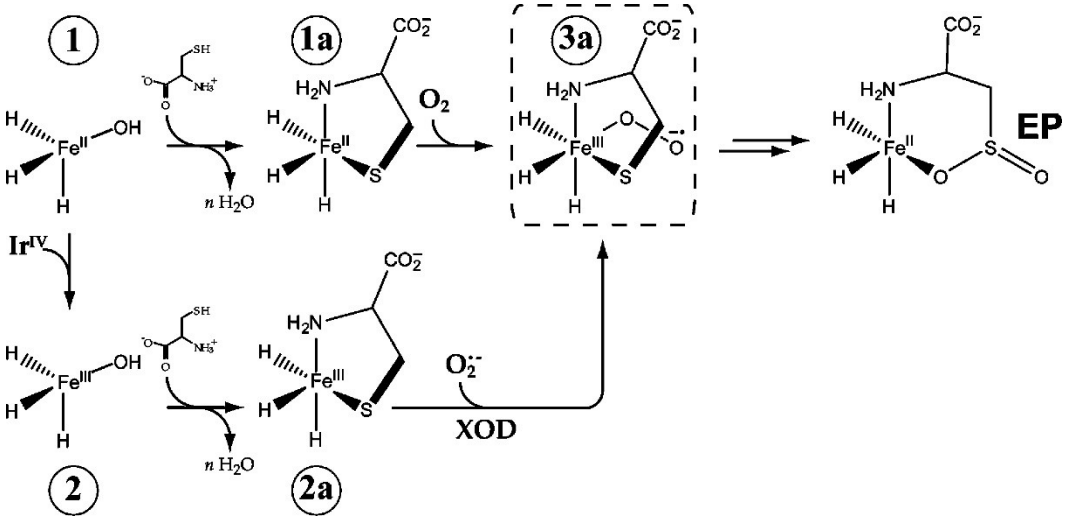


Scheme 2-1 Summary of Experiments.

The work presented here explores a chemical-rescue approach by which a putative substrate-bound $Fe^{III}$-superoxide species can be produced and spectroscopically characterized in CDO. A summary of the experiments performed is shown in Scheme 2-1. Briefly, samples of catalytically active $Fe^{II}$-containing enzyme (**1**) were oxidized by treatment with potassium hexachloroiridate, $K_2IrCl_6$, to produce a catalytically inactive, $Fe^{III}$-containing enzyme (**2**). Addition of Cys to samples of **2** produced the substrate-bound $Fe^{III}$-CDO species (**2a**) previously characterized by UV–vis, CD/MCD, and resonance Raman spectroscopy [153]. Within samples of **2a**, aqueous superoxide anions were generated by xanthine oxidase-catalyzed univalent $O_2$-reduction. In theory, superoxide can act as a suitable oxidant to accept the remaining three electrons required for CSA formation and regenerate the catalytically active CDO species **1**. Following introduction of $O_2^{\bullet-}$, an unusually long-lived intermediate (**3a**) ($t_{1/2}$ ~ 1.2 min) is observed by UV–vis and EPR spectroscopy. The decay of this intermediate is kinetically matched to CSA formation. Moreover, enzymatic activity of CDO is recovered upon

treating **2a** with superoxide. To our knowledge, this is the first reported instance of superoxide-rescue for a non-heme iron enzyme. Freeze-quenched samples of **3a** were characterized by EPR spectroscopy, and spectroscopic simulations indicate that **3a** is best described as an antiferromagnetically coupled $S_A = 5/2$ with $S_B = 1/2$ resulting in a ground state $S = 3$. Thus, the observed spin state of CDO intermediate **3a**is consistent with the assignment of a substrate-bound $Fe^{III}$-superoxide intermediate species, analogous to the initial step (**B**) of the proposed reaction mechanism for CDO-catalyzed thiol-oxidation shown in Figure 2-2.

## Materials and Methods

### *Purification of CDO*

Overexpression and purification of recombinant mouse CDO enzyme was performed with minor modifications to the procedure previously described.[104] In a typical purification, ~30 g of *E. coli*BL21(DE3) cell paste was thawed in 100 mL of lysis buffer (25 mM HEPES, pH 8.0). To the resulting slurry, 10 mg of lysozyme and 2 mg each of RNase and DNase (Sigma-Aldrich, St. Louis, MO) were added. The slurry was then mixed by hand on ice for 20 min prior to pulsed sonication for 10 min. Following sonication, the suspension was centrifuged for 1 h at 40000*g* at 4 °C to remove cell debris. The supernatant was diluted 1:1 with the lysis buffer and loaded onto a DEAE Sepharose anion exchange column pre-equilibrated in lysis buffer. The anion exchange column was washed with one column volume of wash buffer (25 mM HEPES, 30 mM NaCl, pH 8.0) prior to gradient elution from 50 to 350 mM NaCl. The fractions were pooled based on CDO activity as determined by TLC assay (described below) and the presence of the maltose binding protein–CDO fusion (MBP–CDO) observed by SDS PAGE. The pooled fractions were concentrated to approximately 5–10 mL using an Amicon stir cell equipped with an YM-30 ultrafiltration membrane. Tobacco etch virus

protease (TEV) was used to cleave CDO from the fusion protein (4 h ambient temperature) in 50 mM HEPES, 100 mM NaCl, 0.3 mM tris(2-carboxyethyl)phosphine hydrochloride (TCEP), pH 7.5. A Sephacryl S-100 size exclusion column was used to separate MBP from CDO in 25 mM HEPES, 50 mM maltose, 150 mM NaCl, pH 7.5. The purified CDO enzyme was assayed for iron content as previously described, and protein content was determined by Bio-Rad protein assay. In a typical preparation, Fe-incorporation within CDO is approximately 50–60% relative to protein concentration. Since adventitious iron binding to CDO could potentially interfere with spectroscopic characterization, iron reconstitution was not attempted. Therefore, the concentrations reported for all experiments reflect the concentration of ferrous iron within samples of CDO. When normalized for $Fe^{II}$ content, the Michaelis–Menten parameters ($k_{cat}$ and $K_M$) determined for product formation were 2.2 $s^{-1}$ and 3 mM, respectively ($V/K \sim 730\ M^{-1}\ s^{-1}$). These values are consistent with those previously reported for CDO [104, 153]. Batches of CDO used in these experiments typically contain ~80% C93–Y157 as determined by SDS PAGE densitometry. The freely available software ImageJ was used for analysis of SDS PAGE densitometry.

*TLC CDO Activity Assay*

Following column purification, fractions were selected based on qualitative CDO activity determination by thin-layer chromatography (TLC). From selected fractions a 50 µL aliquot was taken and placed in a 37 °C incubator. L-Cysteine was added to this solution for a final concentration of 10 mM. At 0, 15, and 30 min, 1 µL of the reaction was spotted onto a silica gel 60 F254 TLC plate (VWR) alongside 5 mM L-cysteine and cysteine sulfinic acid standards. After spotting the sample on the TLC plate a heat gun was used to completely dry the plate prior to elution for 20 min using a mobile phase of 20:20:60 (v/v) $H_2O$, acetic acid, and *n*-butanol, respectively. Following elution, the

solvent front was marked and the plate was dried by a heat gun. The TLC plate was stained with ninhydrin (3 g of ninhydrin, 200 mL of ethanol, 6 mL of acetic acid) and developed by a heat gun.

*HPLC CDO Activity Assay*

The rate of cysteine sulfinic acid formation was determined by HPLC by a modified version of the method previously described [104]. Briefly, 1 μM CDO enzyme was allowed to react aerobically with L-cysteine for up to 30 min at 37 °C in 25 mM HEPES, 50 mM NaCl, pH 7.5. Samples were taken at selected time points for determination of L-cysteine and cysteinesulfinic acid concentration by reverse phase HPLC using 99.4:0.6 (v/v) water:methanol with 1% heptafluorobutyric acid, pH 2.0, as the mobile phase. Each sample aliquot was filtered by 0.22 μM cellulose acetate membrane (Corning, Spin-X) prior to analysis on HPLC. Injections (50 μL) were eluted at a flow rate of 1.0 mL/min on a Phenomenex Kinetex 2.6 μm C18 100 Å column (100 × 4.6 mm) and detected at 218 nm. HPLC samples were analyzed using a Dionex UltiMate 3000 HPLC equipped with a 3000 variable wavelength detector. The concentration of CSA produced in steady-state assays was determined by comparison to a 7-point standard curve (0.1–10 mM CSA) run in parallel with kinetic samples.

*Anaerobic Work*

All anaerobic samples were prepared in a glovebox (Coy Laboratory Products Inc., Grass City, MI) with the $O_2$ concentration maintained below 1 ppm. Solutions were degassed on a Schlenk line prior to transferring into the anaerobic chamber. Analytical grade argon was passed through a copper catalyst (Kontes, Vineland, NJ) to remove trace $O_2$ impurities and then sparged through distilled water to hydrate the gas.

*$K_2IrCl_6$ Oxidation of $Fe^{II}$-CDO*

Solutions of potassium hexachloroiridate [$K_2IrCl_6$] (15 mM) were prepared in aerobic buffer (25 mM HEPES, 50 mM NaCl, pH 8.0). In a typical reaction, a slight molar excess of hexachloroiridate (3 equiv per enzyme) was added to samples of CDO. This solution was allowed to equilibrate for 30 min at 4 °C prior to Sephadex G-25 gel filtration [1.5*D* × 15*L*] to remove excess iridium species. Both Sephadex G-25 size exclusion and DEAE Sepharose anion exchange resins were found to be equally effective in removing residual iridium species from treated proteins samples. Following gel filtration, the iron content within samples of $Fe^{III}$-CDO was determined as described elsewhere. Enzymatic inactivation by potassium hexachloroiridate treatment was confirmed by HPLC and TLC assays as described above.

*Addition of Superoxide to Substrate-Bound $Fe^{III}$-CDO*

Xanthine oxidase (Sigma, St. Louis, MO) was used to generate superoxide anions by univalent reduction of oxygen using a modified version of the method described by Fridovich et al [154-156]. Briefly, a buffer containing 50 mM HEPES, 50 mM NaCl, 150 μM L-cysteine, 6 μM xanthine, pH 8.2 was sparged for 1 h with pure $O_2$ gas at 20 °C. CDO was added to this solution to obtain a final concentration 100 μM $Fe^{III}$-CDO within a quartz cuvette. Each reaction was initiated by spiking 0.4 units of xanthine oxidase into the cuvette using a Hamilton gastight syringe. Decay of the substrate-bound $Fe^{III}$-CDO was followed spectrophotometrically at 650 nm, and the amount of CSA produced in these reactions was determined by HPLC. Sample aliquots (200 μL) were taken directly from the cuvette at selected times (1–10 min). Each aliquot was immediately heat denatured at 95 °C and filtered by a spin-X centrifugal filter (Corning) to remove the precipitated protein. HPLC samples were prepared and analyzed as described above. LC-MS analysis of selected HPLC samples was

performed as secondary confirmation of CSA product formation. The amount of superoxide produced by xanthine oxidase in the conditions described above was determined by monitoring the reduction of cytochrome *c* (Sigma, St. Louis, MO) by UV–vis spectroscopy (550 nm) according to published methods [156, 157]. Catalase and superoxide dismutase (Sigma, St. Louis, MO) were added for control reactions to confirm the specificity of the cytochrome *c* assay for superoxide.

*Spectroscopy*

All UV–vis measurements were performed on an Agilent 8453 photo diode array spectrometer (Santa Clara, CA). Sample temperature was held constant by a 13 L circulating water bath and an Agilent thermostatable cell holder (89054A) with magnetic stirrer. All measurements were made in ES Quartz cuvettes (NSG Precision Cells, Farmingdale, NY). X-band (9 GHz) EPR spectra were recorded on a Bruker (Billerica, MA) EMX Plus spectrometer equipped with a bimodal resonator (Bruker model 4116DM). Low-temperature measurements were made using an Oxford ESR900 cryostat and an Oxford ITC 503 temperature controller. A modulation frequency of 100 kHz was used for all EPR spectra. All experimental data used for spin quantitation were collected under nonsaturating conditions.

Analysis of the EPR spectra utilized the general spin Hamiltonian

$$\hat{H} = JS_A S_B + D\left(\hat{S}_Z{}^2 - \frac{S(S+1)}{3}\right) + E(\hat{S}_X{}^2 + \hat{S}_Y{}^2) + \beta BgS$$

where D and E are the axial and rhombic zero-field splitting (zfs) parameters, *g* is the *g*-tensor, and J is the Heisenberg-exchange constant [158]. EPR spectra were simulated and quantified using Spin Count (ver. 3.1.2), created by Professor M. P.

Hendrich at Carnegie Mellon University. The simulations were generated with consideration of all intensity factors, both theoretical and experimental, to allow for determination of species concentration. The only unknown factor relating the spin concentration to signal intensity was an instrumental factor that is specific to the microwave detection system. However, this was determined by the spin standard, Cu(EDTA), prepared from a copper atomic absorption standard solution purchased from Sigma-Aldrich.

## Results

### *Production of $Fe^{III}$-CDO (2)*

As discussed in the Materials and Methods section, samples of resting $Fe^{II}$-CDO (termed CDO species **1**) were treated with a slight excess of potassium hexachloroiridate(IV) ($E_m$ = +870 mV) [159-161] for 30 min on ice. Excess iridium species were removed by Sephadex G25 gel filtration. Following treatment of **1** with $K_2IrCl_6$, the catalytic activity of CDO is essentially zero. However, enzymatic activity is fully restored (~95% relative to as-isolated enzyme) upon reduction with hydroxylamine or sodium dithionite mediated by methyl viologen. This result indicates that $K_2IrCl_6$oxidation of CDO is reversible and does not adversely affect the integrity of the enzyme. No evidence was obtained by either EPR or UV–vis spectroscopy to suggest the presence of adventitious iridium within treated samples of CDO.

Prior to the addition of substrate, the UV–vis spectrum of the $Ir^{IV}$-treated enzyme (termed **2**) is indistinguishable from the resting enzyme. However, as shown in Figure 2-3, addition of Cys produces an intense ligand to metal charge transfer (LMCT) band at 650 nm. This band is consistent with the oxidized substrate-bound enzyme (**2a**) which has been previously characterized by UV–vis, CD/MCD, resonance Raman spectroscopy, and supporting DFT calculations [153]. CDO species **2a** is very stable,

showing only minor decay (<10%) in the observed absorbance at 650 nm over 30 min at ambient temperature, thus suggesting that Cys is not capable of rapidly reducing the ferric enzyme. On the basis of the aforementioned spectroscopic work, the active site geometry of **2a** is believed to approximate that of the active ferrous enzyme prior to the binding of $O_2$.

Deprotonation of the Cys ammonium and thiol groups is necessary for direct coordination of Cys to CDO species **2**. Therefore, it is reasonable that the formation of **2a** would be pH-dependent. A pH profile was conducted to determine the optimal pH for the binding of Cys to **2**. In these experiments, 150 μM samples of **2** were prepared within an appropriate Good's buffer (100 mM) [MES (p$K_a$ 6.1), HEPES (p$K_a$ 7.5), and CHES (p$K_a$ 9.3)] over a pH range of 5.5–9.5. To each sample, a substoichiometric amount of Cys (0.7 equiv per **2**) was added and allowed to equilibrate at 4 °C for 15 min. The amount of **2a** produced was measured spectrophotometrically at 650 nm. Additionally, aliquots of **2a** were prepared for analysis by EPR spectroscopy (discussed below). The extinction coefficient of **2a** was determined by dividing the recorded absorbance at 650 nm observed by UV–vis spectroscopy by the concentration of **2a** determined by EPR spin-quantitation. Using this approach, a more accurate determination of the **2a**extinction coefficient was obtained ($\varepsilon_{650}$ = 2200 $M^{-1}$ $cm^{-1}$). As indicated by Figure 2-3 (inset), CDO species **2** shows an optimal binding of Cys at pH 7.4 with ~95% of the total Cys added producing **2a**. No appreciable change in the extinction coefficient of **2a** was observed within the pH range of these experiments.

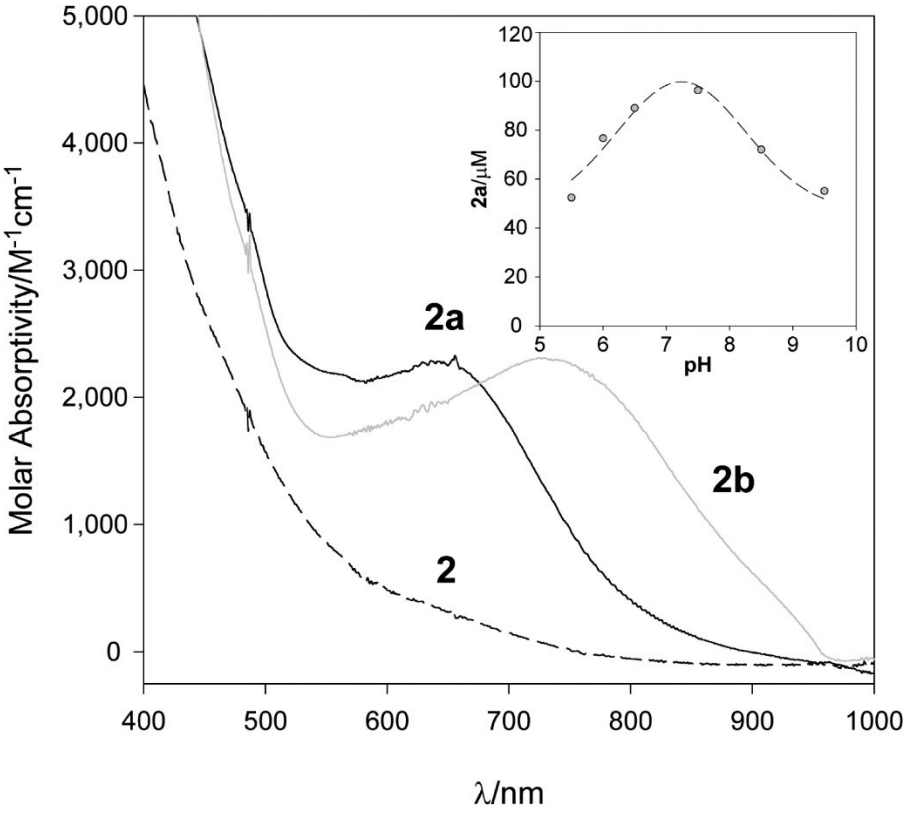


Figure 2-3 UV–vis spectrum of.FeIII-CDO.
UV–vis spectrum of $Fe^{III}$-CDO (**2**) [dashed line], Cys-bound $Fe^{III}$-CDO (**2a)** [solid black line], and Sec-bound $Fe^{III}$-CDO (**2b**) [solid gray line] in 25 mM HEPES, 50 mM NaCl, pH 7.8. Inset: optimal pH for Cys binding to $Fe^{III}$-CDO (**2**) as observed by UV–vis spectroscopy.

As shown in Figure 2-4 A, the X-band EPR spectra of 2 exhibits an isotropic resonance at $g \sim 4.3$ and a much weaker resonance at $g \sim 8.3$ (spectrum i, top). The $g \sim 4.3$ feature originates from the middle doublet of a high-spin rhombic (E/D ~ 1/3) ferric iron ($S$ = 5/2) center, whereas the $g \sim 8.3$ feature can be attributed to overlapping resonances within the lowest and highest lying doublets of the $S$ = 5/2 spin system. Spin-quantitation of spectrum i accounts for ~95% of the total iron within the sample as determined spectrophotometrically. On the basis of this spectrum alone, it is difficult to determine if the observed ferric iron resides within the active site of CDO or is

adventitiously bound to the protein. However, upon addition of a slight excess Cys (1.5 equiv per species 2), spectrum i is completely converted to spectrum ii (bottom). The observed spectra (ii) show unusually sharp rhombic features at $g_{x,y,z}$ = 4.47, 4.36, and 4.27 as well as a set of weaker resonances at $g \sim 9.7$. The shift in the observed *g*-values for EPR spectra ii as compared to i can be attributed to the direct coordination of Cys to the iron site. The full conversion of spectrum i to ii upon addition of Cys indicates that all of the ferric iron observed by EPR spectroscopy must reside within the active site of CDO. On this basis, the signal observed for EPR spectra ii is assigned to the Cys-bound $Fe^{III}$-CDO (2a). A quantitative simulation (dashed line) for 2a is overlaid on spectrum ii in Figure 4B. On the basis of this simulation, the concentration of 2a was determined. The magnitude of the axial-zero field splitting term ($|D| = 2.7\ cm^{-1}$) for 2a was determined by fitting the temperature normalized intensity of the gave = 4.4 signal (inset) to a Boltzmann population distribution for a three-level system. Table 2-1 lists all the relevant spectroscopic parameters for 2a determined from EPR simulation. As expected, the direct S-atom coordination to the high-spin ferric iron site results in increased spin–orbit coupling of 2a as compared to typical non-heme iron ferric centers. This is clearly reflected by the amount of microwave power required for half-saturation of the $S = 5/2$ EPR signal ($P_{1/2}$ = 90 mW).

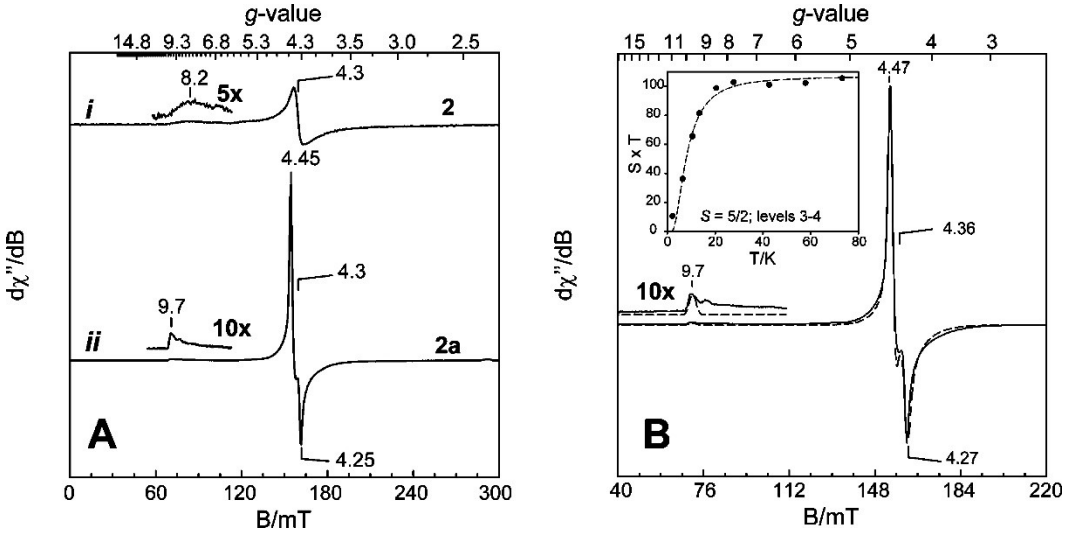


Figure 2-4 EPR spectra of $Fe^{III}$-CDO.
(A) 10 K X-band EPR spectra of CDO $Fe^{III}$-CDO (spectrum i, 2) and Cys-bound $Fe^{III}$-CDO (spectrum ii, 2a). (B) Quantitative EPR simulation (dashed line) overlaid on spectrum ii (solid line).

Table 2-1 Spectroscopic Parameters for Substrate-Bound Oxidized CDO Species

| parameter | ($Fe^{III}$-Cys) 2a | ($Fe^{III}$-Sec) 2b | ($Fe^{III}$-X$^{\bullet}$) 3a |
|---|---|---|---|
| $S$ | 5/2 | 5/2 | 3 |
| $g_{x,y,z}$ | 2.08, 2.00, 1.98 | 2.09, 2.00, 1.99 | ~2.00 |
| $\|D\|$ ($cm^{-1}$) | 2.7 | 2.5 | 0.13 |
| $E/D$ | 0.31 | 0.30 | 0.10 |
| $\sigma_D$ ($cm^{-1}$) | 0.02 | 0.02 | <0.01 |
| $\sigma_{E/D}$ | 0.06 | 0.05 | 0.03 |
| $J$ ($cm^{-1}$) | | | –8 ± 3 |
| $\sigma_B$ ($cm^{-1}$) | 0.9 | 0.9 | 0.9 |
| $P_{1/2}$ (mW), 10 K | 90 | 195 | 25 |
| λ (nm) | 630 | 740 | 565 |
| ε ($M^{-1}$ $cm^{-1}$) | 2200 ± 300 | 2300 ± 300 | n/d |

The binding of selenocysteine (Sec) to **2** was performed as an additional control to confirm that the $Fe^{III}$-CDO produced by treatment with $K_2IrCl_6$ is equivalent to the minor fraction of $Fe^{III}$-CDO previously characterized by resonance Raman and CD/MCD spectroscopy [153]. Shown in Figure 2-3 is the UV–vis spectrum of the Sec-bound $Fe^{III}$-

CDO (termed **2b**) for comparison to **2a**. As previously reported, the $Fe^{III}$–Sec LMCT band for **2b** is significantly red-shifted relative to the $Fe^{III}$-Cys LMCT for **2a**. However, as indicated by Table 2-1, the EPR spectroscopic properties of **2b** showed only modest deviations from **2a**. The nearly identical zfs parameters of **2a** and **2** bindicate that the binding geometry of Cys and Sec to the active site of $Fe^{III}$-CDO are essentially identical. However, the half-power microwave saturation obtained for **2b** ($P_{1/2}$ = 195 mW) is nearly twice that observed for **2a** at the same temperature (10 K). Collectively, these experiments clearly demonstrate that the Se-atom of Sec is directly coordinated to the ferric site of CDO. Moreover, these observations are consistent with the results obtained from previous published CD/MCD spectroscopic work [153].

*Addition of Superoxide Anion to Substrate-Bound $Fe^{III}$-CDO (**2a**)*

It has been previously demonstrated that xanthine oxidase (XO) can be utilized to catalyze the univalent reduction of $O_2$ to produce superoxide anion ($O_2^{\bullet-}$) within an aqueous solution [154, 155]. Indeed, under appropriate conditions (basic conditions, substoichiometric xanthine concentration, and saturating $O_2$), XO is capable of converting a significant fraction of the oxygen present in solution into superoxide [154]. The most common method for detection of superoxide anions involves the spectrophotometric determination of cytochrome *c* reduction [157]. Using this procedure, the apparent second-order rate constant for superoxide-dependent cyt *c*reduction was determined to be ~1900 $M^{-1}$ $s^{-1}$. This value is consistent with previously published results. As an additional control, superoxide formation was confirmed by EPR spectroscopy using the ($O_2^{\bullet-}$/$^{\bullet}$OH) spin-trap (DEPMPO).

In these experiments, XO was used to produce a steady-state concentration of superoxide in the presence of Cys-bound $Fe^{III}$-CDO (**2a**). For each reaction, a buffered solution (150 μM L-cysteine, 10 μM xanthine, pH 8.2) was sparged with pure $O_2$ for 1 h at

20 °C. Oxidized CDO (**2**) was added to the solution for a final **2a** concentration of 100 μM as confirmed by UV–vis spectroscopy. Production of superoxide was initiated by addition of 0.4 units XO under constant mixing at 20 °C.

As illustrated in Figure 2-5A, addition of XO to samples of **2a** in the presence of 6 μM xanthine and saturating $O_2$ resulted in formation of a new transient species (termed **3a**) with observable features at 485 and 565 nm. Complete loss of **2a** was observed within 5 s following addition of XO. Alternatively, the subsequent decay of **3a** was significantly slower. Given the competition between XO-dependent superoxide formation and the apparent consumption of superoxide by **2a**, the observed kinetics for this reaction are complicated. To simplify interpretation, the XO solution was premixed with xanthine and $O_2$ and allowed to react for 60 s prior to mixing with **2a**. This preincubation step allows superoxide to build up to a steady-state concentration prior to addition of **2a**, thus forcing the reaction into an apparent first-order regime. Other than the order of addition, all reagent concentrations remain constant. As illustrated in Figure 2-5B, incorporation of a 60 s premixing step simplifies the observed kinetics to an apparent first-order reaction in which only the decay of **3a** is observed. The decay of **3a** observed by UV–vis spectroscopy (black circles) can be reasonably fit assuming a single-exponential decay ($k_{obs}$ = 0.6 $min^{-1}$). Given the relatively slow rate of **3a** decay, aliquots of this reaction were pulled at selected time points (1–10 min) for heat inactivation at 95 °C and analysis by HPLC. The determination of CSA formation was performed as described within the Materials and Methods section. For clarity, the scale for the ordinate is normalized for simultaneous comparison of UV–vis and HPLC results (Figure 2-5C). In these experiments, CSA formation (gray circles) is observed concomitant with the decay of **3a** (black circles). Selected reaction samples were analyzed by LC-MS for independent confirmation of correct product (CSA) formation.

To confirm that the CSA produced is not the direct product of Cys oxidation by $O_2^{\bullet-}$, control XO reactions were prepared containing excess Cys, but lacking **2**. However, no detectable amounts of CSA were observed within the time scale of these experiments (10 min). Moreover, addition of excess superoxide dismutase (SOD, 5 units) or known ($O_2^{\bullet-}$ and $^{\bullet}OH$) trapping reagents (DEPMPO, 10 mM) to XO reactions completely abolishes formation of the **3a** intermediate and CSA. Addition of catalase (5 units) to XO reactions appeared to decrease the rate of CSA formation slightly (~13%); however, it has been previously demonstrated that, in addition to $H_2O_2$, catalase also reacts readily with superoxide anions [162-164]. Therefore, as an additional control, $H_2O_2$ (200 μM) was directly added to samples of **2a** to determine if it is (in part) responsible for the formation of CSA. However, no detectable amounts of CSA or **3a** were observed in these reactions. On the basis of these results, it can be reasonably concluded that only superoxide is reacting with **2a** to produce the physiologically relevant product (CSA) and the observed **3a** intermediate.

As illustrated in the superoxide-rescue pathway shown in Scheme 2-1, the formation of CSA by addition of $O_2^{\bullet-}$ to **2a** should also return CDO to its catalytically active state (**1**, $Fe^{II}$-CDO). Thus, the catalytic activity of CDO should be recovered following treatment with XO. Indeed, samples collected after 10 min treatment with XO showed 60% specific activity as compared to the as-isolated enzyme.

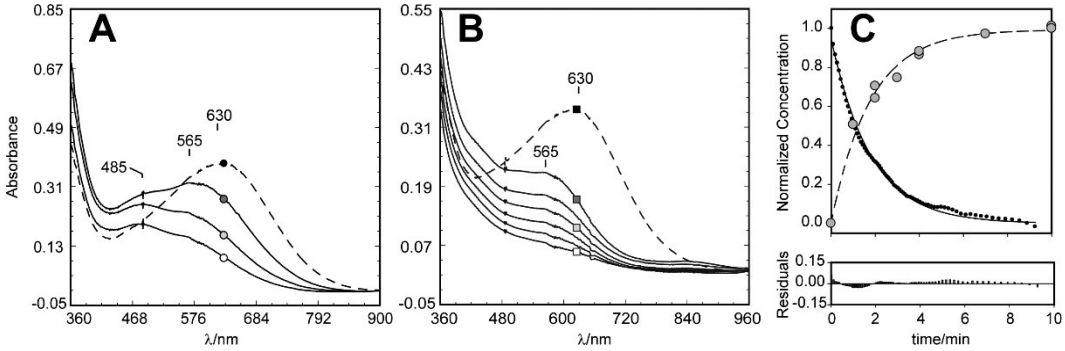


Figure 2-5 UV-vis and HPLC characterization of $Fe^{III}$-CDO.
(A) Time-dependent change in the observed UV–vis spectrum of **2a** following addition of XO. The absorbance of **2a** before addition of XO is shown (A, B) by the dashed line. The circles (●, shaded ○, and ○) indicate spectra taken at 0.5, 1.0, and 2 s, respectively. (B) Time-dependent UV–vis spectra of **2a** upon addition of premixed (~60 s) XO solution. The squares (■, shaded □, and □) indicate spectra taken at 0.5, 22, and 600 s, respectively. (C) Aliquots of reaction were taken at 0, 2, 3, 4, 7, and 10 min for CSA determination by HPLC. Data were fit to a single exponential to obtain an apparent first-order rate constant (*k*obs = 0.6 min–1). In multiple experiments (*n* = 5), 1.1 ± 0.2 mol equiv of CSA is produced per **2a** within 10 min.

Superoxide can act as a mild reductant in aqueous solutions [$E(O_2/O_2^{\bullet-})$ = −0.16 V vs NHE] [165, 166]. Therefore, one possible explanation for the reactivation of CDO and subsequent product formation is that $O_2^{\bullet-}$ reduces **2a** to produce **1a** and 1 mol equiv of $O_2$. Rapid rebound of **1a** with the resulting $O_2$ would then initiate product formation via the native CDO reaction pathway. To explore this possibility, CDO species **2** was exposed to superoxide in the absence of substrate as described above for **2a**. Following treatment for 15 min, the reaction was quenched by addition of SOD and catalase (5 units each). Cys was then added to samples, and the amount of **2a**produced was determined by UV–vis spectroscopy. Therefore, any reduction of **2** by $O_2^{\bullet-}$ would result in decreased **2a** formation; however, no discernible decrease in the amount of **2a**produced was observed relative to untreated enzyme. Moreover, $O_2^{\bullet-}$ treated **2** remains

catalytically inactive. Taken together, these results indicate that superoxide is not capable of reducing the oxidized enzyme.

*EPR Spectroscopy of Putative Substrate-Bound $Fe^{III}$-Superoxo CDO (3a)*

Given the slow decay of **3a** observed spectrophotometrically, EPR samples could be produced by hand-mixing reagents and freezing in liquid $N_2$ at selected time points. Samples were frozen over ~30 s to avoid breaking the quartz EPR tube during expansion of the freezing solution. Therefore, times specified refer to the time each sample was placed into the liquid $N_2$. The preparation of EPR samples was carried out as described for the above UV–vis experiments with the exception that the final **2a** concentration (before addition of XO) was increased to 160 μM. As observed by UV–vis experiments, the binding of superoxide to **2a** appears to be quite rapid. In samples frozen ~40 s after hand-mixing **2a** with XO, only trace amounts of **2a** could be observed in transverse mode ($B_1 \perp B$) EPR (data not shown). Spin-quantization reveals only ~10 μM **2a**corresponding to ~4% of the total iron in the sample. However, as shown in Figure 2-6A, a new signal can be observed at $g \sim 11$ (10 K, solid line) when the microwave field polarization is applied parallel to the static magnetic field ($B_1 \parallel B$). This signal exhibits inhomogeneous saturation behavior with a $P_{1/2}$ of 25 mW at 10 K. The observed spectra for **3a** is consistent with a transition within a "non-Kramers" doublet from an integer-spin paramagnetic center.

As previously mentioned, treatment of CDO with $K_2IrCl_6$ results in stoichiometric conversion of all $Fe^{II}$ into $Fe^{III}$. Furthermore, neither superoxide nor Cys is capable of reducing $Fe^{III}$-CDO within the time scale of these experiments. Therefore, it is unlikely that this signal can be attributed to a high spin ferrous species ($S = 2$) spectroscopically distinct from the resting enzyme. It can also be argued qualitatively that the increased spin–orbit coupling from a ($d^6$) ferrous iron would significantly increase the electronic

relaxation rates. However, at 10 K the $P_{1/2}$ value obtained for **3a** is relatively close in magnitude to the substrate-bound $Fe^{III}$-CDO species (25 vs 90 mW, respectively). For comparison, microwave power saturation data collected for synthetic 4-coordinate Fe(II) complexes exhibit significantly greater $P_{1/2}$ values (490 mW) on the same instrumentation with equivalent temperature, modulation amplitude, scan rate, and time constant [167]. On the basis of these observations, it is argued henceforth that the likely Fe-oxidation state of **3a** is +III.

On the basis of simple electron count, a $Fe^{III}$-superoxo species would be the expected product for this reaction. Antiferromagnetic (AF, $J > 0$) or ferromagnetic exchange (F, $J < 0$) coupling of a high-spin ferric iron ($S_A = 5/2$) and a superoxide anion ($S_B = 1/2$) would result in a ground $S = 2$ or $S = 3$ spin state, respectively. The observed resonance for this intermediate species lies between the expected *g*-values for an idealized $S = 2$ ($g \sim 8$) or $S = 3$ ($g \sim 12$) species. Therefore, EPR spectroscopic simulations for F ($S = 3$) and AF ($S = 2$) configurations of **3a** were performed. These calculations employ least-squares analysis of spectra data to allow variation of spectroscopic terms (*g*-values, *D*, and *E*/*D*) and a distribution in the zero-field splitting terms ($\sigma_{E/D}$, and $\sigma_D$). As indicated by Figure 2-6A (dashed line) the spectrum of **3a** could be reasonably fit for the F configuration with the spectroscopic parameters given in Table 2-1. As expected for a $d^5$ ion, the *g*-values obtained by simulation show little deviation from the free electron *g* value ($g_e$= 2.0023). Simulations were also attempted assuming AF exchange; however a reasonable match to the observed **3a** spectra could not be obtained without invoking unreasonably high *g*-anisotropy ($\Delta g \sim 0.37$) for the Fe site. Moreover, the concentration predicted by the AF simulation was exceedingly low as compared to the F simulation (~50 μM). Given the half-life of **2a** observed by UV–vis

spectroscopy ($t_{1/2}$ ~ 70 s), the concentration of **3a** predicted by the F simulation (50 μM) is more consistent with the expected intermediate concentration when quenched at 40 s.

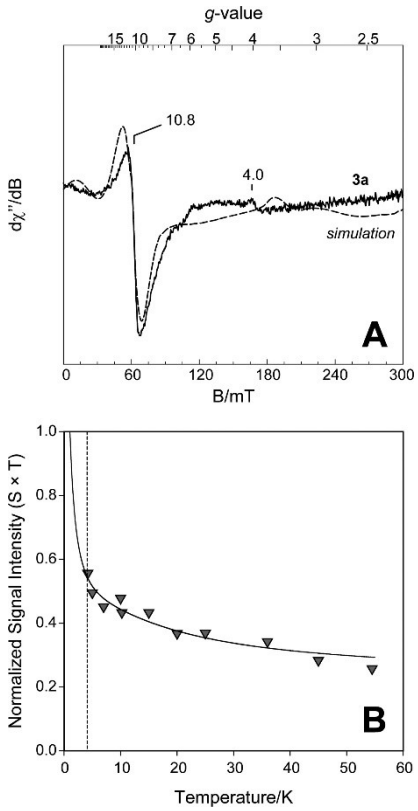


Figure 2-6 EPR characterization of $Fe^{III}$-CDO.
(A) Parallel mode X-band EPR spectra of **3a** produced following addition of XO to **2a**. A simulation (dashed line) for species **3a** is overlaid on the collected spectra (solid line). Instrumental parameters: temperature, 4.8 K; microwave frequency, 9.38 GHz; microwave power, 0.63 mW; modulation amplitude, 1.0 mT. Simulation parameters: $S$ = 3, $gx,y,z$ = 2.00; $|D|$ = 0.13 $cm^{-1}$; σ$D$ = 0.007 cm–1; $E/D$ = 0.10; σ$E/D$ = 0.03; σB = 0.9 mT. The concentration of **3a** determined by EPR simulation was ~50 μM (~30% of the total Fe-containing CDO). (B) Curie law normalized signal intensity (S × T) of **3a** as a function of temperature. The magnitude of the exchange coupling ($J$ = −8 ± 3 $cm^{-1}$; $H$ = $JSASB$) was determined by fitting the normalized signal intensity to the theoretical Boltzmann population (solid line) for a $S$ = 3 multiplet. The dashed-vertical line designates the lowest temperature limit of the cryostat.

As indicated by the gray triangles in Figure 2-6B, the temperature normalized signal intensity of **3a** is most intense at 4.2 K and decreases gradually with increasing temperature. This observation suggests that the $g \sim 11$ signal likely originates from either the ground- or a very low-lying doublet. As shown by the solid line in Figure 2-6B, the temperature-dependent behavior of **3a** can be well fit assuming ferromagnetic exchange coupling of $S_A$ and $S_B$ ($J = -8$ cm$^{-1}$) with a small, axial zero-field splitting ($|D| \sim 0.13$ cm$^{-1}$). This is in good agreement with the simulation for **3a** shown in Figure 2-6A. As indicated by the theoretical fits to the temperature-dependent signal intensity of **3a**, the exchange interaction ($J$) is significantly larger than the axial zero-field splitting term ($D$) for both of the proposed F configuration. In this strong-exchange limit ($J/D \gg 1$), the spin system can be treated as an isolated $S = 3$ multiplet.

## Discussion

### *Oxidation of CDO Active Site*

Previous spectroscopic work on $Fe^{III}$-CDO experiments relied on the presence of trace impurities of the catalytically inactive ferric enzyme [153]. However, batch to batch, the concentration of $Fe^{III}$-CDO is highly variable and often does not exceed 5% relative to the catalytically active ferrous enzyme. For this reason, potassium hexachloroiridate(IV) was used to chemically oxidize resting $Fe^{II}$-CDO (**1**) to produce the oxidized $Fe^{III}$-CDO (**2**). This reagent has been frequently employed in aqueous systems to oxidize various enzymes [161, 168]. Both enzymatic activity assays and spectroscopic (UV–vis/EPR) results confirm near full conversion of **1** to **2** is obtained under mild conditions by treatment with a slight molar excess of $K_2IrCl_6$ (3 equiv relative to the Fe-containing enzyme). Moreover, since essentially full activity of CDO is restored upon chemical reduction, Ir-oxidation of CDO occurs reversibly and without any discernible damage to the protein.

EPR spectroscopy of the Cys- (**2a**) and Sec-bound $Fe^{III}$-CDO (**2b**) indicates that both species exhibit near identical axial zero-field splitting (*D*) and rhombicity (*E*/*D*). This result is in good agreement with the spectroscopic characterization of these species by CD/MCD spectroscopy [153]. Moreover, the doubling of the half-power saturation behavior ($P_{1/2}$) of **2b** (195 mW) relative to **2a** (90 mW) and the red-shifted LMCT of **2b** relative to **2a** observed by UV–vis spectroscopy confirms direct ferric-iron coordination of the Se and S-atom of Sec and Cys, respectively. Interestingly, both of these observations are in contrast to the reported EXAFS data for the substrate-bound resting enzyme [169]. Although the binding of Sec and Cys to the active site of CDO is geometrically equivalent, it should be noted that only Cys serves as a competent substrate for CDO [153]. By all activity assays (TLC, HPLC), no indication of CDO-catalyzed Sec oxidation could be observed. It can be argued that this can be attributed to the rapid oxidation of Sec directly by $O_2$ to produce L-selenocystine and $H_2O_2$.

Given the direct coordination of the deprotonated thiolate of Cys ($pK_a \sim 8.3$) to the CDO active-site iron, it is not surprising that the pH optimum for Cys-binding to **2** is strongly pH-dependent. The observed optimum (pH ~ 7.5) for the formation of **2a** likely reflects the $pK_a$ of the Cys-thiol group when coordinated to the $Fe^{III}$-active site. This value is close to the optimal pH for enzymatic activity reported by Chai et al. (pH 7.5) but is significantly higher than reported by Simmons et al. (pH 6.1) [17, 18]. Surprisingly, there is a wide range of optimal pH values reported for CDO (6.1–9.0) in the literature [17, 18, 96, 170]. For batches of CDO described here, the pH-dependent steady-state rate of CSA formation agrees reasonably well with the observed pH optimum demonstrated for Cys-binding to the $Fe^{III}$-CDO (pH 8.0 and 7.5, respectively).

*Putative Ferric-Superoxide Intermediate (3a) of CDO*

In heme-containing enzymes, a variety of ferric-superoxide intermediates have been crystallographically and spectroscopically characterized [171-173]. However, few examples of such intermediates have been reported for non-heme iron enzymes [150, 174]. The EPR spectroscopic parameters determined for **3a** are in good agreement with the $Fe^{III}$-superoxo species (**Int-1**) reported for 2,3-HPCD with a few notable exceptions. First of all, the observed line width of **3a** is broader than for **Int-1** in 2,3-HPCD. While several factors contribute to line broadening in parallel mode EPR spectra, the most likely explanation for this difference is increased spin–orbit coupling due to the direct coordination of the Cys S-atom. The EPR signal for the **3a** intermediate in CDO is well fit assuming ferromagnetically coupling of a high-spin Fe(III) ion ($S_A$ = 5/2) with a radical, presumably $O_2^{\bullet-}$ ($S_B$ = 1/2). Both the magnitude of the axial zero field-splitting term ($D$) and isotropic $g$-values observed for **3a** are consistent with a $d^5$ ferric ion. Moreover, the small axial zero field splitting ($|D| \sim 0.13$ $cm^{-1}$) is in good agreement with the $D$ value reported for the nonheme iron $Fe^{III}$-superoxo species identified in 2,3-HPCD [150]. The magnitude of the spin exchange ($J$) is also comparable with the value reported for **Int-1** and suggests direct coordination of the paramagnetic centers. However, in contrast to the **Int-1** intermediate of 2,3-HPCD, **3a** exhibits ferromagnetic exchange ($J = -8$ $cm^{-1}$) coupling, giving rise to a ground state $S$ = 3 multiplet. Alternatively, the exchange coupling for **Int-1** is antiferromagnetic ($J = +6$ $cm^{-1}$), resulting in a ground state $S$ = 2 manifold. While the reason for this deviation is not yet clear, it can be speculated that this likely reflects a difference in the coordination geometry of the putative $Fe^{III}$-superoxo species in **3a** as compared to **Int-1** in 2,3-HPCD.

*Mechanistic Implications*

The experiments performed here demonstrate a chemical-rescue of the catalytically inactive substrate-bound $Fe^{III}$-CDO (**2a**) by treatment with superoxide ($O_2^{\bullet-}$). In many respects, the well-known peroxide-shunt pathway exhibited by both heme and non-heme monoxygenase enzymes can, to some extent, be thought of as a chemical-rescue for such enzymes lacking an electron-transport system. However, while chemical-rescue experiments have been performed on a variety of non-heme iron enzymes [175-177], to our knowledge, superoxide has not been previously utilized as a chemical trigger to study the activity of non-heme mononuclear iron activities. In contrast to the peroxide-shunt pathway, superoxide-rescue experiments do not produce steady-state catalysis. Instead, only a single turnover of the substrate-bound $Fe^{III}$-CDO and recovery of active $Fe^{II}$-CDO enzyme is observed.

One striking feature regarding the work presented here is the relatively long lifetime and high accumulation of the **3a** intermediate upon triggering with superoxide. The formation of **3a** following initiation of XO-dependent $O_2^{\bullet-}$ generation is very rapid, exhibiting full conversion of **2a** within 5 s. Therefore, the binding of $O_2^{\bullet-}$ to **2a** does not appear to be rate-limiting in UV–vis reactions. Interestingly, while the rate of **3a** decay and product formation ($k_{obs} \sim 0.6$ min$^{-1}$) are kinetically matched, this rate is nearly 200-fold slower than the steady-state rate of native CDO catalysis ($k_{cat} \sim 2.2$ s$^{-1}$). Since chemical reduction of **2a** yields active enzyme with catalytic efficiency ($V/K$) equivalent to untreated enzyme, oxidation of CDO by hexachloroiridate does not cause any irreversible damage to CDO. Therefore, the unusual stability of the **3a** intermediate suggests an inherent difference in the local environment of the iron-active site of **2a** relative to the untreated ferrous enzyme (**1a**). For example, a protein conformation change or a difference in the protonation state of a nearby residue. One argument for the unusually

long lifetime exhibited by this putative $Fe^{III}$-superoxide species can be made on the basis of the crystal structure for the putative persulfenate-bound enzyme shown in Figure 2-7 [144]. In this work it was observed that the Y157 hydroxyl group of CDO is at a favorable distance to form a hydrogen bond with the proximal O-atom of the putative persulfenate intermediate. In theory, this interaction could stabilize the bound superoxide anion, thus slowing its rate of attack on the Fe-bound Cys substrate. Several examples of stabilizing hydrogen bonding interactions to $Fe^{III}$-superoxo and $Fe^{III}$-peroxo species have been reported for both heme-containing and non-heme iron metalloproteins [171, 178-181].

Alternatively, the reaction pathway taken during native catalysis may be entirely divergent than that observed during superoxide-rescue experiments. If, for example, native catalysis in CDO follows a substrate-activating mechanism analogous to the $Fe^{III}$-dependent catechol dioxygenase, direct nucleophilic attack by the Fe-bound Cys-thiolate on molecular oxygen would precede CSA formation. The resulting thiadioxirane intermediate (Figure 2-2H) would bypass formation of a $Fe^{III}$-superoxide species entirely. Indeed, an analogous mechanism has been postulated for the "dioxygenase-like" behavior observed in 4-coordiante Ni(II)–thiolate complexes upon exposure to $O_2$ [145, 146]. However, this model is inconsistent with the observation that the substrate-bound resting enzyme readily binds nitric oxide to produce an unusual $\{Fe\text{-}NO\}^7$ ($S$ = 1/2) species [104]. The direct coordination of NO to the enzyme–substrate CDO complex implies that $O_2$ would also favor direct coordination to the Fe site as opposed to the S-atom of the bound Cys-thiolate. Regardless, without additional experimental information it is not immediately clear how the native and superoxide-rescue pathways deviate mechanistically. It should also be noted that, up to this point, it has been assumed that the $S_B$ = 1/2 site in **3a** is attributed to a superoxide anion. However, other possibilities cannot be excluded without supporting spectroscopic confirmation. Additional

characterization of **3a** using resonance Raman and Mössbauer spectroscopy is planned in order to unambiguously assign intermediate **3a**.

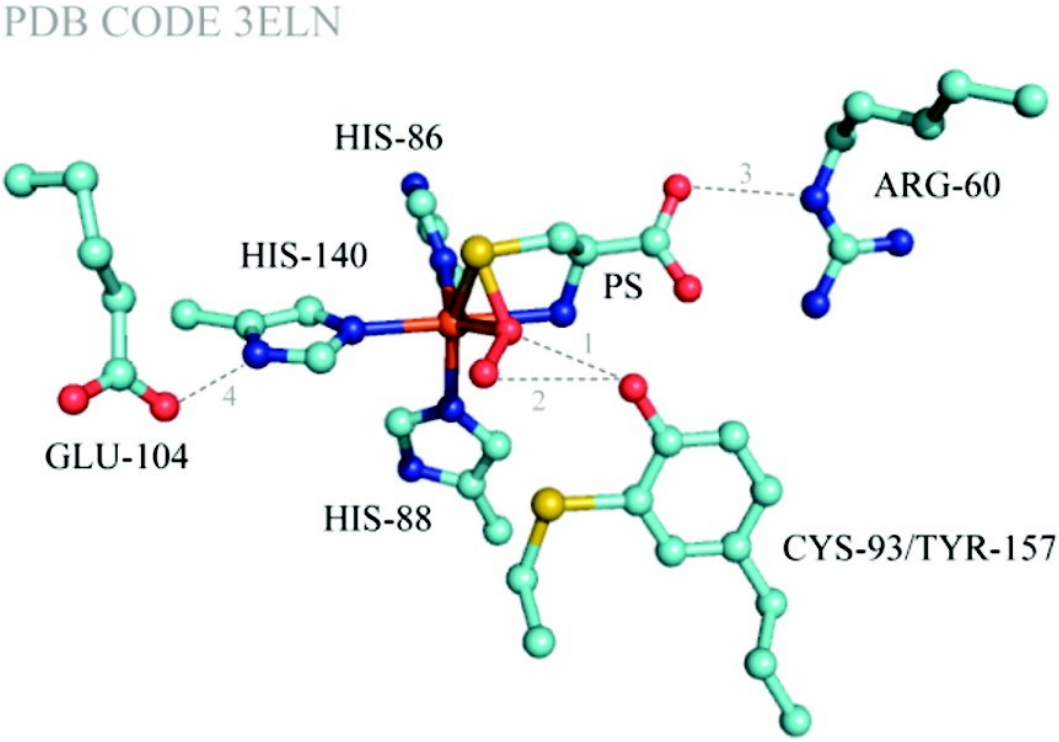


Figure 2-7 1.4 Å resolution crystal structure of the putative $Fe^{II}$-bound Cys-persulfenate.
1.4 Å resolution crystal structure of the putative $Fe^{II}$-bound Cys-persulfenate within the active site of CDO (pdb code 3ELN). Selected distances indicated by 1, 2, 3, and 4 are 2.8, 3.2, 2.9, and 2.7 Å, respectively.

In summary, the UV–vis and EPR spectroscopic characterization of **3a** provides a critical first glance at an intermediate species kinetically matched with product formation. While it is not clear if this transient species is produced within the native catalytic cycle of CDO, it offers a point of comparison to intermediates observed in other non-heme mononuclear iron enzymes. Given the similar electronic structure for **3a** in CDO and **Int-1** in 2,3-HPCD, it is tempting to speculate that CDO follows a similar mechanistic pathway as 2,3-HPCD, in which a $Fe^{III}$-superoxo intermediate facilitates

substrate oxidation instead of a high-valent $Fe^{IV}(O)$ intermediate as indicated by the upper pathway (I) of Figure 2-2.

Abbreviations

| | |
|---|---|
| CDO | cysteine dioxygenase |
| SOD | superoxide dismutase |
| Cat | catalase |
| XO | xanthine oxidase |
| Cys | L-cysteine |
| Sec | selenocysteine |
| CSA | cysteine sulfinic acid |
| HPLC | high performance liquid chromatography |
| EPR | electron paramagnetic resonance |
| DEPMPO | 5-(diethoxyphosphoryl)-5-methyl-1-pyrroline *N*-oxide. |

# Chapter 3

## Second-Sphere Interactions between the C93–Y157 Cross-Link and the Substrate-Bound Fe Site Influence the $O_2$ Coupling Efficiency in Mouse Cysteine Dioxygenase

### Introduction

Enzymes involved in sulfur oxidation and transfer are increasingly being recognized as potential drug targets for the development of antimicrobials and therapies for both cancer and inflammatory disease [182-185]. Ironically, while sulfur is considered one of the six primordial elements required during the early stages of biological evolution, mechanistic characterization of enzymes involved in sulfur metabolism is far from complete. The study of enzymes involved in mammalian sulfur metabolism has been of considerable medical interest recently because of the observation that patients suffering from neurological disorders, such as autism and Down syndrome, have significantly lower plasma concentrations of transsulfuration pathway and methionine cycle products [cysteine (Cys), homocysteine (HCY), glutathione (GSH), and S-adenosylmethionine (SAM)] [122, 123]. Imbalances in Cys metabolism have also been observed in a variety of other neurological disorders such as motor neuron disease, Parkinson's disease, and Alzheimer's disease [17, 124, 126]. These observations suggest a potential correlation between impaired sulfur metabolism, oxidative stress, and neurodegenerative disease [122]. Cysteine dioxygenase (CDO) and cysteamine (2-aminoethanethiol) dioxygenase (ADO) are the only known mammalian thiol dioxygenase (TDO) enzymes. TDO enzymes use a single Fe(II) ion within their active site to catalyze the $O_2$-dependent oxidation of sulfur-containing amino acid derivatives without the need for an external electron source. Of the TDO enzymes, CDO is the best characterized. Scheme 3-1 illustrates the reaction catalyzed by CDO. Until recently, the catabolic dissimilation of Cys to produce inorganic

sulfate, pyruvate, hypotaurine, and taurine was believed to be unique within the domain of eukaryotes [120, 186]. However, a number of bacterial TDO enzymes have now been identified, suggesting that the ability to oxidize excess thiols is advantageous for survival.

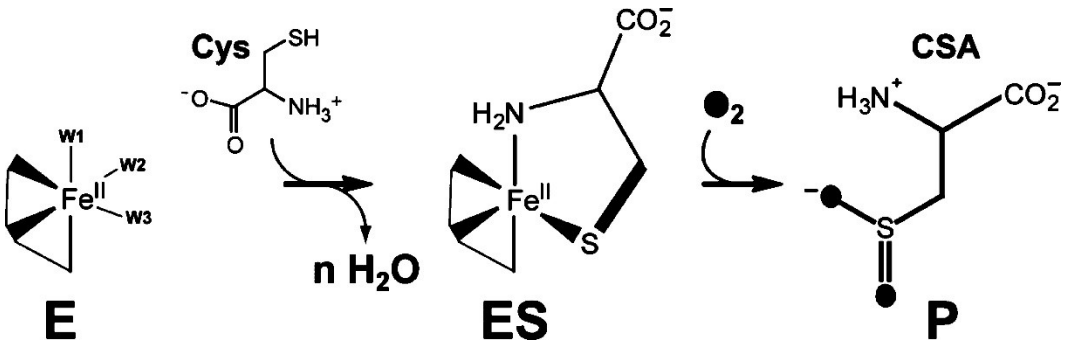


Scheme 3-1 Reaction Catalyzed by CDO.

While multiple high-resolution crystal structures of mammalian CDO have been determined [Protein Data Bank (PDB) entries 2ATF, 2B5H, and 2IC1] [17-19], mechanistic details are limited for this emerging class of enzymes. As illustrated in Figure 3-1, the active site of CDO contains a ferrous iron ligated by the Nε atoms of His86, His88, and His140, representing a new three-His variant on the classic two-His, one-carboxylate facial triad observed in mononuclear non-heme iron enzymes [2, 17, 98, 130]. Within the non-heme mononuclear iron family, only a handful of enzymes with a three-His active site motif have been crystallographically characterized [CDO, diketone dioxygenase (Dke1) [130], and gentisate 1,2-dioxygenase (GDO) [187]. However, on the basis of sequence homology, it has been proposed that ADO also contains a three-His non-heme iron active site [93].

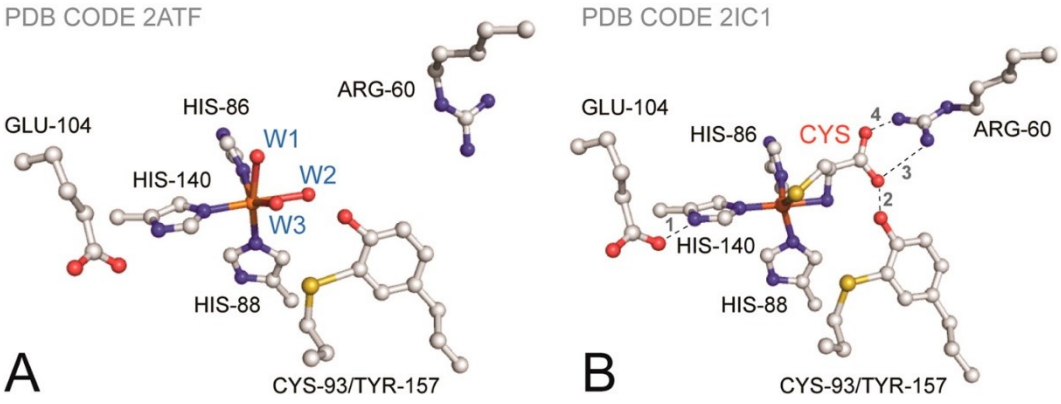


Figure 3-1 Crystal structure of resting CDO and substrate bound CDO. (A) Crystal structure (1.75 Å resolution) of resting CDO (PDB entry2ATF). Active site solvent ligands are designated W1–W3. (B) Crystal structure (2.7 Å resolution) of the substrate-bound CDO active site (PDB entry2IC1). Selected distances indicated by 1–4 are 2.70, 2.75, 2.88, and 2.27 Å, respectively.

The study of non-heme iron enzymes has historically attracted considerable interest in the realm of bioinorganic chemistry. This intense focus of research efforts can largely be explained by the vast number of functionally (and structurally) diverse non-heme iron enzymes identified throughout the biological kingdom, and the incredible versatility exhibited in chemical oxidations they initiate (mono- and dioxygenations, aliphatic desaturation, halogenations, and oxidative ring cyclizations) [6, 25, 188-191]. Remarkably, all of these divergent oxidations are facilitated by minor perturbations to what is essentially a conserved first coordination sphere to a mononuclear Fe(II) active site. With the notable exceptions mentioned above and the aliphatic halogenase enzyme (SyrB2), the typical Fe(II) coordination sphere observed for this class of enzymes is comprised of two protein-derived neutral His residues and one monoanionic carboxylate ligand provided by either an Asp or Glu residue. Because all protein-derived ligands occupy one face of an octahedron, the substrate/cofactor binding and $O_2$ binding occur at the opposite octahedral face of the two-His, one-carboxylate facial triad. Alternatively,

within the active site of SyrB2, a single chloride anion ($Cl^-$) replaces the protein-derived carboxylate ligand. This unusual Fe coordination is responsible for the "chloride rebound" mechanism resulting in chlorination of the terminal methyl group of amino acids covalently attached to peptidyl carrier proteins (PCPs) [15, 16]. As with other members of this enzymatic family, the Fe site within SyrB2 is also coordinated by a monoanionic ligand set. In contrast to this monoanionic facial triad motif, the active site of CDO (and potentially ADO) contains a neutral all-His (three-His) facial triad.

In addition to the three-His active site coordination, crystal structures of recombinant CDO reveal a covalently cross-linked cysteine–tyrosine pair (C93–Y157) within 3.3 Å of the iron center. To date, relatively few enzymes have been identified with an analogous post-translational modification [102, 131, 133, 192]. A number of theories have been proposed for the function of the C93–Y157 pair; however, self-oxidation of endogenous residues adjacent to oxidase and oxygenase non-heme iron centers is commonly observed. For example, the irreversible self-hydroxylation of Tyr73 within TauD during the $O_2$- and α-ketogluterate-dependent oxidation of taurine is responsible for oxidative inactivation of this enzyme over multiple catalytic turnovers [193, 194]. Similar self-oxidation behavior has been observed for the two-His, one-carboxylate non-heme iron enzymes prolyl-4-hydroxylase and lysyl hydroxylase [195-197]. By analogy to the self-hydroxylation pathway of TauD, it is possible that formation of the C93–Y157 pair in CDO is simply the result of uncoupled turnover and is not relevant to native catalysis. In apparent support of this hypothesis, it has been reported that the C93–Y157 cross-link forms over hundreds of catalytic turnovers in the presence of excess Fe, Cys, and $O_2$ [99]. Contrary to this hypothesis, the C93A variant of CDO, which is unable to produce the C93–Y157 cross-link, is catalytically active, albeit with decreased activity

[98]. Moreover, it has been previously demonstrated that the specific activity of wild-type CDO increases in a manner concomitant with C93–Y157 cross-link formation [99, 198]. In the face of these observations, it is clear that further investigation into the relevance of this enigmatic post-translational modification to native catalysis is necessary.

Among mononuclear dioxygenase enzymes, second-sphere residues are frequently employed to modulate the reactivity of transient Fe–oxo intermediates during catalysis. For example, within the active site of 2,3-dioxygenase, a second-sphere histidine residue (H200) has been identified to have a profound influence on the enzymatic steps following $O_2$ activation [199]. Indeed, selected H200 variants (H200F and H200N) exhibit increased transient intermediate stability [199, 200] and divergent substrate oxidation mechanisms (intradiol vs extradiol) relative to that of the wild-type enzyme [201]. By extension, it is reasonable to assume that second-sphere interactions also play a crucial role in regulating thiol oxidation by non-heme iron enzymes. Unlike C93, both Y157 and H155 are universally conserved among CDO enzymes [186]. Therefore, these residues make an attractive starting point for the exploration of key second-sphere interactions relevant to native CDO catalysis.

Conveniently, CDO can be prepared with variable amounts of the C93–Y157 cross-link present. For example, the as-isolated CDO (termed AI-CDO) typically contains ~50 ± 10% C93–Y157 cross-link as determined by sodium dodecyl sulfate–polyacrylamide gel electrophoresis (SDS–PAGE) densitometry. However, if the enzyme is allowed to turn over with excess L-Cys, a nearly quantitative yield of the C93–Y157 pair is generated within purified CDO. For the sake of clarity, the fully modified enzyme prepared by this method is designated α-CDO. Therefore, the influence of the C93–Y157 pair can be investigated within the wild-type enzyme by comparison of AI-CDO with α-

CDO. Selected CDO variants (C93A, Y157F, and H155A) were also prepared for comparison to the wild-type enzyme isoforms.

The efficiency at which an oxygenase enzyme incorporates 1 mol of $O_2$ into the product is commonly termed "coupling". In the steps following $O_2$ activation, unregulated access of solvent molecules to transient Fe–oxo intermediates generated prior to substrate oxidation often results in unproductive or uncoupled catalysis. The outcome of enzymatic uncoupling can result in oxidation of amino acid residues adjacent to the non-heme iron center, formation of reactive oxygen species (ROS), and ultimately enzymatic inactivation [196]. As a general rule, to limit enzymatic uncoupling, oxygenase enzymes utilize second-sphere interactions to tightly regulate solvent access within the active site. As illustrated in Figure 3-1, the distance separating the second-sphere C93–Y157 hydroxyl group from the carboxylate group of the Fe-bound substrate (L-Cys) is 2.75 Å. However, as stated previously, the relevance of this second-sphere interaction to native catalysis is poorly understood. In this work, the steady-state rate of CSA formation and $O_2$ consumption were simultaneously monitored to explore the effect of the C93–Y157 post-translational modification on native catalysis and $O_2$/CSA coupling efficiency for CDO.

In practice, CSA/$O_2$ coupling experiments are useful for the identification of key enzyme–substrate interactions relevant to native catalysis. However, once identified, more sophisticated methods are needed to develop a "molecular-level" understanding of these substrate–enzyme interactions. Therefore, complementary EPR experiments were performed utilizing the catalytically inactive $Fe^{III}$–CDO species in which cyanide was used as a spectroscopic probe to monitor the effect of the C93–Y157 pair on the electronic structure of the substrate-bound active site. Here, the strong π-accepting character of cyanide is exploited to produce a low-spin cyano/substrate-bound $Fe^{III}$–CDO complex.

To aid in the interpretation of these EPR spectra, as well as to gain further insight into the electronic structure of the active site in the absence or presence of the C93–Y157 cross-link, we used whole-protein QM/MM computational models and DFT calculations. Together, the kinetic, spectroscopic, and computational results all lend support to the hypothesis that the cross-link plays a vital role in CDO-mediated catalysis.

## Materials and Methods

### *Purification*

Recombinant mouse CDO (EC 1.13.11.20) was expressed in *Escherichia coli* BL21(DE3) pLysS competent cells (Novagen) and purified as previously described [104, 108]. Tobacco etch virus protease (TEV) was used to cleave CDO from the maltose binding protein (MBP) fusion protein (4 h at ambient temperature) in 50 mM HEPES, 100 mM NaCl, and 0.3 mM tris(2-carboxyethyl)phosphine hydrochloride (TCEP) (pH 7.5). Subtractive Ni-IMAC (GE Healthcare, 5 mL HiTrap IMAC FF) was used to separate MBP from CDO. The concentration of CDO protein was determined using the published extinction coefficient at 280 nm (28300 $M^{-1}$ $cm^{-1}$) [198]. Because incorporation of Fe within AI-CDO is variable from batch to batch (60–80%), each preparation was assayed for both ferrous and ferric iron spectrophotometrically as described previously [104, 153]. In a typical preparation of CDO, 90–95% of the iron is observed as ferrous. For the sake of clarity, the concentrations reported in enzymatic assays reflect the concentration of ferrous iron within samples of CDO ($Fe^{II}$–CDO). The fraction of CDO containing the C93–Y157 thioether linkage was determined by SDS–PAGE densitometry using the freely available ImageJ software (http://rsbweb.nih.gov/ij/index.html). AI-CDO prepared from a 10 L fermentation typically contained 50 ± 10% C93–Y157 cross-link as observed by SDS–PAGE. Broad-range protein molecular weight markers (catalog no.

V8491) utilized in SDS–PAGE experiments were purchased from Promega (Madison, WI).

All CDO variants (C93A, Y157F, and H155A) were prepared using the QuikChange Lightning Site-Directed Mutagenesis kit (Agilent Technologies). Mutagenic primers were purchased from Integrated DNA Technologies (https://www.idtdna.com), and sequence verification of single-amino acid mutations was performed by Sequetech (Mountain View, CA).

*Conversion of AI-CDO to Fully Modified CDO (α-CDO)*

Typically, ~100–200 μM AI-CDO was added to a buffered solution [25 mM HEPES and 50 mM NaCl (pH 7.5)] containing excess Cys (25 mM). This solution was allowed to react for ~30 min at 37 °C, prior to buffer exchange with a Sephadex G-25 desalting column or overnight dialysis at 4 °C. Following buffer exchange, the protein was concentrated using an Amicon $N_2$ stirred cell equipped with an YM-10 ultrafiltration membrane (Millipore). The ferrous and ferric iron content and complete C93–Y157 cross-link formation were confirmed spectrophotometrically and by SDS–PAGE, respectively, as described above. The specific activity of all CDO preparations was verified as described below.

*HPLC CDO Activity Assay*

Cysteinesulfinic acid (CSA) was assayed using a modified version of the HPLC method described previously [104]. The mobile phase [20 mM sodium acetate, 0.6% methanol, and 1% heptofluorobutyric acid (pH 2.0)] was altered to compensate for a change in the reverse-phase column (Phenomenex Kinetex C18, 100 Å column, 100 mm × 4.6 mm, 2.6 μm). Sample injections (50 μL) were eluted isocratically at a flow rate of 1.0 mL/min and detected at 218 nm. This modification to the HPLC method resulted in greater column retention of CSA, allowing for separation of CSA from the void volume. In

a typical assay, 1 μM CDO was added to a solution of L-Cys (0.1–25 mM) under aerobic conditions at 37 °C. Aliquots were taken from each reaction mixture at selected time points and reactions quenched by spin filtration (0.22 μm cellulose acetate membrane; Corning, Spin-X) prior to HPLC analysis. This HPLC method was also used to monitor hypotaurine formation in CDO assays utilizing cysteamine (CSH) as a substrate. The concentration of CSA and hypotaurine was determined by comparison to standard calibration curves (0.1–20 mM).

*Oxygen Electrode*

The dioxygen concentration was determined polarographically using a standard Clark electrode (Hansatech Instruments, Norfolk, England) within a jacketed 2.5 mL cell at 37 ± 2 °C. The electrode was bathed in a saturated solution of KCl and separated from the buffer using a gas-permeable membrane. The electrode was calibrated by measuring the deflection in the voltage upon addition of ~500 units of catalase (Sigma-Aldrich, St. Louis, MO) to a buffer with a known concentration of $H_2O_2$ ($\varepsilon_{250}$ = 16.7 $M^{-1}$ $cm^{-1}$). Once the reaction had reached completion, the amplitude for the change in voltage was used to determine a response factor for the electrode. As an additional control, the stability of the electrode response factor was verified for each pH used in steady-state assays (pH 5–11) by addition of sodium dithionite to aerobic buffer. Enzymatic reaction mixtures were made by adding 1 mL of reaction buffer (25 mM Good's buffer and 50 mM NaCl) containing Cys (0.1–25 mM) to the electrode cell under continuous aerobic mixing. The reaction was initiated by injection of CDO, resulting in a final enzyme concentration of 1 μM.

*pH Profile Results*

For steady-state analysis, 1 μM CDO was allowed to react with different concentrations of Cys in 25 mM HEPES and 50 mM NaCl (pH 7.5) at 37 °C. For

experiments conducted over a broad pH range, the CDO solution was exchanged into an appropriate Good's buffer selected on the basis of its p$K_a$ (MES, p$K_a$ 6.1; HEPES, p$K_a$ 7.5; CHES, p$K_a$ 9.3). Each buffer was prepared at 25 mM and titrated to the desired pH using 1 N NaOH. As with steady-state reactions, 1 μM CDO was allowed to react with 20 mM Cys in 25 mM HEPES and 50 mM NaCl at 37 °C. Amounts of CSA produced and $O_2$ consumed were quantified by HPLC and oxygen electrode assays, respectively.

*Analysis of Kinetic Data*

Steady-state kinetics of wild-type and variant CDO were analyzed by SigmaPlot version 11 (Systat Software Inc., Chicago, IL). In the absence of substrate inhibition, initial rate data for CSA formation and O2 consumption were fit to the Michaelis–Menten equation to obtain kcat and $K_M$. In all assays, initial rates are normalized for Fe-containing CDO (v0/[E]). Under conditions of substrate inhibition, initial rate data were fit to equation 3-1 to determine the dissociation equilibrium or inhibition constant (KI).

$$v_0 = \frac{k_{cat}[S]}{K_M + [S] + \frac{[S]^2}{K_I}} \quad \textbf{(3-1)}$$

*Spectroscopy*

All UV–visible measurements were performed on an Agilent (Santa Clara, CA) 8453 photo diode array spectrometer. The sample temperature was held constant by a 13 L circulating water bath and a thermostable cell holder (89054A) with a magnetic stirrer. All measurements were taken in ES Quartz cuvettes (NSG Precision Cells, Farmingdale, NY). X-Band (9 GHz) EPR spectra were recorded on a Bruker (Billerica, MA) EMX Plus spectrometer equipped with a bimodal resonator (Bruker model 4116DM). Low-temperature measurements were taken using an Oxford ESR900 cryostat and an Oxford ITC 503 temperature controller. A modulation frequency of 100 kHz was used for

all EPR spectra. All experimental data used for spin quantitation were collected under nonsaturating conditions.

Analysis of the EPR spectra utilized the general spin Hamiltonian

$$\hat{H} = \mathbf{D}\left[\hat{S}_Z^{\,2} - \frac{S(S+1)}{3}\right] + \mathbf{E}(\hat{S}_X^{\,2} + \hat{S}_Y^{\,2}) + \beta\mathbf{B}\cdot\mathbf{g}\cdot\mathbf{S} \quad \textbf{(3-2)}$$

where **D** and **E** are the axial and rhombic zero-field splitting (zfs) parameters, respectively, and ***g*** is the ***g***-tensor.(45) In case of low-spin ferric iron ($S$ = $^1/_2$), eq 3-2 simplifies to the following equation:

$$\hat{H} = \beta\mathbf{B}\cdot\mathbf{g}\cdot\mathbf{S} \quad \textbf{(3-3)}$$

EPR spectra were simulated and quantified using Spin Count (version 3.1.2), written by M. P. Hendrich at Carnegie Mellon University (Pittsburgh, PA). The simulations were generated with consideration of all intensity factors, both theoretical and experimental, to allow for the determination of species concentration. The only unknown factor relating the spin concentration to signal intensity was an instrumental factor that is specific to the microwave detection system. However, this was determined by a spin standard, Cu(EDTA), prepared from a copper atomic absorption standard solution purchased from Sigma-Aldrich.

The half-power microwave saturation ($P_{1/2}$) for these signals was determined using SpinCount according to eq 3-4.

$$\frac{S}{\sqrt{P}} = \frac{A}{\left(1 + \frac{P}{P_{1/2}}\right)^{b/2}} \quad \textbf{(3-4)}$$

The software performs least-squares fitting of the normalized derivative signal intensity (*S*) as a function of microwave power (P). The A term represents the normalized maximal signal amplitude. The variable b is a spectroscopic inhomogeneity factor that is characteristic of the spin packet of the observed resonance. Generally, the signal packet derived from frozen solutions and powders exhibits inhomogeneous line broadening behavior (b = 1).

*Computational Methods*

A quantum mechanics/molecular mechanics (QM/MM) approach as implemented in Gaussian09 was utilized in the optimization of full-protein models of mouse CDO. For the QM region, density functional theory (DFT) was employed in conjunction with Becke's three-parameter hybrid exchange functional with the Lee–Yang–Parr correlation functional (B3LYP) [202, 203], as well as the 6-31G basis set [204] on all atoms except iron, its immediately ligated atoms, and the $CN^-$ ligand (for which TZVP [205] was used instead). For the MM portion of the calculation, the Amber95 force field [206] was utilized. The QM/MM boundary was placed between the β- and α-carbons of the appropriate residues, using hydrogens as the link atoms. The α-carbons of the QM residues were held fixed during the optimization process.

The starting coordinates for the models investigated were derived from two X-ray crystal structures, namely, PDB entry 2IC1 [98] for the QM region and PDB entry 3ELN [144] for the MM region residues. The cyanide ligand was manually added to the iron(III) center trans to H86, at an Fe–C distance of ~2 Å. Hydrogen atoms for the entire protein were added using Reduce version 3.14 [207]. On the basis of inspection of potential hydrogen bonding interactions, histidine residues at positions 86, 88, 140, and 155 were singly protonated at $N_\delta$, whereas all other histidines were singly protonated at $N_\varepsilon$. Residues R60, H86, H88, C93, H140, H155, and Y157 as well as Fe(III), L-Cys (or Sec),

$CN^-$, and six crystallographically defined water molecules within 10 Å of the iron center were included in the QM region. In the case of the model not containing the Cys–Tyr cross-link, the starting coordinates for the C93 side chain were adjusted to eliminate the bond between the residues and hydrogen atoms were added to both C93 and Y157 to restore them to a pre-cross-linked protonation state.

In the generation of small active site models, residues H86, H88, and H140 as well as Fe(III), the substrate (analogue), and cyanide were excised from the optimized protein coordinates. Amino acid residues were capped as methyl groups at their β-carbon, with C–H bond lengths of ~1.1 Å. Spin unrestricted single-point DFT calculations were conducted using Orca version 2.9 developed by F. Neese and used the same functional and basis sets as the QM/MM portion of the calculation. PyMOL version 1.5.0.4 was utilized to generate isosurface plots of relevant MOs using an isodensity value of 0.05 arbitrary unit. EPR parameters for these models were also computed with Orca version 2.9, using the PBE0 functional [208] (or B3LYP in a separate calculation for comparative purposes) in conjunction with the TZVP basis set on all atoms except sulfur, selenium, and iron [for which IGLOO(III) [209], CP(PPP) [209, 210], and CP(PPP), respectively, were used]. These calculations included all orbitals within ±100 hartree of the HOMO–LUMO gap, and the origin of the **g**-tensor was taken to be the center of the electronic charge. A high-resolution radial grid with an integration accuracy of 7 was used for the Fe, S, and Se atoms.

## Results

### *Purification of CDO Forms and Selected Variants*

Expression and isolation of the MBP–CDO fusion protein (Figure 3-2, lanes 2 and 3, respectively) were performed as previously described [104]. Shown in lane 4

are the two distinct CDO fractions (α and β) obtained from treating the as-isolated MBP–CDO fusion protein with tobacco etch virus (TEV) protease. For the sake of clarity, the expanded region shown in Figure 3-2B illustrates the two CDO isoforms (α and β) within AI-CDO. Previous experiments have confirmed that band α is the fraction of CDO enzyme with the covalent C93–Y157 pair, whereas the fraction within band β lacks this covalent modification [98, 99]. As demonstrated in Figure 3-2, by comparing lane 4 to lane 5, we observed that nearly 100% α-CDO can be produced from β-CDO within 30 min by addition of excess L-Cys (25 mM) to isolated batches of AI-CDO (100–200 μM) at pH 7.5. This is consistent with previous reports that the C93–Y157 pair is produced over multiple turnovers with the substrate [99, 198]. Unless otherwise stated, only fully modified CDO (Figure 3-2, lane 6) (α-CDO) will be used for the determination of steady-state kinetic parameters for the wild-type enzyme.

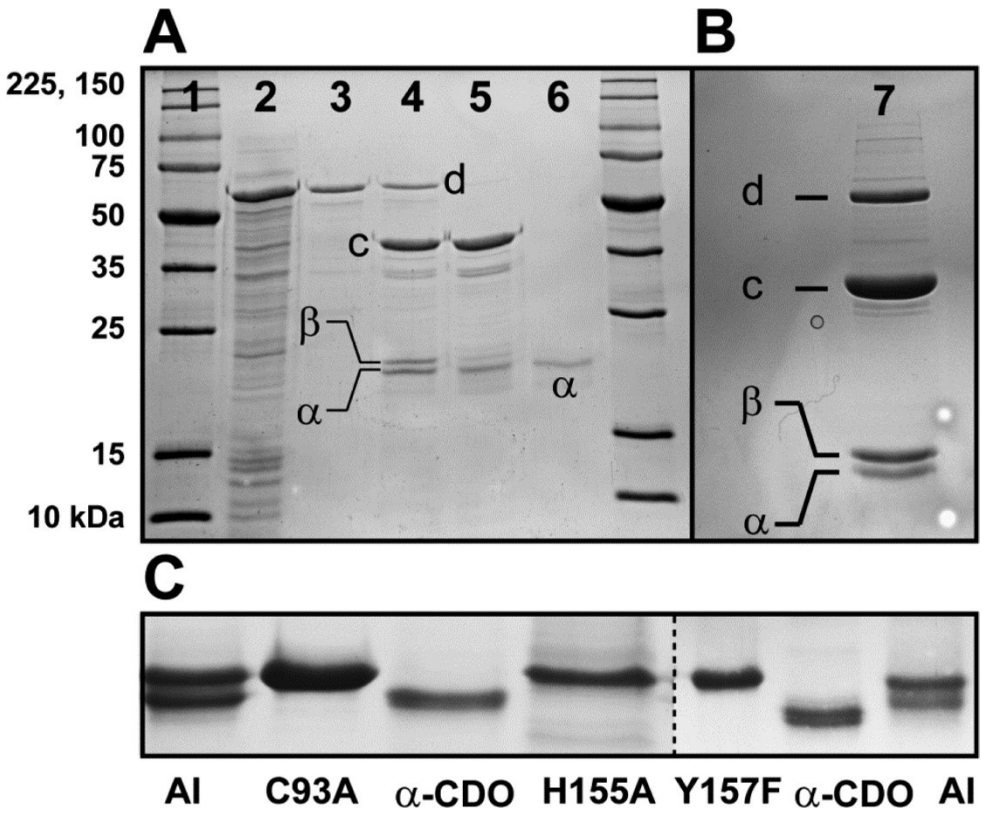


Figure 3-2 SDS-PAGE of wild-type CDO and mutants.
(A) SDS–PAGE (12%) of sequential α-CDO purification steps: lane 1, markers; lane 2, cell free extract; lane 3, purified MBP–CDO fusion protein; lane 4, MBP–CDO fusion protein following TEV protease cleavage (equivalent to lane 7 in panel B); lane 5, α-CDO produced following a 30 min treatment with excess l-Cys; lane 6, purified α-CDO following a subtractive Ni-IMAC column. (B) Lane 7 shows an expanded SDS–PAGE gel illustrating the two CDO isoforms (α and β) present in Al-CDO. The bands designated by c and d represent the cleaved maltose binding protein and the uncleaved fusion protein, respectively. (C) Migration of active site variants (C93A, H155A, and Y157F) relative to Al-CDO and α-CDO. The dashed line separates bands run on separate gels.

Because formation of the C93–Y157 pair may influence the steady-state kinetic parameters observed for CSA formation or CSA/$O_2$ coupling efficiency, active site variants incapable of C93–Y157 cross-link formation (namely, C93A and Y157F) were prepared to evaluate the role of the C93–Y157 pair in catalysis. Active site variants (C93A, H155A, and Y157F) were prepared using the Agilent QuikChange site-directed

mutagenesis kit as described in Materials and Methods. All variants were expressed, purified, and assayed for Fe content as described above for the wild-type enzyme. Figure 3-2C illustrates the migration of CDO active site variants (C93A, Y157F, and H155A) relative to the as-isolated and fully modified isoforms of wild-type CDO.

*Influence of the C93–Y157 Pair and Substrate Interactions on Enzymatic Coupling*

Because two forms of enzyme are present (α and β) within the as-isolated enzyme, the steady-state Michaelis–Menten kinetic parameters ($k_{cat}$ and $K_M$) determined for AI-CDO are not strictly valid. Therefore, coupling efficiencies were determined for α-CDO by comparing the steady-state kinetics of $O_2$ consumption to those of CSA formation. As described in Materials and Methods, $O_2$ consumption and CSA formation were measured using a calibrated Clarke-type $O_2$ electrode and reverse-phase HPLC, respectively. Unless otherwise noted, all initial rates are normalized for Fe-containing enzyme concentration ($v_0$/[E]), such that the values for $k_{cat}$ and $K_M$ are easily obtained from fitting the results to the Michaelis–Menten equation. The steady-state kinetics for wild-type CDO with L-Cys are shown in Figure 3-2A. The dashed line represents a best fit to the initial rate of $O_2$ consumption (●). From this analysis, the values of $k_{cat}$ and $K_M$ were determined to be 10.6 ± 0.4 $s^{-1}$ and 0.7 ± 0.1 mM for the steady-state rate of $O_2$ consumption, respectively. In terms of $O_2$ consumption, the catalytic efficiency ($V/K$) of α-CDO is ~15100 $M^{-1}$ $s^{-1}$. By comparison, from the steady-state kinetics for CSA formation (△, solid line), $k_{cat}$ and $K_M$ were determined to be 8.6 ± 0.5 $s^{-1}$ and 3.1 ± 0.6 mM, respectively ($V/K$ ~ 2900 $M^{-1}$ $s^{-1}$). As $k_{cat}$ represents the zero-order limit of an enzymatic reaction, the coupling efficiency can be obtained from the ratio of the $k_{cat}$ for CSA formation to the $k_{cat}$ for $O_2$ consumption. Therefore, the coupling efficiency for wild-type CDO with L-Cys is ~81 ± 5%. A summary of kinetic parameters and

CSA/$O_2$ coupling efficiency observed for wild-type CDO and selected active site variants is provided in Table 3-1. As previously stated, the steady-state kinetic parameters ($k_{cat}$ and $K_M$) for AI-CDO are not strictly valid; however, by comparison to that of α-CDO, it is readily apparent that the specific activity of CDO is proportional to the extent of the C93–Y157 pair present. This observation is consistent with previous reports [99, 198]. While the value obtained for $K_M$ (with respect to CSA formation) is consistent with those typically reported for recombinant CDO, the $k_{cat}$ for the α-CDO reported here is significantly higher than those reported elsewhere [18, 98, 104].

The pH dependence of CDO coupling was obtained by measuring the rate of CSA formation at a saturating Cys concentration (20 mM). As indicated by Figure 3-4, the optimal pH values for $O_2$consumption (●, pH ~8.2) and CSA formation (△, pH 8.6) do not fully overlap. Both data sets were fit to a three-parameter normal log peak equation. For the sake of clarity, the data were normalized to the maximal $k_{cat}$ observed for CSA formation at pH 8.6. Interestingly, the coupling efficiency is nearly fully coupled above pH 8.5; however, under more acidic conditions (pH ≤7), CDO appears to be significantly uncoupled, with ~25 ± 10% more $O_2$ consumed than CSA produced.

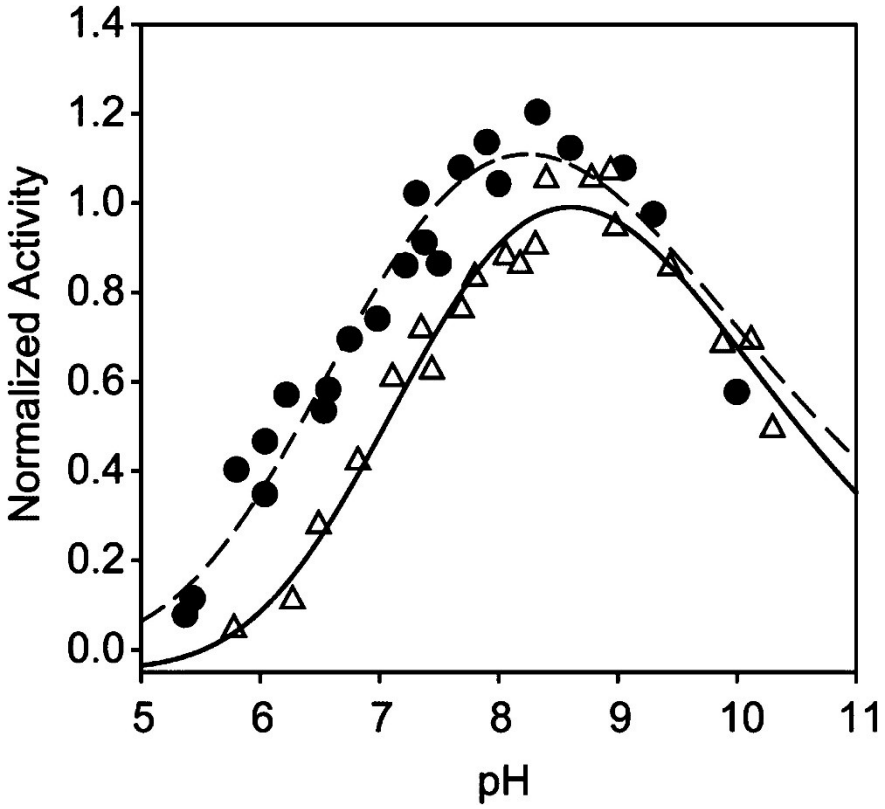


Figure 3-3.Steady-state analysis of WT CDO and C93A.
Steady-state kinetics of wild-type CDO-catalyzed O2 consumption (−−−) compared to those of product formation (—) for l-cysteine (A) and d-cysteine (B). For the sake of clarity, the steady-state curve for CSA formation as a function of initial d-Cys concentration is expanded in the inset of panel B.

Figure 3-4 pH profile of WT CDO.
pH dependence of CSA/O2 coupling efficiency for wild-type CDO with L-cysteine. For the sake of clarity, the initial rates observed for O2 consumption (●) and CSA formation (△) were normalized to the maximal rate of CSA produced at pH 8.6.

Such coupling experiments can frequently provide greater mechanistic insight into substrate–enzyme interactions. For example, the carboxylate group of l-cysteine can potentially make two stabilizing interactions with second-sphere residues within the CDO active site (Figure 3-1). First, the R60 guanidinium group is at a favorable distance (2.27–2.88 Å) to stabilize the substrate carboxylate charge. Additionally, it has been

proposed that the L-Cys carboxylate group may also form hydrogen bonding interactions with the nearby hydroxyl group of the C93–Y157 pair (2.75 Å). With a change in the stereochemistry of the substrate from l- to d-Cys, both H-bonding and electrostatic interactions would potentially be disrupted. As demonstrated in Figure 3-3B, in steady-state assays utilizing d-Cys, the maximal rate of O2 consumption (■, dashed line) increases by nearly 2-fold ($k_{cat}$ = 18.3 ± 0.9 s–1) relative to that of the native L-Cys substrate. Additionally, the $K_M$ for D-Cys increases to 9.1 ± 1 mM. Therefore, in terms of O2 consumption, the catalytic efficiency observed for α-CDO with d-Cys (V/K ~ 2000 M–1 s–1) decreases by >7-fold relative to that with L-Cys.

Table 3-1Steady-State Kinetic Parameters Determined for CSA Formation and O2 Consumption (CSA/O2) for Selected CDO Forms and Variants.

| Enzyme | $k_{cat}$ (s–1) (CSA/O2) | $K_M$ (mM) (CSA/O2) | $K_I$ (mM) (CSA) |
|---|---|---|---|
| fully modified | | | |
| l-cysteine | 8.6/10.6 (81%) | 3.1/0.7 | – |
| d-cysteine | 2/18.3 (4%) | 8/9.1 | 12 |
| as-isolated (AI-CDO) | 1.0–2.0 (CSA only) | 4.0 (CSA only) | – |
| C93A | 0.4/0.4 (45%) | 4/4 | 14 |
| H155A | <0.1 (CSA only) | not saturated at 25 mM | – |
| Y157 | – | inactive | – |

By contrast to what is observed for the steady-state formation of CSA from L-Cys, under identical assay conditions, α-CDO exhibits significant substrate inhibition with D-Cys [Figure 3-3B (◇)]. This decay is not observed in the rate of $O_2$ consumption, thus suggesting the formation of reactive oxygen species or self-hydroxylation during steady-state turnover. For steady-state assays exhibiting substrate inhibition, initial rates were fit to eq 3-1 (solid line) as described in Materials and Methods to obtain the kinetic parameters ($k_{cat}$ = 2 $s^{-1}$, and $K_M$ = 8 mM) and substrate inhibition constant ($K_I$ = 12 mM).

Given that the formation of CSA from D-Cys follows a more complicated substrate inhibition kinetic model, comparison of the $k_{cat}$ observed for CSA formation relative to that observed for $O_2$ consumption is no longer valid. For the sake of simplicity, the coupling efficiency for α-CDO with D-Cys was taken as the ratio of the initial rate observed for CSA formation over that observed for $O_2$ consumption at a fixed and saturating substrate concentration (20 mM). By this definition, the CSA/$O_2$ coupling efficiency for α-CDO with D-Cys is ~4%, essentially a 20-fold decrease relative to that with the native L-Cys substrate. A similar effect on oxidative uncoupling can also be observed in assays utilizing cysteamine (2-aminoethanethiol, CSH) as a substrate for α-CDO. Given the lack of a carboxylate group in CSH, the specific activity ($v_0$) of α-CDO at 20 mM CSH is vastly reduced (~0.02 $s^{-1}$ for hypotaurine formation) relative to that of the native substrate (~0.2 $s^{-1}$ for $O_2$ consumption). Moreover, the coupling efficiency (~6%) is close to that observed with D-Cys. Although coupling efficiencies have not been previously reported for this enzyme, the decreased specific activity observed for CDO with respect to D-Cys and CSH is consistent with the literature [95, 117-119].

The impact (if any) of the C93–Y157 post-translational modification was also interrogated by comparing the enzymatic activity and coupling efficiency of selected variants (C93A and Y157F) with those of the wild-type enzyme. As illustrated in Figure 3-2C, these variants are unable to produce the cross-linked pair. Interestingly, while C93 is not conserved among putative bacterial CDO enzymes, both Y157 and H155 are universally conserved [186]. Therefore, the H155A variant of CDO was also evaluated for comparison to wild-type α-CDO.

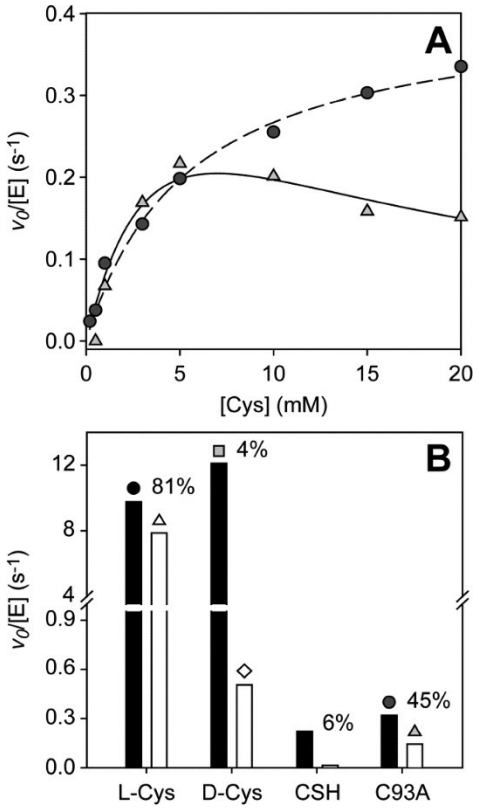


Figure 3-5 (A) Steady-state analysis of C93A and oxygen coupling. Steady-state kinetics of C93A CDO-catalyzed O2 consumption (●, −−−) compared to those of product formation (△, —) for l-cysteine. (B) Bar graph representing the CSA/O2 coupling efficiency for wild-type CDO with l- and d-cysteine and cysteamine (CSH) as compared to C93A CDO with l-cysteine.

Figure 3-5 shows that the C93A variant is catalytically active, albeit at a level significantly decreased relative to that of the wild-type enzyme. This observation is consistent with results obtained for a similar variant (C93S and C93A) in human and rat CDO [98, 99]. As with the wild-type enzyme, the rates of $O_2$ consumption and CSA formation are designated by a dashed line (●) and a solid line (△), respectively. Additionally, like wild-type CDO utilizing D-Cys as the substrate, the C93A variant exhibits behavior consistent with substrate inhibition, resulting in a rapid decay in the rate of CSA formation at saturating L-Cys concentrations. As observed previously, the decay in the

initial rate with an increasing substrate concentration is not observed for $O_2$ consumption, suggesting self-oxidation and/or production of reactive oxygen species. Steady-state assays of the C93A variant demonstrate a significantly lower maximal rate of $O_2$consumption ($k_{cat}$ = 0.4 $s^{-1}$) and Michaelis–Menten constant ($K_M$ = 4.4 mM) relative to those of the wild-type enzyme. Alternatively, the kinetic parameters obtained for the C93A variant in terms of CSA formation were 0.4 $s^{-1}$ ($k_{cat}$), 4.0 mM ($K_M$), and 13.5 mM ($K_I$). On the basis of this analysis, the CSA/$O_2$ coupling efficiency for the C93A variant is 43 ± 4%. Unlike experiments utilizing D-Cys or CSH, the carboxylate group of L-Cys is still present and available for interaction with R60. Therefore, the decreased level of coupling observed for the C93A variant can be attributed to disruption of second-sphere interactions with the C93–Y157 pair only. Figure 3-5B illustrates the coupling efficiency (percent) and observed $v_0$/[E] for $O_2$ consumption and CSA formation for the C93A variant as compared to those of the wild-type enzyme.

Although comparable to that of the wild-type enzyme in terms of iron incorporation, the specific activity of the H155A variant is nearly 2 orders of magnitude lower than that of the wild-type enzyme (~0.1 $s^{-1}$). Given its drastically reduced activity, the rate of product accumulation could reliably be measured only under saturating L-Cys conditions (25 mM). Isolated batches of the Y157F variant exhibited no detectable specific activity despite having appreciable ferrous iron incorporation and no visible signs of protein precipitation or denaturation.

*Cyanide Binding and EPR Spectroscopy of Substrate-Bound AI-CDO, α-CDO, and the C93A $Fe^{III}$–CDO Complexes*

In an effort to better understand the role second-sphere residues play in coupling and catalysis, the electronic structures at the active sites of catalytically relevant species of both isoforms of CDO were probed through the use of EPR spectroscopy. The parallel

mode X-band EPR spectra of the substrate-bound $Fe^{II}$–CDO complex are characteristic of high-spin ferrous iron ($S$ = 2) and easily differentiated from those of free hexaqua$Fe^{II}$ in solution. However, in cases of systems with large spin–orbit coupling (such as CDO), the zero-field splitting ($\Delta_k$) for the non-Kramers doublet ($k$) can exceed the incident microwave radiation ($\Delta_k \geq h\nu$) of the spectrometer. Therefore, at X-band frequencies ($h\nu \sim 0.3$ $cm^{-1}$), the majority of the resonance observed for the substrate-bound $Fe^{II}$–CDO complex is not observed even in the absence of an applied field ($B_0 = 0$) [211]. In such situations, higher microwave frequencies are necessary to observe the full paramagnetic spectra. Thus, the spectroscopic intractability of the $Fe^{II}$–CDO signal and the high oxygen sensitivity of the substrate-bound $Fe^{II}$–CDO complex make EPR characterization of the catalytically active enzyme challenging. However, it has been previously demonstrated that the $Fe^{II}$–CDO complex can be stoichiometrically converted to the $Fe^{III}$–CDO complex by being treated with potassium hexachloroiridate ($K_2IrCl_6$) [108]. While catalytically inactive, the ferric enzyme is more amenable to EPR spectroscopic characterization. In these experiments, cyanide ($CN^-$) was used as a spectroscopic probe to model the binding of $O_2$ to the substrate-bound $Fe^{III}$–CDO active site. The strong π-accepting character of cyanide was exploited to produce a low-spin ($S$ = $^1/_2$) cyano/substrate-bound $Fe^{III}$–CDO species. In principle, the resulting ternary complex would have a formal charge and size similar to those of the proposed $Fe^{III}$–superoxide intermediate in the CDO catalytic cycle [108]. Thus, the Fe-bound cyano ligand could serve as a spectroscopic probe for the observation of hydrogen bonding interactions or geometric perturbations arising from interactions with second-sphere active site residues such as the Y157 hydroxyl group of the C93–Y157 pair or the H155 imidazole ring [98, 144]. Unlike π-donors such as superoxide or nitric oxide that favor a bent Fe coordination geometry, bound cyano ligands typically exhibit a strong preference

for linear coordination. While this linear geometry is less desirable as a structural model for a putative $Fe^{III}$–superoxide intermediate, the use of cyanide as opposed to nitric oxide is spectroscopically cleaner as it prevents the production of dinitrosyl iron complexes (DNIC) ($g_{obs}$-values of 2.03, 2.02, and 2.01) and free nitric oxide ($g \sim 1.98$), both of which are observed at *g*-values comparable to those of the substrate-bound $\{Fe\text{-}NO\}^7$ ($S = {}^1/_2$) CDO site ($g_{obs}$-values of 2.07, 2.02, and 1.98) [104]. Moreover, the substrate-bound CN/Cys-bound $Fe^{III}$–CDO complex exhibits greater *g* spread ($\Delta g$) than the substrate-bound $\{Fe\text{-}NO\}^7$ CDO, thus offering greater sensitivity to second-sphere perturbations. As with the steady-state coupling experiments, the fully modified (α-CDO), as-isolated (AI-CDO), and C93A, Y157F, and H155A forms of the enzyme were characterized for comparison.

Prior to addition of KCN, EPR spectra for both the substrate-bound α-CDO and AI $Fe^{III}$–CDO enzymes exhibit a sharp signal with observed *g*-values of 4.47, 4.36, and 4.27. A weaker set of resonances can also be observed at $g \sim 9.7$ (Figure 3-6A). This signal is consistent with the high-spin ($S = {}^5/_2$) substrate-bound $Fe^{III}$–CDO species (termed $Fe^{III}$–ES) previously reported [108]. Indeed, within experimental error, both the half-saturation microwave power at 10 K ($P_{1/2} \sim 90 \pm 15$ mW) and the magnitude of the axial zero-field splitting term ($|D| \sim 2.7 \pm 0.3$ $cm^{-1}$) are equivalent for the $Fe^{III}$–ES prepared from α-CDO and AI-CDO.

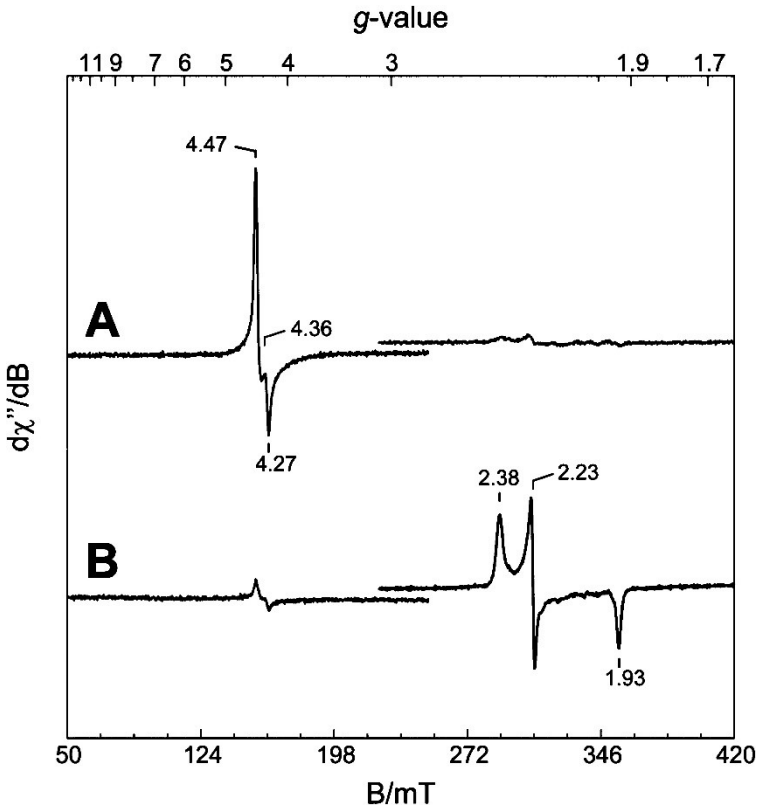


Figure 3-6 X-Band EPR spectra of α-Fe$^{III}$–ES after the addition of a KCN.

However, Figure 3-6B shows that addition of a 10-fold molar excess of KCN relative to the α-Fe$^{III}$–ES enzyme (0.15 mM) results in a nearly complete loss of the high-spin EPR signal with concomitant formation of a new rhombic $S = {}^1/_2$ signal. Substoichiometric additions of cyanide relative to the Fe$^{III}$–ES complex (0.5-fold molar excess) resulted in only minor formation of the $S = {}^1/_2$ signal (22% of total iron) (Figure 3-6A), thus indicating that the α-Fe$^{III}$–ES enzyme has a relatively poor binding affinity for the cyanide anion. As indicated by Table 3-2, the *g*-values for this$S = {}^1/_2$ signal (2.38, 2.23, and 1.93) and half-power microwave saturation at 10 K ($P_{1/2}$ = 140 ± 24 μW; *b* = 1.0) are consistent with those observed for a variety of low-spin non-heme ferric iron enzymes. A quantitative simulation (**S1**, dashed line) for α-Fe$^{III}$(CN)–ES is overlaid on

spectrum α in Figure 3-7. The spectral line width is dominated by *g* strain, and thus, simulations use distributions in the *g*-values along each principle axis ($\sigma g_1$, $\sigma g_2$, and $\sigma g_3$) to give the correct line width. On the basis of this simulation, the concentration of CN/Cys-bound $Fe^{III}$–α-CDO was determined, which accounts for 91% of the initial high-spin $S = {}^5/_2$ $Fe^{III}$–ES signal (150 μM). Thus, nearly all of the initial high-spin α-$Fe^{III}$–ES is converted to the corresponding low-spin α-$Fe^{III}$(CN)–ES adduct upon addition of a 10-fold molar excess of KCN.

Remarkably, in the absence of a substrate (L-Cys), no cyanide binding could be observed by EPR spectroscopy even following addition of a 100-fold molar excess of cyanide relative to enzyme. This apparent obligate ordered addition of substrate prior to cyanide has also been observed in experiments in which nitric oxide was used as a surrogate for $O_2$ binding. However, to the best of our knowledge, the obligate-ordered addition of substrate prior to cyanide has not been previously observed for other non-heme mononuclear iron enzymes.

As with the steady-state experiments, the AI-CDO used in these experiments has approximately 50% C93–Y157 cross-link (α) as indicated by SDS–PAGE densitometry. As shown in Figure 3-7, two spectroscopically distinct $S = {}^1/_2$ species can be observed in AI $Fe^{III}$(CN)–ES samples. As indicated by Figure 3-7, one of the $S = {}^1/_2$ species has *g*-values identical to those observed in samples of the CN/Cys-bound $Fe^{III}$–α-CDO complex (**S1**). However, an additional $S = {}^1/_2$ signal (**S2**) can be observed with *g*-values of 2.34, 2.21, and 1.95. The individual contribution of each species in the observed spectra was determined by quantitative simulation [**S1** (60%) and **S2**(40%) (dashed line)] and least-squares fitting. Because **S2** is observed only when it is prepared from AI-CDO, it is likely that this signal originates from the β fraction of the $Fe^{III}$–AI-CDO complex lacking the covalently cross-linked C93–Y157 pair (β-CDO). While the fraction of **S1** and **S2**

analytically determined by quantitative simulation slightly differs from the expected values obtained by SDS–PAGE, the values obtained are well within the error associated with gel densitometry. As additional confirmation of this assignment, samples of CN/Cys-bound $Fe^{III}$–CDO were prepared from the C93A variant. As indicated in Figure 3-7, only one low-spin ferric signal is observed with *g*-values (2.35, 2.22, and 1.94) nearly identical to those observed for **S2**. Additionally, the half-power microwave saturation at 10 K for the C93A CN/Cys-bound $Fe^{III}$–CDO complex is essentially equivalent to that observed for α-CDO ($P_{1/2}$ = 160 μW; $b$ = 1.0).

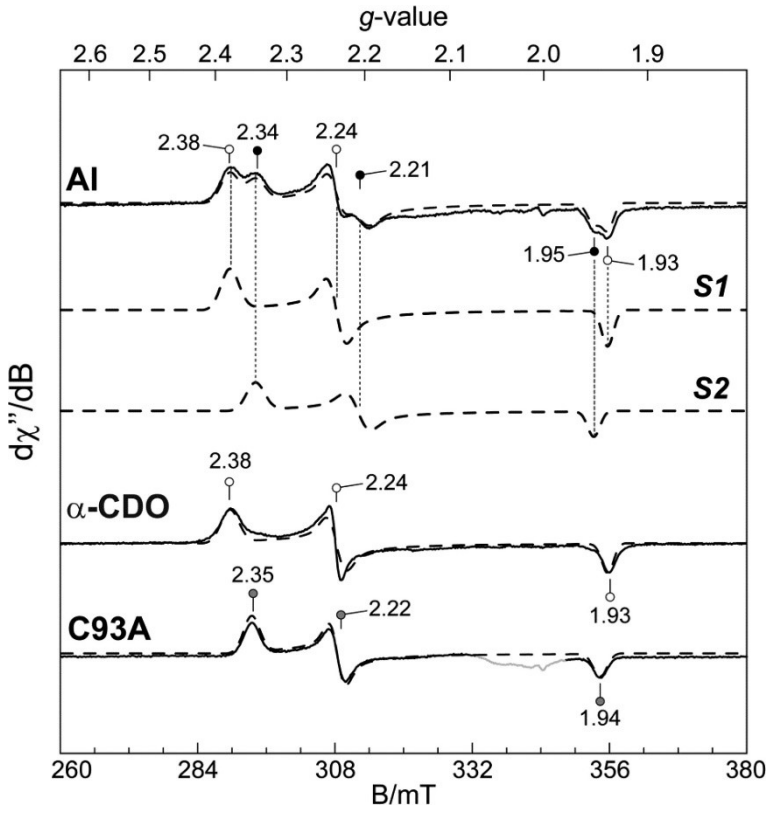


Figure 3-7 X-Band EPR spectra of the CN/Cys-bound $Fe^{III}$–CDO complex
X-Band EPR spectra of the CN/Cys-bound $Fe^{III}$–CDO complex prepared from as-isolated (AI), fully modified (α-CDO), and C93A CDO enzymes. EPR spectroscopic simulations (−−−) of **S1** and **S2** are overlaid on the spectra (—) for comparison. The component simulation to AI spectra is produced by two

spectroscopically distinct low-spin ferric ($S$ = $^1/_2$) sites. Instrumental parameters: microwave frequency, 9.64 GHz; modulation frequency, 100 kHz; modulation amplitude, 0.9 mT; temperature, 10 K; microwave power, 6 μW (45 dB). Simulation parameters are listed in Table 3-2.

Table 3-2 Simulation Parameters for the l-Cys-Bound, d-Cys-Bound, and l-Sec (CN/substrate)-Bound ($S$ = 1/2) $Fe^{III}$–CDO Samples.

| species | $g1$ | $g2$ | $g3$ | $\sigma g1$ | $\sigma g2$ | $\sigma g3$ |
|---|---|---|---|---|---|---|
| S1 (α) | 1.937 | 2.234 | 2.379 | 0.001 | 0.007 | 0.01 |
| S2 (β) | 1.951 | 2.208 | 2.343 | 0.023 | 0.01 | 0.01 |
| α-FeIII(CN/l-Cys) | 1.937 | 2.234 | 2.379 | 0.001 | 0.007 | 0.01 |
| α-FeIII(CN/d-Cys) | 1.932 | 2.243 | 2.384 | 0.015 | 0.015 | 0.023 |
| α-FeIII(CN/l-Sec) | 1.959 | 2.262 | 2.446 | 0.012 | 0.004 | 0.019 |

Interestingly, CDO variants Y157F and H155A, which exhibit no or vastly diminished catalytic activity, were also unable to bind cyanide in the substrate-bound $Fe^{III}$ oxidation state. Indeed, even at excess cyanide concentrations (100-fold molar excess, 15 mM) no low-spin ferric signals could be detected. Thus, on the basis of these experiments, the catalytic activity of CDO can be correlated to the ability of the substrate-bound enzyme to bind cyanide.

While it was originally developed for the study of heme metalloproteins and complexes, it is frequently useful to use the model initially developed by Griffith to analyze the EPR spectra of low-spin ferric complexes. This model assumes that the ligand field splitting separating the $t_{2g}$and $e_g$ orbitals is significantly large to prevent orbital mixing. By neglecting the influence of the unoccupied $e_g$ orbitals, a simplified model can be envisioned in which the tetragonal (Δ/λ) and rhombic ($V$/Δ) components of the $t_{2g}$ orbital splitting can be determined from the experimentally observed $g$-values [212]. (In this context, Δ refers to the tetragonal ligand field strength and not the zero-field splitting of a non-Kramers doublet.) Equations 3-5 and 3-6 show the relationships

developed by Taylor for the determination of *V*, Δ, on the basis of the observed *g*-values ($g_1$–$g_3$), and the one-electron spin–orbit coupling constant ($\lambda_{Fe}$) [5, 212, 213].

$$\frac{V}{\lambda_{Fe}} = \frac{g_x}{g_x + g_y} + \frac{g_y}{g_z - g_x} \quad \textbf{(3-5)}$$

$$\frac{\Delta}{\lambda_{Fe}} = \frac{g_x}{g_z + g_y} + \frac{g_z}{g_y - g_x} - \frac{V}{2\lambda_{Fe}} \quad \textbf{(3-6)}$$

For low-spin ferric complexes, $\lambda_{Fe}$ is typically ~400 $cm^{-1}$ [5, 213, 214]. An additional term (*k*), the "orbital reduction factor", can be determined from the observed *g*-values to account for covalency. For low-spin heme centers, the value of *k* is typically <1.0. However, in instances in which $k \geq 1$, for example, some non-heme iron centers, the assumption that the excited $e_g$orbitals do not interact with the ground $t_{2g}$ set is not fully justified [5, 214].

On the basis of the *g*-values obtained from **S2**, a tetragonal splitting ($\Delta/\lambda = 6.53$) is obtained for the ternary complex in the absence of the C93–Y157 pair. Alternatively, in samples prepared from α-CDO (**S1**), a decrease in the tetragonal splitting ($\Delta/\lambda = 5.65$) is observed. However, both**S1** and **S2** exhibit very similar rhombic distortion (*V*/Δ values of 0.98 and 0.93, respectively). These findings indicate that the C93–Y157 pair decreases the magnitude of the low-spin ferric iron tetragonal field (Δ) without significantly altering the rhombicitiy (*V*/Δ) of the CN/Cys-bound $Fe^{III}$ site. As expected, the tetragonal splitting and rhombic distortion for the C93A CN/Cys-bound $Fe^{III}$–CDO complex are comparable to the values obtained for **S2** (for C93A, $\Delta/\lambda = 6.14$ and $V/\Delta = 0.98$). This observation suggests that the decreased tetragonal distortion in the presence of the C93–Y157 pair can mainly be attributed to a decrease in the level of cyano–ligand π-backbonding.

Alternatively, in samples of the $Fe^{III}$–CDO species bound by L-selenocysteine (L-Sec), the presence of the C93–Y157 pair has an only modest impact on the tetragonal

splitting (Δ/λ) of the ternary complex (5.89 and 5.56 for α- and β-CDO, respectively). However, a more significant difference can be observed in the rhombic distortion [$V/\Delta$ = 0.87 (α) and 1.00 (β)]. These observations suggest that for the L-Sec-bound ternary complexes, the presence of the C93–Y157 pair alters both cyano backbonding and substrate coordination geometry. For comparison, the observed $g$, Δ/λ, and $V/\Delta$ values for selected low-spin non-heme iron centers are listed in Table 3-3.

Table 3-3 EPR and Calculated Ligand Field Parameters Observed for Low-Spin Non-Heme Ferric Iron Centers.

| protein | $g1$ | $g2$ | $g3$ | Δ/λ | $V/\Delta$ | $k$ | ref |
|---|---|---|---|---|---|---|---|
| $Fe^{III}$(CN/Cys) (α-CDO) | 1.94 | 2.23 | 2.38 | 5.65 | 0.98 | 1.15 | this work |
| $Fe^{III}$(CN/Cys) (β-CDO) | 1.95 | 2.21 | 2.34 | 6.53 | 0.93 | 1.17 | this work |
| $Fe^{III}$(CN/Sec) (α-CDO) | 1.96 | 2.26 | 2.45 | 5.89 | 0.87 | 1.26 | this work |
| $Fe^{III}$(CN/Sec) (β-CDO) | 1.94 | 2.24 | 2.38 | 5.56 | 1 | 1.2 | this work |
| $Fe^{III}$(CN/Cys) C93A | 1.94 | 2.22 | 2.35 | 6.14 | 0.98 | 1.19 | this work |
| $Fe^{III}$(CN)–SOR | 1.97 | 2.13 | 2.27 | 10.8 | 0.7 | 1 | 68 |
| $Fe^{III}$–NH | 1.92 | 2.18 | 2.45 | 7.55 | 0.61 | 1.14 | 69 |
| $Fe^{III}$(CN)–AK | 1.89 | 2.21 | 2.43 | 5.72 | 0.8 | 1.11 | 77 |
| $Fe^{III}$(CN)2–PCD | 1.9 | 2.18 | 2.41 | 6.65 | 0.71 | 1 | 78 |
| $Fe^{III}$–BLM | 1.94 | 2.17 | 2.26 | 6.64 | 1.09 | 0.92 | 79 |
| activated BLM | 1.94 | 2.23 | 2.38 | 5.65 | 0.98 | 0.82 | 79 |

The alignment of the g-tensor trace ($g1$–$g3$) relative to the molecular axes can be qualitatively interrogated to develop greater insight into the role of these second-sphere interactions within the enzymatic active site. As illustrated in Figure 3-8, samples of the CN/Cys-bound $Fe^{III}$-α-CDO complex were prepared utilizing L-Cys (top) and D-Cys (middle). Not surprisingly, the g-values observed for each ternary complex are essentially identical as determined by quantitative simulation (listed in Table 3-2). This suggests that substitution of D-Cys for L-Cys does not significantly alter the electronic structure of the CN/Cys-bound $Fe^{III}$ site. However, the line width observed for samples prepared from D-Cys is significantly broader than those prepared from

L-Cys. As stated previously, the spectral line width for these signals is dominated by distributions in the observed g-values (g strain). As shown in Table 3-2, samples of the CN/Cys-bound $Fe^{III}$–CDO complex prepared from D-Cys exhibit significantly greater *g* strain ($\sigma g_1$ = 0.015, $\sigma g_2$ = 0.015, and $\sigma g_3$ = 0.023) than samples prepared from L-Cys ($\sigma g_1$ = 0.001, $\sigma g_2$ = 0.007, and $\sigma g_3$ = 0.010). Analogous to the Debye–Waller factors (B factors) reported via crystallography, the increased gstrain observed for binding of D-Cys to the FeIII site indicates greater coordination lability within the active site relative to that with L-Cys. Interestingly, this increase in *g* strain is significantly more pronounced (15-fold) along the g1 axis (1.93) than along the $g_2$ and $g_3$ axes (2.1- and 2.3-fold, respectively). By inspection of the enzyme–substrate complex (Figure 3-1), it is reasonable to conclude that altering the stereochemistry of the substrate Cys from l to d would disrupt any stabilizing interactions with the hydroxyl group of the C93–Y157 pair. As the Cys amine group is directly adjacent to the substrate carboxylate group, altering the substrate chiral center is expected to have the greatest influence on the stability of Fe–amine coordination. This observation implies that the $g_1$ axis of the CN/Cys-bound Fe site is closely associated with the Fe–N(Cys) bond.

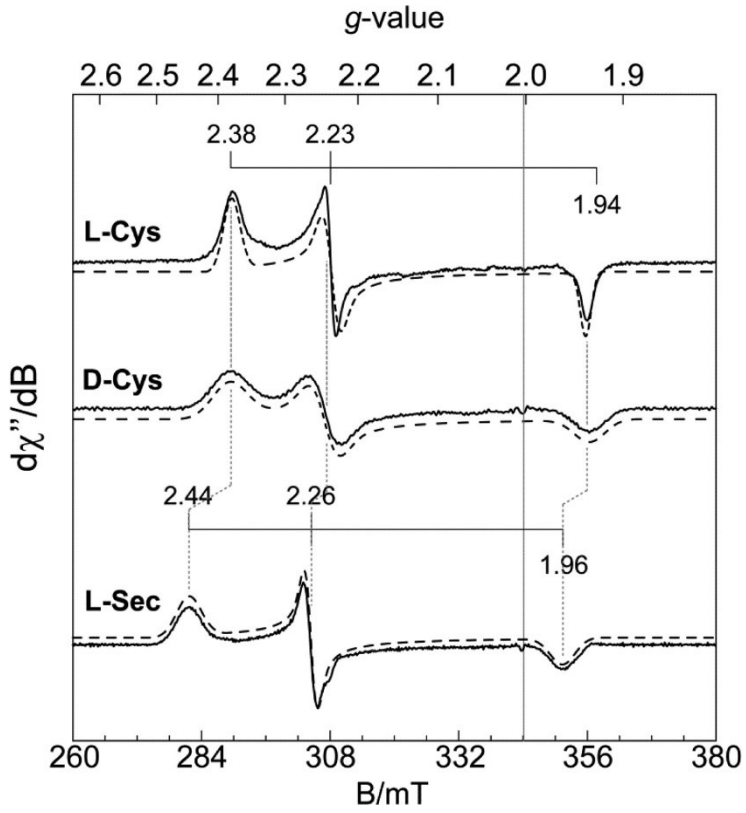


Figure 3-8 X-Band EPR spectra of l-Cys, d-Cys, and l-Sec CN/substrate-bound $Fe^{III}$–CDO complexes.
EPR spectroscopic simulations (−−−) are overlaid on the spectra (—) for comparison. Instrumental parameters: microwave frequency, 9.64 GHz; modulation frequency, 100 kHz; modulation amplitude, 0.9 mT; temperature, 10 K; microwave power, 6 μW (45 dB). Simulations parameters for $S = {}^1/_2$ species are listed in Table 3-3.

While CDO cannot utilize L-Sec as a substrate, for the purposes of providing an additional reference point in relating the observed *g*-values to a molecular coordinate system, it is instructive to prepare samples of CN/Sec-bound $Fe^{III}$–α-CDO for comparison. As indicated in Figure 3-8 (simulation parameters listed in Table 3-2), samples prepared by substituting L-Sec for L-Cys also exhibit a rhombic $S = {}^1/_2$ EPR spectrum. Not surprisingly, the *g*-values observed for L-Sec (2.44, 2.26, and 1.96) are shifted slightly

relative to those of L-Cys; however, this is most pronounced along the $g_3$ axis ($\Delta g \sim 0.08$) relative to the $g_2$ or $g_1$ axis ($\Delta g$ value of $\sim$0.03 or $\sim$0.02, respectively). This observation suggests that the $g_3$ axis is correlated to the Fe–$S_{(Cys)}$bond. Indeed, the increased polarizability of the sulfur atom within the Fe–$S_{(Cys)}$ bond should exhibit significantly greater spin–orbit coupling than other Fe-coordinating atoms. Therefore, it is expected that this bond also gives rise to the largest deviation between the observed *g* value and the electron *g* factor ($g_e \sim 2.0023$). Finally as the $g_1$, $g_2$, and $g_3$ axes must be mutually orthogonal, if $g_1$ and $g_3$ are assigned correctly, it is reasonable to conclude that the $g_2$ axis roughly corresponds to the Fe–CN bond. It should be noted that, although the proposed *g* axis assignments are consistent with spectroscopic observables provided above, this simplistic interpretation implies that the **g**-tensor is essentially colinear with the pseudo-octrahedral symmetry of the CN/Cys-bound $Fe^{III}$ site ligand coordination. However, additional DFT calculations (discussed below) are necessary to analytically verify the orientation of the **g**-tensor with respect to the $Fe^{III}$ site molecular axis system and provide additional insight into the effect of the C93–Y157 cross-link on the electronic structure of the ternary complex.

*QM/MM Computational Models of the CN/Cys-Bound $Fe^{III}$–CDO Active Site*

The EPR spectra of the two isoforms of CDO complexed with either L-Cys or L-Sec and cyanide were used to validate the QM/MM-optimized geometries of these species. Both the predicted and experimentally observed *g*-values for these species are listed in Table 3-4. Although our computational results only partially reproduce the large *g* spread observed experimentally, they properly predict a rhombic EPR spectrum with both functionals tested. This apparent discrepancy may be at least partially ascribed to the nature of the approximations inherent in the CP-SCF calculation used to calculate

EPR parameters, which has a known bias for underestimating *g* shifts for complexes containing a first-row transition metal [215]. Although the magnitude of error in our calculated versus experimentally observed *g*-values is larger than what has been previously seen with a set of small test molecules, an increase in the rhombicity for the α-CDO species as compared to that of the non-cross-linked version is both computationally predicted and experimentally observed. Additional validation of computational models may be derived by inspection of the calculated **g**-tensor orientation relative to the molecular coordinate system. Although the **g**-tensor axes obtained from calculations are not strictly colinear with the molecular axes, there is a close correspondence between the two coordinate systems. As indicated by Figure 3-9, for both isoforms of CDO (α- and β-CDO), DFT calculations predict that the $g_1$, $g_2$, and$g_3$ axes are approximately aligned along the Fe–$N_{(Cys)}$, Fe–$C_{(CN)}$, and Fe–$S_{(Cys)}$ bond axes, respectively. Thus, the computationally derived orientation of the **g**-tensor agrees well with the qualitatively inferred **g** orientation obtained by comparison of the L-Cys, D-Cys, and L-Sec CN/substrate-bound $Fe^{III}$–CDO EPR signals shown in Figure 3-8. As the QM/MM-derived models for the CN/Cys-bound $Fe^{III}$–CDO complex accurately reflect the change in the observed *g*anisotropy upon formation of the C93–Y157 cross-link and predict the orientation of the **g**-tensor, the molecular orbital descriptions and geometric parameters derived from these models clearly warrant further inspection.

Table 3-4 Experimentally Determined and Computationally Predicted g-values for the Species Discussed in This Work.

| | non-cross-linked (β) | | | cross-linked (α) | | |
|---|---|---|---|---|---|---|
| species | *g*1 | *g*2 | *g*3 | *g*1 | *g*2 | *g*3 |
| $Fe^{III}$(CN/Cys), observed | 1.951 | 2.207 | 2.344 | 1.937 | 2.235 | 2.379 |
| $Fe^{III}$(CN/Cys), PBE0 | 2.016 | 2.155 | 2.165 | 2.011 | 2.167 | 2.183 |
| $Fe^{III}$(CN/Cys), B3LYP | 2.025 | 2.135 | 2.146 | 2.024 | 2.145 | 2.163 |
| $Fe^{III}$(CN/Sec), observed | 1.947 | 2.236 | 2.377 | 1.936 | 2.254 | 2.445 |
| $Fe^{III}$(CN/Sec), PBE0 | 2.059 | 2.174 | 2.182 | 2.042 | 2.178 | 2.198 |
| $Fe^{III}$(CN/Sec), B3LYP | 2.085 | 2.161 | 2.181 | 2.088 | 2.157 | 2.183 |

The CN/Cys adducts of both FeIII-bound α- and β-CDO possess a very similar set of molecular orbitals (MOs) and thus also have the same low-spin Fe(III) ground state as shown in Figure 3-10. The MOs arising from an Fe–S(Cys) bonding interaction as well as the lone pair on the cysteinyl sulfur are also shown, whereas the Fe–CN and C–N bonding interactions are sufficiently stabilized in energy such that they have been omitted from this figure for the sake of clarity. As expected for a low-spin $d^5$ ion with approximately octahedral symmetry, the Fe $3d_{xz}$- and $3d_{yz}$-based MOs are doubly occupied, while the $3d_{xy}$-based MO is formally occupied by a single spin up electron. Consequently, it is the electron in this orbital that gives rise to the experimentally observed $S$ = 1/2 EPR spectrum. Although it is unoccupied, the spin down Fe $3d_{xy}$-based orbital (the SUMO) provides an excellent representation of the EPR-active orbital, as the composition of the SOMO becomes highly mixed because of spin polarization-induced orbital mixing of the SOMO with the other spin up orbitals [216]. For both the α- and β-CDO adducts, the SUMO contains a significant π* interaction between the Fe $3d_{xy}$ orbital (~65% of the electron density for this MO) and the sulfur $3p_y$ orbital (~15%) but lacks any sizable contributions from the cyano ligand (<5%). Although the formally singly occupied molecular orbital has little electron density on the cyano group, it is important to note that spin–orbit coupling-induced orbital mixing provides a route by which the nature of the Fe–

CN bond can be probed. The orbitals comprising the eg set in the parent octahedral symmetry (i.e., the Fe $3d_{x^2-y^2}$ and $3d_{z^2}$ orbitals) are unoccupied and have an energy much higher than that of the $t_{2g}$ set of Fe-based orbitals.

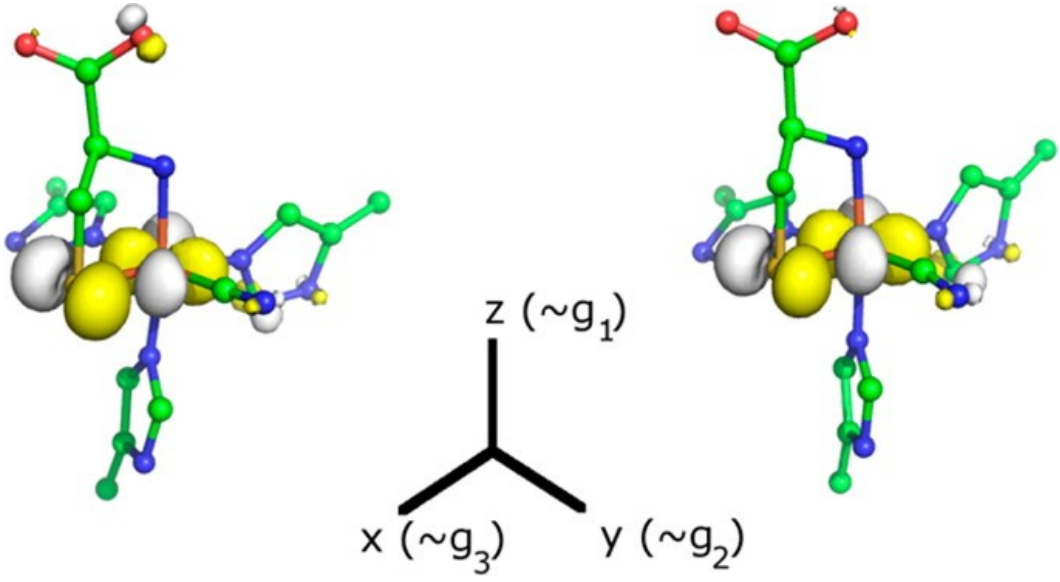


Figure 3-9 Comparison of the spin down SUMOs of the β (left) and α isoforms (right) of the CN/Cys-bound $Fe^{III}$–CDO adducts.
Comparison of the spin down SUMOs of the β (left) and α isoforms (right) of the CN/Cys-bound $Fe^{III}$–CDO adducts. The approximate orientation of the **g**-tensor, as derived from the computational models, with respect to the molecular axes is also shown.

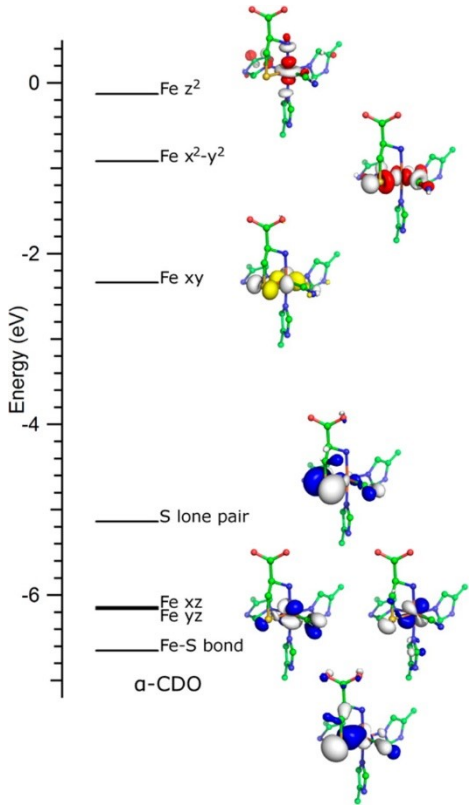


Figure 3-10 Partial molecular orbital diagram for the α isoform of the CN/Cys-bound $Fe^{III}$–CDO adduct.
For the sake of clarity, hydrogen atoms have been omitted and only the spin down orbitals are shown. Doubly occupied, singly occupied, and unoccupied MOs are colored blue, yellow, and red, respectively.

Judging by the QM/MM-optimized geometries of the α and β forms of CDO complexed with l-Cys and cyanide, the three-His facial triad motif is not perturbed upon formation of the C93–Y157 cross-link, with bond lengths and angles that are very similar between the two species (see Table 3-5). Similarly, the Fe–C and cyanide C–N bond distances are invariant between the two forms of CDO. However, as illustrated in Figure 3-11, the orientation of the cyanide ligand and the carboxylic acid group on the bound L-Cys are very sensitive to the second-sphere cross-link, with the Fe–C–N unit being considerably more linear when the cross-link is absent. This arrangement moves

the nitrogen of the cyano group near the Hδ atom of the highly conserved H155 residue, such that these atoms come to lie within the sum of their van der Waals radii. Additionally, a network of hydrogen bonds exists such that both the guanidyl group of R60 and the phenol of Y157 interact with one of the carboxylic acid oxygens on the bound L-Cys. Conversely, the formation of the covalent C93–Y157 bond moves the Y157 phenol group away from the side chain of R60, in turn pulling the carboxylic acid group of the substrate into a position that allows both of its oxygens to interact with an amide hydrogen on R60's guanidyl group (see Figure 3-11). Together, these computational results suggest that both the phenol group on Y157 and the guanidyl group of R60 play a major role in the recognition of the Cys substrate, while H155 may play a role in $O_2$ recognition.

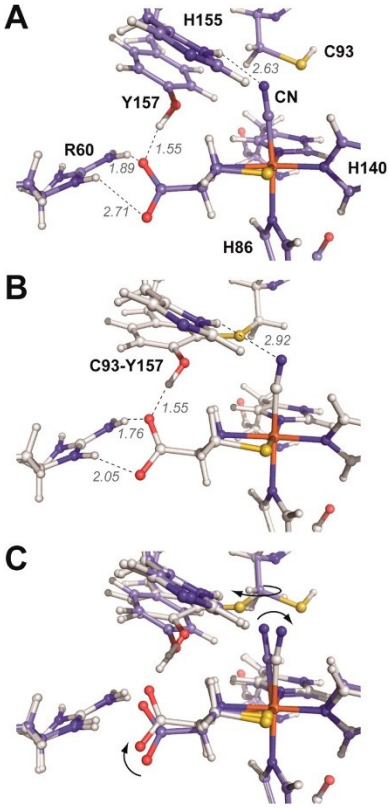


Figure 3-11 QM/MM-optimized structures of CN bound CDO. QM/MM-optimized structures of non-cross-linked (A) and cross-linked (B) CN/Cys-bound $Fe^{III}$–CDO adducts. An overlay of both structures is shown in panel C. Selected distances indicated by the dashed lines are given in angstroms. Arrows in panel C represent major structural changes within the CN/Cys-bound $Fe^{III}$–CDO site upon formation of the C93–Y157 cross-link.

Table 3-5 Relevant Bond Lengths (in angstroms) and Angles (in degrees) of the QM/MM-Optimized Active Sites.

| species | Fe–S(Cys)/Se(Sec) | Fe–N(Cys/Sec) | Fe–C(CN)–N(CN) | His86–Fe–C(CN) |
|---|---|---|---|---|
| $Fe^{III(}$CN/Cys)-α | 2.28 | 2.09 | 169.2 | 168.6 |
| $Fe^{III}$(CN/Cys)-β | 2.26 | 2.11 | 176.3 | 172.6 |
| $Fe^{III}$(CN/Sec)-α | 2.43 | 2.1 | 170.5 | 167.7 |
| $Fe^{III}$(CN/Sec)-β | 2.41 | 2.12 | 176.5 | 171.9 |

## Discussion

The ability of substrate-bound CDO to bind exogenous ligands in both the $Fe^{II}$ and $Fe^{III}$ oxidation states supports an inner-sphere model for $O_2$ activation. Historically, azido, carbonyl, and cyano ligands have been employed as a means of spectroscopically characterizing noncovalent interactions (distal effects) between the coordinated ligand and the solvent or protein environment in heme oxygenase enzymes [217]. However, while key second-sphere residues have been identified in non-heme mononuclear iron enzymes, fewer spectroscopic studies are available for comparison [200].

Consistent with previous reports, the vast difference observed between the rate of α-CDO product formation and those of AI-CDO and the C93A variant clearly demonstrates that formation of the C93–Y157 thioether cross-link is an important "activating" event in the maturation of CDO [99, 198]. In light of the EPR spectroscopy and QM/MM models that have been generated, the stark difference observed in the steady-state CSA/$O_2$ coupling efficiency among L-Cys (81%), D-Cys (4%), and CSH (6%) indicates that the C93–Y157 pair is critical for substrate recognition and stabilization of the ES complex and may also help gate access of solvent molecules to the active site following $O_2$ activation. As the C93A variant exhibits a coupling efficiency (45%) significantly higher than that of the wild-type enzyme utilizing D-Cys, it is clear that the hydroxyl group of Y157 represents a key enzyme–substrate interaction point. This is clearly evident upon comparison of the EPR spectra of L- and D-Cys CN/Cys-bound $Fe^{III}$–CDO sites. As both species exhibit equivalent *g*-values, the geometry of the first coordination sphere is essentially unperturbed. However, the increased *g* strain observed upon disrupting the interaction between C93–Y157 and the Cys carboxylate group indicates a significant increase in the lability of the enzyme–substrate complex. As

this effect is most pronounced along the Fe–$N_{(Cys)}$ bond ($g_1$axis), we can conclude that one function of the C93–Y157 pair is to position the substrate within the active site by securing the Fe–amine coordination. This may also explain the lack of enzymatic activity (and lack of cyanide binding) observed for the Y157F variant despite the ability of the enzyme to stabilize ferrous iron. The cross-link formed between C93 and Y157 also provides structural rigidity to the cross-linked pair, forcing a single conformation of the Y157 residue relative to the substrate-bound active site. The van der Waals radius of the C93–Y157 pair S atom may also add steric bulk to the $O_2$-binding pocket, thereby shielding the Fe active site from solvent access and resulting in the increased enzymatic coupling efficiency. This would also explain the apparent substrate inhibition behavior exhibited by the C93A variant and when utilizing D-Cys as the substrate in wild-type CDO assays. Moreover, the added bulk of the S atom also forces the Fe–C–N angle (169°) away from its nearly linear (176°) geometry observed in the absence of the C93–Y157 pair. This bend in the Fe–cyano coordination forces the cyano ligand 0.16 Å closer to the substrate thiol S atom. This effect would potentially be more pronounced for π-donating ligands ($O_2$ and NO), which favor a bent coordination geometry.

The use of cyanide as a spectroscopic probe over nitric oxide offers significant advantages with respect to *g* spread, sensitivity to Fe coordination angle, and the lack of "EPR active" contaminating species. Prior to the addition of cyanide, the substrate-bound AI-CDO and $Fe^{III}$–α-CDO ($Fe^{III}$–ES) cannot be distinguished by EPR spectroscopy. Therefore, no conclusions can be made regarding interactions between bound solvent molecules and the C93–Y157 pair. However, upon addition of cyanide to samples of AI $Fe^{III}$–ES, two $S = {}^1/_2$ signals (**S1** and **S2**) are observed. Alternatively, addition of cyanide to the substrate-bound $Fe^{III}$–α-CDO adduct yields only one signal (**S1**). As the Fe–C–N angle strongly influences the strength of π-backbonding, cyanide is an ideal probe for

monitoring perturbations to the coordination geometry. The decreased tetragonal ligand field strength (Δ/λ) observed for **S1** indicates weaker π-backbonding of the $Fe^{III}$-bound cyanide ligand than of the non-cross-linked enzyme (**S2**). This correlates well with our QM/MM-optimized geometries, in which the C93–Y157 pair induces a more bent Fe–C–N geometry, resulting in a decreased level of orbital overlap between the Fe 3d- and cyanide π*-based orbitals. Assuming a reasonable estimate for $\lambda_{Fe}$ (~400 $cm^{-1}$) [5, 213, 214], the tetragonal field splitting of CDO in the presence of the C93–Y157 thioether cross-link (α-CDO) is ~2260 $cm^{-1}$. Alternatively, in the absence of the C93–Y157 pair (**S2**; β-CDO), the axial field strength increases to ~2610 $cm^{-1}$ (Δ ~ 2500 $cm^{-1}$ for the C93A variant). Thus, the deviation in axial field strength (350 $cm^{-1}$) between α- and β-CDO corresponds to ~4.2 kJ/mol, approximately equivalent to the strength of a weak hydrogen bond.

As the H155A and Y157F variants are completely unable to bind cyanide, the role of second-sphere interactions with the substrate-bound active site cannot be confirmed by EPR spectroscopy. However, the vastly decreased activity or complete inactivity of these CDO variants suggests that these residues represent another key second-sphere interaction relevant to catalysis. The QM/MM models provided here suggest that this residue could serve as a stabilizing hydrogen bonding interaction with bound Fe–oxo intermediates during native catalysis, similar to H200 of 2,3-dioxygenase [199]. However, further experiments are necessary to verify this hypothesis.

In summary, the results provided here suggest that the C93–Y157 post-translational modification is critical for efficient enzymatic coupling. Coupling assays with substrate analogues (D-Cys and CSH) suggest that the hydroxyl group of Y157 represents a key point enzyme–substrate interaction necessary for efficient oxidative coupling. Additionally, the computational models presented here provide a reasonable

explanation for the differences observed in both enzymatic activity and spectroscopic observables between the cross-linked and non-cross-linked enzyme. While both spectroscopic measurements and computational models were performed on the catalytically inactive CN/Cys-bound $Fe^{III}$–CDO state, the pronounced decrease in $k_{cat}$ and CSA/$O_2$ coupling efficiency observed by altering the interactions between the Y157 hydroxyl and R60 guanidyl groups with the substrate Cys carboxyl group clearly demonstrates the relevance of these interactions in native catalysis. The obligate ordered addition of substrate prior to cyanide observed in samples of the $Fe^{III}$–CDO adduct is consistent with experiments utilizing nitric oxide as a spectroscopic probe for $O_2$ binding [104]. However, to the best of our knowledge, this has not previously been observed for other non-heme iron oxidase or oxygenase enzymes in experiments utilizing cyanide. This result is particularly intriguing in light of the prevailing theories proposed to explain the substrate-gated $O_2$ regulation exhibited by non-heme mononuclear iron enzymes: (1) thermodynamic gating of the $Fe^{II}/Fe^{III}$ redox couple upon substrate binding and (2) Fe site conformational changes that facilitate direct $O_2$ coordination [4-6]. Compared to that of nitric oxide, the binding of cyanide should be less influenced by the reduction potential of the active site, suggesting that thermodynamic gating cannot be solely responsible for regulating $O_2$ activation in CDO.

Abbreviations

| | |
|---|---|
| CDO | cysteine dioxygenase |
| CSH | 2-aminoethanethiol (cysteamine) |
| CSA | cysteinesulfinic acid |

| | |
|---|---|
| Sec | selenocysteine |
| HPLC | high-performance liquid chromatography |
| Ni-IMAC | immobilized metal (Ni) affinity chromatography |
| EPR | electron paramagnetic resonance |
| ROS | reactive oxygen species |
| DFT | density functional theory |
| QM/MM | quantum mechanics/molecular mechanics |
| MO | molecular orbital. |

Chapter 4 CDO Substrate Specificity

## Introduction

Cysteine dioxygenase (CDO) is a mononuclear non-heme iron enzyme that catalyzed the first concerted step in the $O_2$-dependent oxidation of L-cysteine to produce cysteine sulfinic acid (CSA) (Scheme 4-1). This enzyme has been of considerable medial interest recently as imbalances in sulfur metabolites has been observed in patients suffering from neurological diseases such as Alzheimer's, Parkinson's, and motor neuron disease [17, 218, 219].

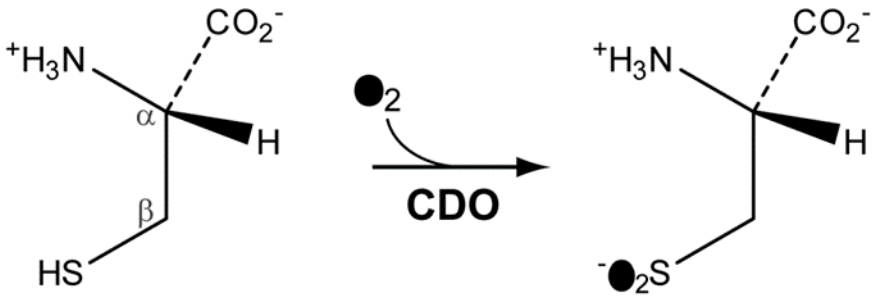


Scheme 4-1 Reaction catalyzed by CDO.

Multiple high resolution crystal structures of the resting and substrate-bound enzyme have been solved which highlight the atypical mononuclear non-heme iron active site for the mammalian CDO [17-19]. Unlike the majority of enzymes within this enzyme family, the mononuclear Fe-site within CDO (Figure 4-1) is coordinated by 3 protein derived histidine residues comprising the unusual 3-His facial triad motif. Another unusual feature of the eukaryotic CDO active site is a covalent post-translational modification in which spatially adjacent Cys93 and Tyr157 residues are covalently cross-linked to produce a C93-Y157 pair in the mature enzyme [108, 220]. While Y157 is conserved among all known CDO enzymes, the C93-Y157 covalent modification appears

to be unique to eukaryotic CDO enzymes. Several reports have demonstrated that formation of this cross-link increases the catalytic activity and coupling efficiency of CDO. However, since C93-varients unable to produce the C93-Y157 pair are active, this post-translational modification does not appear to be required for catalysis. To date, the exact mechanism of C93-Y157 formation remains unresolved.

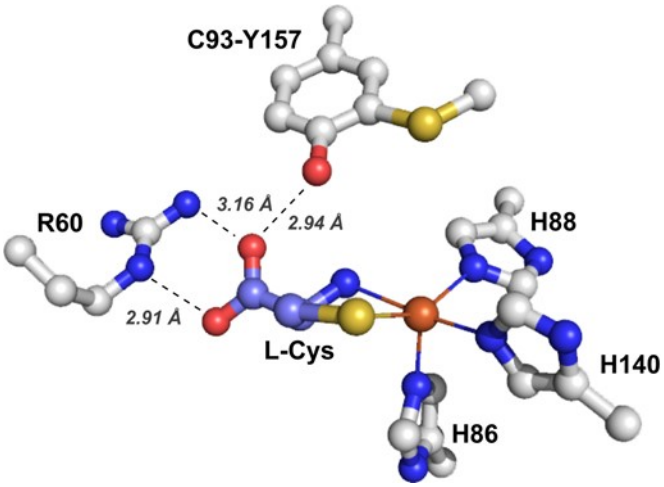


Figure 4-1 Active site of CDO.
1.60 Å resolution X-ray crystal structure for the substrate-bound CDO active site at pH 8.0 (pdb code 4IEV).

As shown in Figure 1, the L-Cys substrate coordination to the Fe-center bidentate via neutral amine and thiolate groups. As with other members of the non-heme mononuclear iron enzyme family, it has been reported that CDO exhibits an obligate ordered binding of L-Cys substrate prior to molecular oxygen [108, 221].

To date, several thiol dioxygenase (TDO) enzymes have been identified across phylogenic domains. All members of this enzyme class belong to the cupin superfamily which has a characteristic β-barrel tertiary structure. Interestingly, despite deviations in thiol-substrates, primary amino acid sequence comparison identifies serial conserved features among TDO enzymes. Figure 3 illustrates the sequence alignment among

selected TDO enzymes. For clarity, *Mus musculus* CDO amino acid numbering was used as the basis for all sequence alignments. From this analysis, the 3-His active site motif appears to be a common feature among all TDO enzymes. Indeed, as indicted by the boxed His residues in Figure 3, a $G(X)_5HXH(X)_{3,4}E(X)_6G$ and $G(X)_5PXG(X)_2H(X)_3N$ metal binding sequence can be identified among all TDO enzymes. Among the CDO enzymes, several conserved sequences have been identified across all phyla (Y58, R60, S153, H155, and Y157). For example, Y157 and H155 is conserved across eukaryotic and prokaryotic CDO enzymes. Moreover, Y157F and H155A CDO variants exhibit abolished enzymatic activity [98]. Recent spectroscopic experiments on the catalytically inactive ferric enzyme suggest that these residues are involved in key outer-sphere interactions with the substrate-bound active site to facilitate catalysis. Alternatively, the C93 involved in C93-Y157 cross-link formation is only observed in mammalian CDO enzymes. In bacterial enzymes this residue is replaced by a glycine residue suggesting that this residue is not catalytically essential. In support of this hypothesis, C93A and C93S variants of mammalian CDO retain catalytic activity, albeit with decreased $k_{cat}$. [98, 220]. X-ray crystallography and computational models suggest that R60 is involved in charge stabilizing of the L-Cys carboxylate group. Interestingly, this Arg residue is absent in mammalian and bacterial ADO enzymes which catalyze the $O_2$-dependent oxidation of 2-aminoethanethiol (cysteamine). It has also been suggested that Ser153, His155 and Tyr157 comprise a "*catalytic triad*". By analogy to hydrolases and transferase enzymes, the Tyr-hydroxyl group of the C93-Y157 pair may serve as a general acid/base in catalysis [7, 186]. In apparent support of this, mutagenesis of H155 and Y157 residues abolishes enzymatic activity [221]. However, to date S153 variants have not been evaluated for diminished activity. Moreover, experiments to evaluate a general acid/base role for C93-Y157 pair have not been specifically explored.

Two other Fe/$O_2$-dependent TDO enzymes [mercaptosuccinate dioxygenase, (MSDO) and 3-mercaptopropionate dioxygenase (MPDO)] have been recently identified in *Variovorax paradoxus*. Sequence comparison to known thiol dioxygenase enzymes suggest that these enzymes also contain a 3-His active site motif [222, 223]. The conserved 3-His metal binding site observed among all TDO enzymes suggest that this first-coordination sphere is necessary for thiol oxidation whereas the outer-sphere residues are likely utilized to facilitate binding of their specific thiol-substrates. This implies that TDO enzymes hve the potential to catalyze the $O_2$-dependent oxidation of a variety of thiol-substrates to produce the corresponding sulfinic acid providing they are capable of binding to the mononuclear active site. In principle, this activity would be modulated by outer-sphere interactions stabilizing substrate binding within the active site cavity.

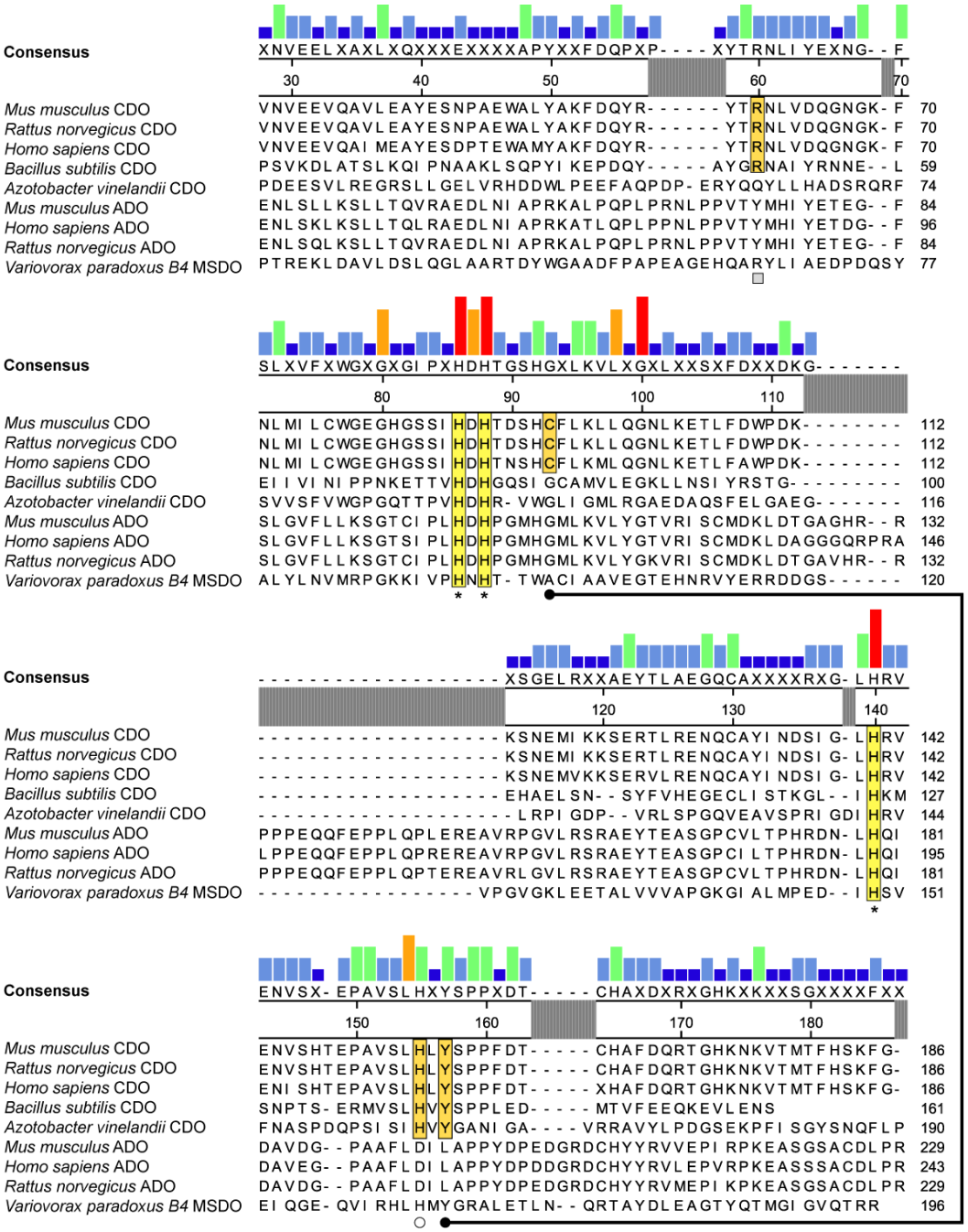


.Figure 4-2 Sequence alignment of thiol dioxygenases.
Conserved CDO active site (3 His) residues (*) are highlighted in yellow boxes and the C93-Y157 cross-link identified in mammalian CDO is illustrated by connected filled circles (●). Catalytically essential outer-sphere residues R60 and H155 identified by the open square (□) and open circle (○), respectively.

Previous studies suggest that mammalian CDO exhibits high substrate and stereoselectivity [95, 117, 118, 224]. For example, it has been reported that L-homocysteine is an inhibitor of CDO but its potential as a substrate has not been fully evaluated [225]. Indeed, detailed characterization of non-natural substrates for severely underreported for TDO enzymes. One potential complication in the characterization of thiol oxygease enzymes is that experimentally, the rate of oxygen consumption (rather than product formation) is frequently reported as enzymatic activity. Unfortunately, the efficiency by which TDO enzymes incorporate molecular oxygen into their product can frequently be less than unity. Therefore, steady-state characterization of TDO enzymes should include both $O_2$-consumption and sulfinic acid product formation.

In this work, a variety of commercially available thiol-substrates were utilized to evaluate the substrate-specificity of wild-type CDO cloned from *Mus musculus*. The steady-state kinetic parameters and coupling efficiencies for $O_2$-consumption and sulfinic acid formation are reported. In all substrates evaluated, NMR spectroscopy, differential $^{16}O/^{18}O$-incorperation, and tandem LC-MS/MS were employed to confirm formation of the appropriate sulfinic acid product.

## Materials and Methods

*Enzyme Purification.*

Recombinant mouse cysteine dioxygenase (CDO) was expressed in Escherichia coli BL21(DE3) pLysS competent cells (Novagen) and purified using a 10 L bioreactor (New Brunswick Scientific Bioflo100) as previously described [108]. The as-isolated CDO enzyme typically contains ~50% (±10%) of the C93-Y157 cross-link as observed by SDS PAGE. Therefore, prior to use, purified CDO is converted to the fully modified enzyme described elsewhere [220]. All preparations were assayed for ferrous and ferric iron content spectrophotometrically as previsouls described [104, 153]. Typical ferrous

iron incorporation within purified CDO is ~ 70% (±10%). For clarity, the concentrations reported in enzymatic assays reflect the concentration of ferrous iron within samples of CDO ($Fe^{II}$-CDO).

*NMR Kinetic Study.*

NMR kinetic studies were performed on a JEOL nuclear magnetic resonance spectrometer (300 MHz, Pleasanton, CA). All measurements were made in Wilmad NMR tubes (Wilmad NMR tubes 5 mm diameter, precision). For each reaction, fully modified CDO was added to a buffered substrate solution in D2O (sodium phosphate buffer, pD 7.5) to initiate the reaction at ambient temperature (20 ± 2°C). Reaction points were terminated by heat shock at 94°C for 2 minutes followed by spin-filtration to remove denatured protein. Final concentration of 1 mM trimethylsilyl propanoic acid (TMSP) was added as the internal standard. NMR spectra were integrated using JOEL USA Delta NMR data processing software (version 5.0.4). For all solutions prepared in deuterium, the corrected value of pD was obtained by adding 0.4 pD units the value reported by the pH electrode (Mettler Toledo InLab Expert Pro)[226].

*Circular Dichroism (CD).*

CD analysis of CDO in $H_2O$ and $D_2O$ buffer was performed on JASCO 715 UV-visible circular dichroism spectrometer with xenon arc light source. All protein samples analyzed by CD were prepared in 10 mM phosphate buffer (pL 7.5) filtered through a 0.22 μm polypropylene membrane filter (VWR international). Equine heart myoglobin (100684-32-0), chicken egg white lysozyme (12650-88-3), and poly-L-lysine (25988-63-0) purchased from Sigma-Aldrich were used as standards for secondary structure determination as described elsewhere [227]. CD results were also interpreted using the freely available online software K2D3 (http://k2d3.ogic.ca/). Far-UV (185-260 nm) CD

spectra of protein were recorded in a quartz cuvette of 0.1 cm path length and ~0.45 mL volume at a scan speed of 40 nm/min at ambient temperature.

*Oxygen Electrode*.

The rate of dissolved oxygen concentration utilized in CDO reactions was determined using a standard Clark type electrode (Hansatech Instruments, Norfolk, England). Reaction temperatures were maintained at room temperature (20 °C) using a circulating water bath (ThermoFlex 900, Thermo Scientific). Calibration of the $O_2$-electrode was performed as previously described [220]. For each potential CDO substrate utilized, 1.0 mL of a stock substrate solution was prepared in prepared in a buffered solution (25 mM HEPES pH 7.5 or equivalent phosphate buffer), and incubated at 20 °C for 3-5 minutes to equilibrate the reaction solution to the cell temperature and establish a baseline for O2-electrode. Reactions were initiated by addition of CDO to obtain a final enzyme concentration within the cell of 1M.

*$^{18}O_2$ Enzymatic Reactions.*

Solutions of CDO and potential substrates were rigorously degassed on a Schlenk line prior to transferring into the anaerobic chamber. Analytical grade argon was passed through a copper catalyst (Kontes, Vineland, N.J.) to remove residual $^{16}O_2$ impurities and then sparged through distilled water to hydrate the gas. All anaerobic samples were prepared in a glove box (Coy Laboratory Products Inc., Grass City, MI) with the $O_2$ concentration maintained below 1 ppm. $^{18}O_2$ reactions were prepared within the anaerobic chamber by adding excess substrate (25 mM) to a 15 mL tube (VWR Catalog Number 89049-170) containing 5.0 μM CDO. Each vial was sealed using a rubber septum (ChemGlass P/N CG-3022-93) within the glove box and secured by standard electrical tape. $^{18}O_2$-saturated buffer (99%) was prepared by sparging anaerobic buffer with $^{18}O_2$ gas (Icon 99% $^{18}O_2$, P/N 11135). For all substrates, 500 uL of

the $^{18}O_2$-satuated buffer was spiked into the septum sealed reaction vial by gas-tight Hamilton syringe (X mL model number ) resulting in an approximate final $O_2$ concentration of ~ 226 uM. [Footnote: based on the $O_2$ solubility in $H_2O$ at 20 °C, 1.36 mM] [ref. Lang's Handbook of Chemistry]. Reaction mixtures were mixed by gentle inversion and allowed to react for > 1 hour prior to heat denatureation, spin-filtration, and work up for LC-MS analysis.

*HPLC Analysis.*

CDO catalyzed oxidation of L/D-Cysteine and 2-Aminoethanethiol (Cysteamine) was performed by isocratic reverse phase HPLC as previously described [108, 220]. Instrumentation: Shimadzu LCMS-2020; Column, Phenomenex Kinetex C18, 100 Å column 100 x 4.6 mm, 2.6 m; Mobile phase, 20 mM sodium acetate, 0.6% methanol, 1% heptofluorobutyric acid, pH 2.0; Injection volume, 50 µL; Flow rate, 1.0 mL/min. Product CSA and hypotaurine peaks were detected spectrophotometrically at 218 nm. Each reaction was initiated by addition of enzyme (1 uM) to a buffered solution (25 mM Phosphate, 50 mM NaCl, pD 7.5) containing substrate at ambient temperature (20 ± 2 °C). At selected times, aliquots were collected and quenched by addition of 10 µL of 40 mM hydrochloric acid. Following addition of HCl, samples were heated to X °C for 3 minutes to ensure full enzyme denaturation and then spin-filtered by 0.22 µM cellulose acetate membrane (Corning, Spin-X) prior to analysis on HPLC. The concentration of CSA and hypotaurine produced in reactions were determined by comparison to standard calibration curves (0.1-20 mM).

*LC-MS Analysis.*

Detection and verification of enzymatic products were performed on a triple quadrupole LC-MS/MS (Shimadzu Scientific Instruments, LC-MS 8040) in positive mode. Instrumentation: Column, Phenomenex Luna 3 µm HILIC 200Å, 100×2.00 mm, (P/N

00D-4449-B0); Mobile phase, 70% ACN, 30% $H_2O$, 30 mM $NH_4AC$, 0.1% trifluroacetic acid; Injection volume, 2 μL; Flow rate, 0.25 mL/min. Confirmation of CDO product (CSA and hypotaurine) in assays utilizing L/D-Cysteine and Cysteamine was performed by multiple reaction monitoring (MRM) using a triple quadrupole LC-MS/MS [Shimadzu Scientific Instruments, LCMS 8040].[228] The molecular ions ($M^+$) of the CDO products (CSA, 154 m/z and Hypotaurine, 110 m/z) were selected for secondary fragmentation. MRM optimization was then employed to maximize transition intensity and sensitivity for each fragment. The optimized MRM method was used to verify both substrate and product by direct injection of enzymatic assays. These results were compared to direct injection of synthetic standards.

In the absence of commercially available standards for thiol dioxygenase products, confirmation of the predicted substrate sulfinic acids product was determined by select ion mode (SIM) by comparing the mass of the molecular ion ($M^+$) produced upon exchanging $^{16}O_2$ molecular oxygen for $^{18}O_2$.

## Results

*Validation of CDO Steady-state Kinetics Utilizing Native (L-Cys) Substrate by NMR, $O_2$-electrode, and LC-MS.*

The rate of CDO catalyzed L-Cysteine oxidation to produce CSA has been well characterized by utilizing both HPLC and LC-MS [229]. While significantly less sensitive than these HPLC or LC-MS methods, NMR does offer a greater flexibility in monitoring a potentially broad range of sulfinic acids produced by CDO. Moreover, re-optimization of assay conditions for each individual substrate or developing a general method for the analysis of all potential products is time consuming and impractical. As an initial point of comparison, the NMR spectra for L-Cysteine and CSA standards within a sodium

phosphate buffer in $D_2O$ (pD 7.5) are shown in Figure 4-3. Within this spectral window (2.50 - 4.40 ppm), only the non-exchangeable protons on the α- and β-carbon are observed. Both have several unique sets of peaks which can be utilized to monitor either the formation of CSA or loss of L-Cys over the course of a typical reaction. The NMR spectra of L-Cys exhibits 3 sets of resonances observed as a doublet of doublets (*dd*) centered at 3.02 [1H(β), $J_1$ = 4.2 Hz, $J_2$ = 15 Hz], 3.10 [1H(β), $J_1$ = 5.7 Hz, $J_2$ = 15 Hz], and 3.97 ppm [1H(α), $J_1$ = 4.2 Hz, $J_2$ = 5.7 Hz]. By comparison, the same α/β-protons observed for CSA are observed at 2.70 [1H(β), *J* = 14.0 Hz, *J* = 9.9 Hz], 2.84 [1H(β), *J* = 14.0 Hz, *J* = 3.0 Hz], and 4.16 ppm [1H(α), *J* = 9.9 Hz, *J* = 3.0 Hz]. As expected, the diastereotopic protons on the β-carbon exhibit the most pronounced shift in their resonance position due to the close proximity of the adjacent sulfinic acid group. For simplicity, the α-proton for L-Cys and CSA (3.97 and 4.16 ppm, respectively) were utilized to monitor the rate of CDO catalyzed CSA formation.

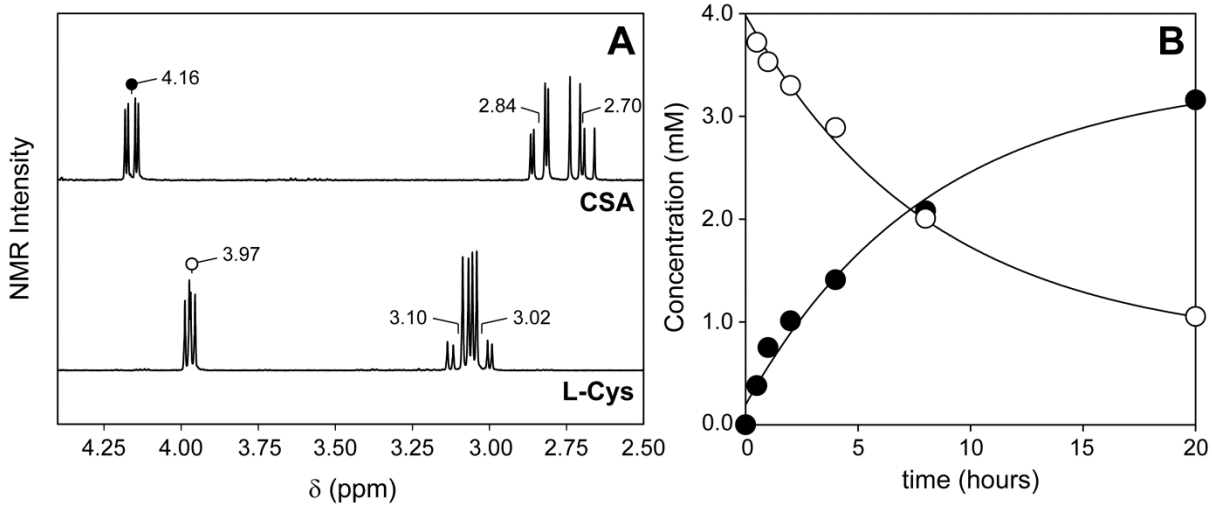


Figure 4-3 NMR spectrum of L-cysteine and cysteine sulfinic acid and time course of CSA formation and L-Cys decay.
Time course of CSA formation and L-Cys decay were followed by integration of the α-carbon protons (L-Cys, *white circle*; centered at 3.97 ppm [1H, dd, $J_1$

= 4.2 Hz, $J_2$ = 5.7 Hz]; CSA, black circle, dd centered at 4.16 ppm [1H, dd, $J_1$ = 9.9 Hz, $J_2$ = 3.0 Hz]) **B**. Time course of L-Cys decay and CSA formation with time. Each data set was fit to either a single exponential decay (L-Cys) or rise to maximum (CSA) using the same observed rate constant of $k_{obs}$ ~ 0.12 ± 0.03 amplitude, 4.0 ± 0.15 mM (~84% of expected).

As proof of concept, 2 μM CDO was added to a phosphate buffered D2O solution (25 mM Phosphate, 50 mM NaCl, pD 7.5, 20 °C) containing 4.5 mM L-Cys. At selected time points, samples were quenched, spin-filtered, and analyzed by NMR spectroscopy. Trimethylsilyl propanoic acid (TMSP) was added as an internal standard to each sample for normalization of signal intensity as described in Material and Methods. Quantitation of each species was performed by comparison of the integrated peak area to freshly prepared standards of known concentration. As illustrated in Figure 4-3 B, integration of the L-Cys and CSA (α-proton) was used to track both the formation and decay of CSA and L-Cys, respectively for 20 hours. Each data set was fit to either a single exponential decay (L-Cys) or a single exponential rise to maximum (CSA) using the same observed rate constant (kobs ~ 0.12 ± 0.03 hours). The amplitude of the exponential phase was 4.0 ± 0.15 mM, representing ~88% of theoretical (4.5 mM). Thus over the course of 20 hours, the reaction reached near completion and the rate of CSA formation was kinetically matched to L-Cys decay.

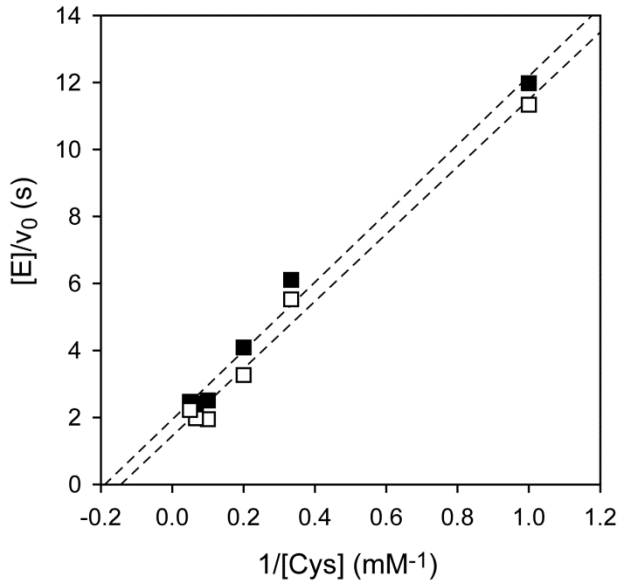


Figure 4-4 Michaelis-Menten kinetics of CDO determined by NMR and HPLC. Comparative Lineweaver-Burk analysis for CDO catalyzed steady-state CSA formation determined by NMR (□) and HPLC (■). Assay conditions: 25 mM sodium phosphate, 50 mM NaCl, pD 7.5, 20 ± 2 °C.

Steady state kinetics for CDO catalyzed CSA formation was performed as described while varying the concentration of L-Cys from 1- 20 mM, then performed under these same conditions. Rather than the extended time (20 hours) illustrated above, the initial rate ($v_0$) of each reaction was collected over 45-minutes as a function of L-Cys concentration. All initial rates are normalized for Fe-containing enzyme concentration ($v_0$/[E]), such that the values for $k_{cat}$ and $K_M$ are easily obtained from fitting the results to the Michaelis-Menten equation. Under these conditions (25 mM sodium phosphate, 50 mM NaCl, pD 7.5, 20°C) the steady-state kinetics for wild-type CDO with L-Cys obtained by NMR spectroscopy is shown in Figure 4-4 . The line represents a best-fit to the initial rate of CSA formation (●). From this analysis, the values of $k_{cat}$ and $K_M$ were determined to be 0.6 (± 0.1) $s^{-1}$ and 6.90 (± 0.5) mM for the steady-state rate of CSA formation, respectively. For comparison, the steady kinetics for CSA formation obtained by HPLC in

$H_2O$ (25 mM sodium phosphate, 50 mM NaCl, pH 7.5, 20°C) utilizing HPLC is overlaid on the same plot (△). Here, the Michaelis-Menten parameters, $k_{cat}$ and $K_M$, were determined to be 1.3 (± 0.2) $s^{-1}$ and 2.3 (± 0.3) mM, respectively. The apparent discrepancy in the observed Michelis-Menten parameters are largely attributed to solvent ($D_2O/H_2O$) effects influencing both $k_{cat}$ and $K_M$, which will be discussed in a separate paper.

The efficiency at which an oxygenase enzyme incorporates one mol of $O_2$ into the product is referred to as 'coupling'. Under steady-state conditions, the (CSA/O2)-coupling efficiency is defined as the ratio of the kcat determined for CSA formation divided by the kcat obtained for the rate of O2-consumption. Interestingly, D2O has a significant impact on the (CSA/O2) coupling efficiency for CDO. The coupling efficiency of fully-modified CDO catalyzed L-Cys oxidation was previously reported as 75-80% [220]. However, under identical conditions within a deuterium buffer, the observed (CSA/O2)-coupling (pD = 7.5) is significantly lower (33%). Indeed, as illustrated in Figure 4-4, the observed $k_{cat}$, $K_M$, and coupling efficiency all appear to be negatively influenced by substituting D2O for H2O. While beyond the scope of this report, a full description of CDO solvent kinetic isotope effects (SKIEs), proton inventory, and (H2O/D2O)-effects on (CSA/O2)-coupling are discussed in the following paper.

As an additional control, CD spectroscopy was used to verify that addition of deuterium had no significant impact on the secondary structure of CDO. In these experiments, 5 μM samples of CDO were prepared in 25 mM Phosphate, 50 mM NaCl, pL 7.5, 20 °C. Analysis of the CDO secondary structure was made by comparison to known protein standards (myoglobin, poly-L-lysine, and lysozyme) utilizing the freely available software K2D3 as described in *Materials and Methods*. From this analysis, it was observed that the fraction of α-helical and β-sheet secondary structure in buffer

prepared in $H_2O$ is 13 ± 4 % and 35 ± 3%, respectively. These values correlate well with the percent $\alpha$-helical (17%) $\beta$-sheet (34%) content determined by X-ray crystallography [230]. By comparison, no significant change is observed in the fraction of $\alpha$-helix (15%) or $\beta$-sheet (33%) observed for CDO in deuterium buffer. Thus, the perturbations observed in the steady-state kinetic parameters cannot be attributed to a change in the secondary structure of CDO.

LC-MS and tandem LC-MS/MS was used to verify the identity of the sulfinic acid product produced in CDO catalyzed reactions and confirm dioxygenase activity. Multiple reaction monitoring (MRM) was performed to verify as described in *Materials and Methods* by multiple reaction monitoring (MRM). In these experiments, the $[M+H]^+$ molecular ion for CSA (154 m/z) was selected for fragmentation. MRM optimization was then employed to maximize transition intensity and sensitivity for each fragment allowing for quantitation of product ions. The optimized MRM method was used to verify sulfinic acid product by direct injection of enzymatic assays. These results were compared to direct injection of synthetic standards. As observed in Figure 4-6 (*panel A*), in addition to the parent $[M+H]^+$ ion observed at 154 m/z, the MRM spectra for a standard solution of CSA exhibits two characteristic ions at 44 and 74 m/z. Figure 4-6 B demonstrates that direct injection (2 $\mu$L) of the CDO catalyzed reaction with L-Cys yields and identical fragmentation pattern. The matching fragmentation pattern and relative intensities confirm the native CSA product within CDO reactions.

As final confirmation of dioxgenase activity, selected ion mode (SIM) was used to observe an appropriate shift in the observed product $[M+H]^+$ ion upon substitution of $^{18}O_2$ for the naturally abundant $^{18}O_2$. As illustrated in Figure 4-6 C, CDO reactions performed

in the presence of $^{18}O_2$ results in a + 4 m/z shift (154 m/z versus 158 m/z) in the observed $[M+H]^+$ parent ion, thus verifying the inclusion of both oxygen atoms into the substrate.

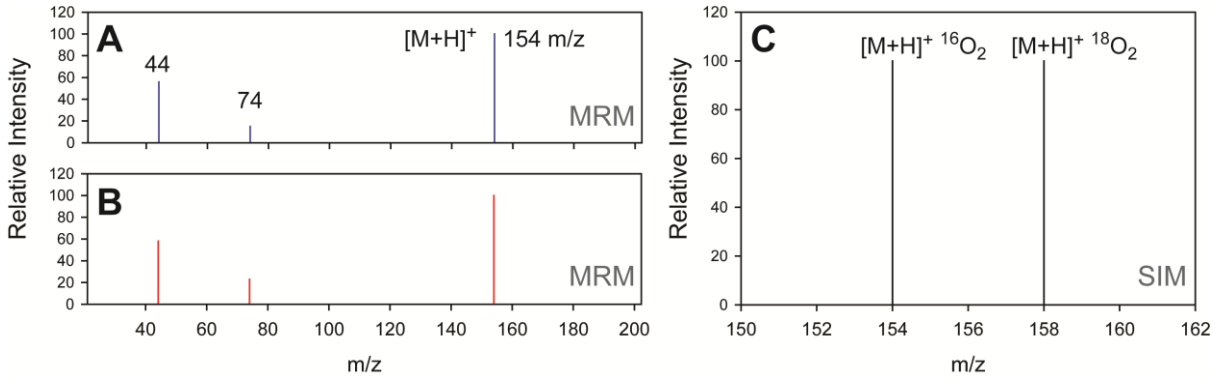


Figure 4-5 LC-MS study on CDO's natural substrate L-cysteine using MRM (Multiple reaction)

*Determination of Steady-state CDO Kinetics and Coupling Utilizing Non-native Substrates.*

CDO steady-state kinetics analysis utilizing non-native (Cysteamine) substrate by NMR, O2-electrode, and LC-MS.

As discussed above, although not perfect, NMR method works fairly well comparing to HPLC method when the natural substrate L-Cysteine is utilized. To explore whether this method also works on the non-natural substrate, Cysteamine was investigated with Hypotaurine being the product of dioxygenase activity. As an initial point of comparison, the NMR spectra for Cysteamine and Hypotaurine standards within a sodium phosphate buffer in $D_2O$ (pD 7.5) are shown in Figure 4-7. Within this spectral window (2.50 - 4.00 ppm), only the non-exchangeable protons on the $\alpha$- and $\beta$-carbon are observed. Both have several unique sets of peaks and the formation of Hypotaurine or loss of Cysteamine can be monitored over the course of a typical reaction. The NMR spectra of Cysteamine exhibits 2 sets of resonances observed as triplets (*t*) centered at

2.83 [2H(β), *J* = 6.6 Hz] and 3.19 ppm [2H(α), *J* = 6.6 Hz]. By comparison, the same α/β-protons observed for Hypotaurine are observed at 2.65 [2H(β), *J* = 6.6 Hz] and 3.62 ppm [2H(α), *J* = 6.6 Hz].

Since the peaks of β-protons overlap a little bit for both chemicals (3.19 and 3.62 ppm, respectively), the α-protons for Cysteamine and Hypotaurine (2.83 and 2.65f ppm, respectively) were utilized to monitor the rate of CDO catalyzed Hypotaurine formation.

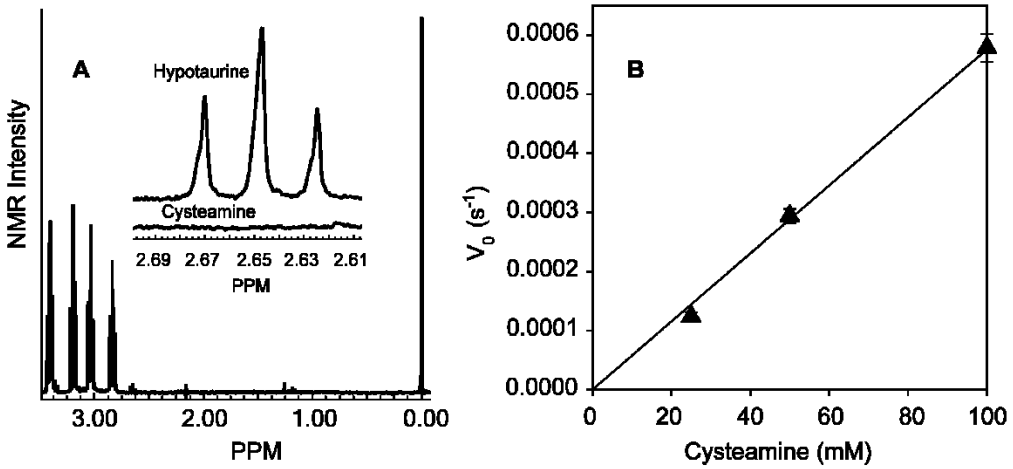


Figure 4-6 Full NMR spectrum of cysteamine reaction converted by CDO and $v_0$ vs. cysteamine concentration.

As proof of concept, 70 μM CDO was added to a phosphate buffered D2O solution (25 mM Phosphate, 50 mM NaCl, pD 7.5, 20 °C) containing 90 mM Cysteamine. Samples were quenched, spin-filtered, and analyzed by NMR spectroscopy after incubated for 6 hours. Trimethylsilyl propanoic acid (TMSP) was added as an internal standard for normalization of signal intensity as described in Material and Methods. Quantitation of each species was performed by comparison of the integrated peak area to freshly prepared standards of known concentration. As illustrated in Figure 4-7A, peaks that arose form Hypotaurine was observed, which indicated that CDO indeed

converted Cysteamine to Hypotaurine and NMR method could be utilized to study this reaction.

Steady state kinetics for CDO catalyzed Hypotaurine formation was performed as described while varying the concentration of Cysteamine (25 mM, 50 mM, 100 mM, respectively), then performed under these same conditions. All initial rates are normalized for Fe-containing enzyme concentration (v0/[E]). Because of the low activity, large concentration of CDO was used to carry out the reaction (More than 20 M). Under these conditions (25 mM sodium phosphate, 50 mM NaCl, pD 7.5, 20°C) the kinetics for wild-type CDO with Cysteamine obtained by NMR spectroscopy is shown in Figure 4-8 (panel B). The line represents a best-fit to the initial rate of Hypotaurine formation (▲). The $K_M$ value was huge and the saturation of Cysteamine was never reached. To analyze the reaction kinetics, data set was fit to a linear equation, and the slope of the line represents the pseudo v/K value for CDO catalyzing Cysteamine. From this analysis, the values of the pseudo v/K was determined to be 5.8(± 0.3) $e^{-3}$ $M^{-1}s^{-1}$.

LC-MS and tandem LC-MS/MS was also used to verify the identity of the hypotaurine product produced in CDO catalyzed reactions and confirm dioxygenase activity. Like in the L-cysteine study, multiple reaction monitoring (MRM) and select ion mode (SIM) were both performed. In these experiments, the $[M+H]^+$ molecular ion for Hypotaurine (110 m/z) was selected for fragmentation. MRM method was optimized and used to verify Hypotaruine product by direct injection of enzymatic assays and the results were compared to direct injection of synthetic standards. As observed in Figure 4-8 (*panel **A***), in addition to the parent $[M+H]^+$ ion observed at 110 m/z, the MRM spectra for a standard solution of Hypotaurine exhibits three characteristic ions at 30, 45 and 65 m/z. Figure 4-8 B demonstrates that direct injection (2 μL) of the CDO catalyzed reaction with

Cysteamine yields and identical fragmentation pattern, which confirms the Hypotaurine product within CDO reactions.

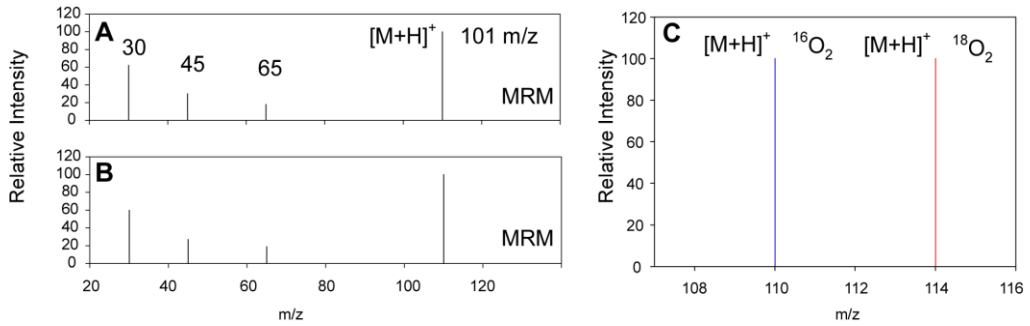


Figure 4-7 LC-MS study on cysteamine using MRM (Multiple reaction).

Selected ion mode (SIM) was used to observe an appropriate shift in the observed product $[M+H]^+$ ion upon substitution of $^{18}O_2$ for the naturally abundant $^{16}O_2$ to confirm the dioxygenase activity. As illustrated in Figure 4-8C, CDO reactions performed in the presence of $^{18}O_2$ results in a + 4 m/z shift (114 m/z versus 110 m/z) in the observed $[M+H]^+$ parent ion, thus verifying the inclusion of both oxygen atoms into the substrate.

Studies with the natural substrate L-Cysteine and non-natural substrate Cysteamine prove that this NMR method is valid and can be used to determine the kinetic parameters for CDO reactions. Besides Cysteamine, other potential non-natural substrates for CDO were investigated. Due to the high hydrophilicity of the substrates and their corresponding products, it's difficult to come up with a method that applies to all of them. Instead of inventing new method for each of the substrate, a universal method that works for all of them would be desired. This NMR method fulfill this purpose well. It is suitable to monitor all of the reactions with almost no change in the procedures. Although the synthetic standards for the other non-natural substrate such as L-Penicillamine and L-homocysteine are not available, it is easy to monitor the decrease of the substrate peak and increase of the new peaks that are associated with products.

With the NMR procedure described above, other non-natural substrates were analyzed and the kinetic parameters are summarized in Table 4-1 below. In the LC-MS experiment, the lack of synthetic standards makes the MRM method not applicable. However, the $^{18}O_2$ substitution experiment using the SIM method is able to prove the presence of product and dioxygenase activity for CDO. The LC-MS results is summarized in Table 4-2.

Table 4-1 Kinetic Parameters determined by NMR.

| | *Oxygen Consumption* | | | *Product Formation* | | | |
|---|---|---|---|---|---|---|---|
| Substrate | $k_{cat}$ ($s^{-1}$) | $K_M$ (mM) | $V/K$ ($M^{-1}s^{-1}$) | $k_{cat}$ ( $s^{-1}$) | $K_M$ (mM) | $V/K$ ($M^{-1}s^{-1}$) | Coupling (%) |
| L-CYS | 1.80 ± 0.02 | 0.70 ± 0.15 | 2570 | 0.71 ± 0.1 | 7.2 ± 0.3 | 98 | 33% |
| D-CYS | 2.40 ± 0.04 | 3.1 ± 0.21 | 770 | 0.08 ± 0.1 | 6.8 ± 3.2 | 10 | 3.30% |
| L-PA | 1.04 ± 0.37 | 34.6 ± 8.0 | 30 | 0.07 ± 0.01 | 6.2 ± 2.1 | 11 | 6.70% |
| L-HYC | 1.60 ± 0.08 | 13.4 ± 1.8 | 119 | 0.09 ± 0.01 | 13.4 ± 3.7 | 7 | 5.60% |
| CSH | N/A | N/A | 0.63 | N/A | N/A | >0.01 | 0.90% |
| MS | - | N/A | N/A | - | N/A | N/A | N/A |
| CME | + | N/A | N/A | + | N/A | N/A | N/A |
| SC | - | N/A | N/A | - | N/A | N/A | N/A |
| DMC | - | N/A | N/A | - | N/A | N/A | N/A |

CYS, cysteine; HCY, homocysteine; CSH, 2-aminoethanethiol (Cysteamine); MS, mercaptosuccinate; PA, L-penicillamine, CME, L-cysteine methyl ester; DMC, 2-(Dimethylamino)ethanethiol. SC, S-methyl-L-cysteine.

Table 4-2 Summary of $^{18}O_2$ substitution experiment.

| Substrate | $^{16}O$ product | $^{18}O$ product |
|---|---|---|
| L-cysteine | + | + |
| D-cysteine | + | + |
| Cysteamine | + | + |
| L-homocysteine | + | + |
| L-Penicillamine | + | + |

## Discussion

While a variety of highly sensitive methods have been described in the literature for the detection of cysteine sulfinic acid [108, 231-234], NMR spectroscopy offers the most versatile means to study a variety of substrates surrogates under identical conditions. Furthermore, the high $K_M$ value observed for CDO catalyzed reactions in $D_2O$ (6.9 mM) allows for collection of data at substrate concentrations appropiate for steady-state kinetic studies. One caveats of using NMR spectroscopy is the significant decrease in the ($O_2$/CSA)-coupling in $D_2O$ as opposed to $H_2O$. While beyond the scope of this manuscript, this effect is believed to originate from a proton-sensitive intermediate in the CDO catalytic cycle following binding of $O_2$.

Although steady-state studies for CDO were first reported nearly 45 years ago, to date no detailed characterization of the substrate-specificity or oxidative coupling efficiencies have been reported for this enzyme. Indeed, despite significant overlap in conserved TDO residues surrounding the non-heme mononuclear active site, few studies are available regarding the minimal structural components of the substrate required for CDO catalyzed thiol oxidation.

As with most oxidase and oxygenase enzymes, activation of $O_2$ in TDO enzymes is gated by substrate-binding. This behavior facilitates high catalytic efficiency and prevents enzymatic self-oxidation or production of potentially toxic reactive oxygen

species (ROS). Currently two theories have been proposed to explain the substrate-gated $O_2$ regulation exhibited by non-heme mononuclear iron enzymes; (**1**) thermodynamic gating of the $Fe^{II}/Fe^{III}$ redox couple and (**2**) Fe-site conformational changes which facilitate direct $O_2$-coordination [235-237]. Taking the structure of the substrate-bound active site into consideration (**Figure 1**), the data provided in **Table 1** demonstrates that simultaneous coordination of both the substrate-thiol and amine groups is required for gating $O_2$-binding and subsequent substrate oxidation. For example, **1MP** and **3MP** lack an amino group and thus neither $O_2$-consumption or sulfinic acid product formation is observed upon addition to aerobic solutions of CDO. Furthermore, while **DMC** has an available amino functional group, the increased steric bulk and altered pKa of the alkylated amine relative to the primary Cys-amine clearly inhibits direct Fe-coordination. Similarly, the methylated thiol group of **SC** prevents S-atom coordination to the Fe-site. Qualitatively, these findings support the hypothesis that (S/N)-bidentate coordination of the CDO substrates thermodynamically regulate $O_2$-binding by altering the $Fe^{II/III}$ redox couple.

One feature that is becoming increasing clear is the role of the C93-Y157 pair in providing appropriate substrate orientation and stereoselectivity. In principle, the (S/N)-bidentate substrate coordination provides two points of simultaneous interaction. A third point of interaction is produced by hydrogen bonding between the Cys-carboxylate group and the C93-Y157 pair (2.94 Å). This third interaction is further stabilized electrostatically by interaction with R60 (separated by 2.91 - 3.16 Å). Collective, these interactions satisfy the "*three point interaction rule*" for chiral selection [238]. Assuming bidentate coordination of the substrate is the only requirement for gating reactivity with $O_2$, then addition of either D- or L-isomers should trigger consumption of $O_2$, which is indeed what is observed experimentally. However, the ratio of $O_2$-consumed per CSA generated in

reactions involving D-Cys is vastly attenuated (< 3%) as compared to the physiologically relevant L-Cys substrate (33%). Indeed, nearly a 10-fold increase is observed in specificity (*V*/*K*) of CDO for L-Cys as compared to D-Cys. This suggests that in addition to the chiral selection provided by three simultaneous points of interaction, outer-sphere interactions with C93-Y157/R60 may also be involved in restricting substrate geometry within the active site in order to minimize escape of partially reduced reactive oxygen species. This hypothesis is supported by previous EPR studies using cyanide as a spectroscopic probe for substrate-interactions within the catalytically inert $Fe^{III}$-CDO. In these experiments, both D- and L-Cys were capable of binding the catalytically to facilitate cyanide binding, however samples prepared form D-Cys exhibited significantly greater *g*-strain suggesting greater conformational heterogeneity [220]. Reactions with CSH further support this model in that both $O_2$-consumption and hypotaurine formation is significantly inhibited. This suggests that in the absence of the third point of interaction, substrate binding is weak resulting in decreased $O_2$-consumption rates and even further attenuated coupling efficiencies.

By comparison, both **HYC** and **PA** have the capacity to form the appropriate three point interaction with CDO. As a consequence the rate of $O_2$-consumption observed for these substrates ($1.04 < k_{cat} < 1.60$ $s^{-1}$) is quite similar to both L/D-Cys. However, as expected the increased steric bulk of these substrates are likely to distort coordination geometry away from optimal resulting in decreased productive catalysis (8% and 15% relative to L-Cys). In fact, within experimental error, all three substrates (**D-Cys**, **HYC**, and **PA**) exhibit essentially equivalent specificity ($5 < V/K < 10$ $M^{-1}$ $s^{-1}$).

As illustrated in **Figure 2**, sequence comparison of mammalian ADO enzymes suggest the absence of a Cys-Tyr pair at an equivalent position as CDO within the protein sequence. However, SDS PAGE gels of recombinant ADO exhibit a doublet

protein band similar to what has been observed for as-isolated CDO [93]. This observation suggests that ADO may also contain a post-transnationally modified Cys-Tyr pair. Interestingly, threading of the *Rattus norvegicus* ADO primary amino acid sequence through the *Rattus norvegicus* CDO (4IEV) crystal structure using the freely available software Protein Homology/analogY Recognition Engine V 2.0 (Phyre$^2$) [239] places Y208 and C206 in close proximity to the predicted 3-His (H100, H102, and H179) active site facial triad. Given the absence of a substrate-carboxylate group for ADO, the presence of a Cys-Tyr cross-link analogous to CDO implies that this post-translational modification must have additional functionality beyond comprising a three point interaction. One possible hypothesis is that the Cys-Tyr pair serves as a proton acceptor for the substrate-amine group during coordination of substrate to the Fe-site. In principle Cys-Tyr cross-linking would be expected to decrease the pKa of the Tyr-hydroxyl group to closer match that of the substrate free amine group [240]. To date, no experiments have been performed to evaluate the possibility of the C93-Y157 serving as a general base in catalysis.

# Appendix A

NMR spectra of CDO substrates and product standards

abundance
0
0.1
0.2
0.3
0.4
0.5
1.38
3.00
4.0 3.9 3.8 3.7 3.6 3.5 3.4 3.3 3.2 3.1 3.0 2.9 2.8 2.7 2.6 2.5 2.4 2.3 2.2 2.1 2.0 1.9 1.8 1.7 1.6 1.5 1.4 1.3 1.2 1.1 1.0 0.9 0.8 0.7 0.6 0.5 0.4 0.3 0.2 0.1 0-0.1
3.987
3.973
3.969
3.955
3.136
3.117
3.086
3.067
3.055
3.041
3.006
2.992
X : parts per Million : 1H
H3N+
COO−
HS

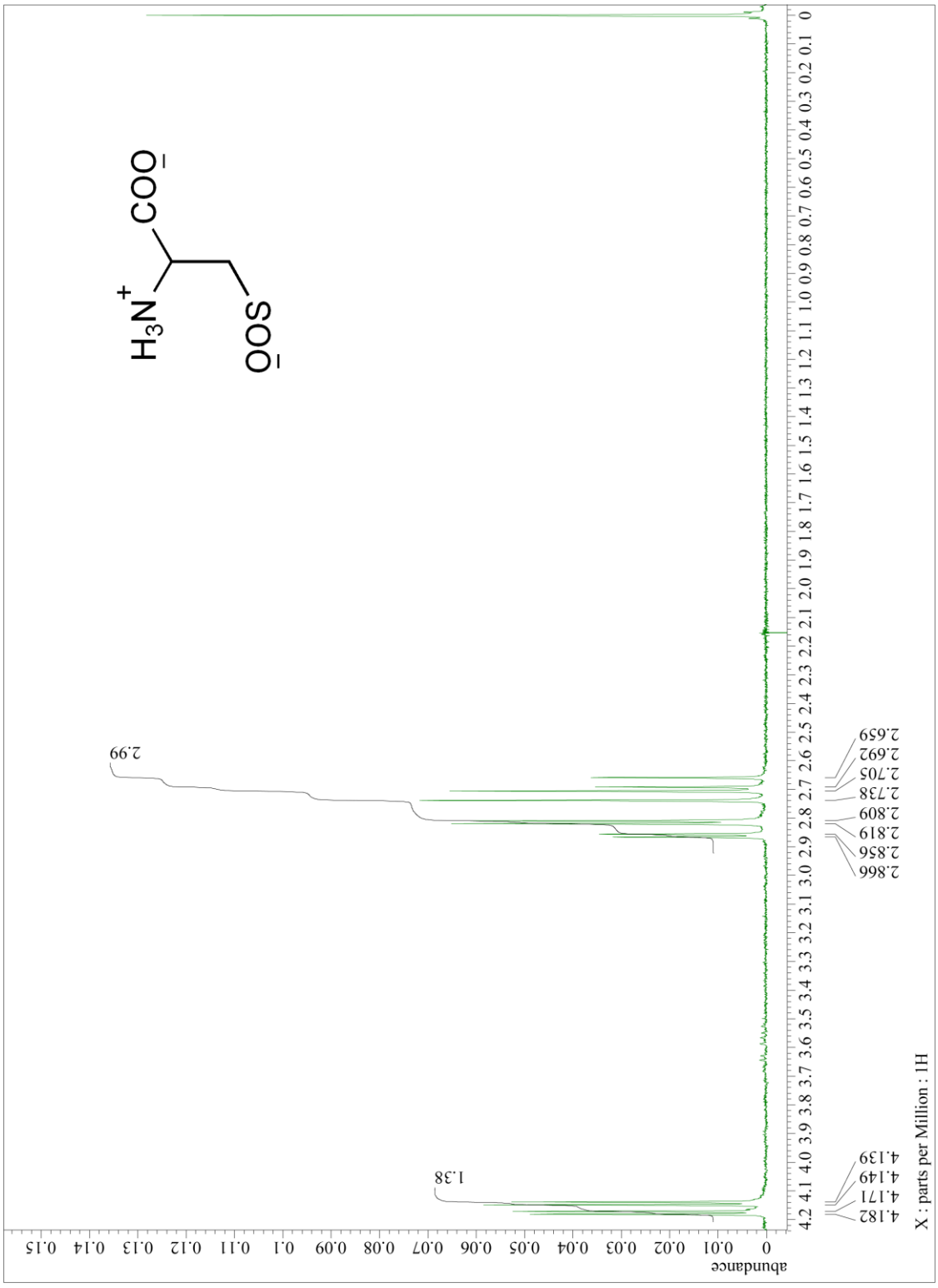
abundance
X : parts per Million : 1H
4.182
4.171
4.149
4.139
2.866
2.856
2.819
2.809
2.738
2.705
2.692
2.659
2.99
1.38
$H_3N^+$
$COO^-$
$OOS^-$

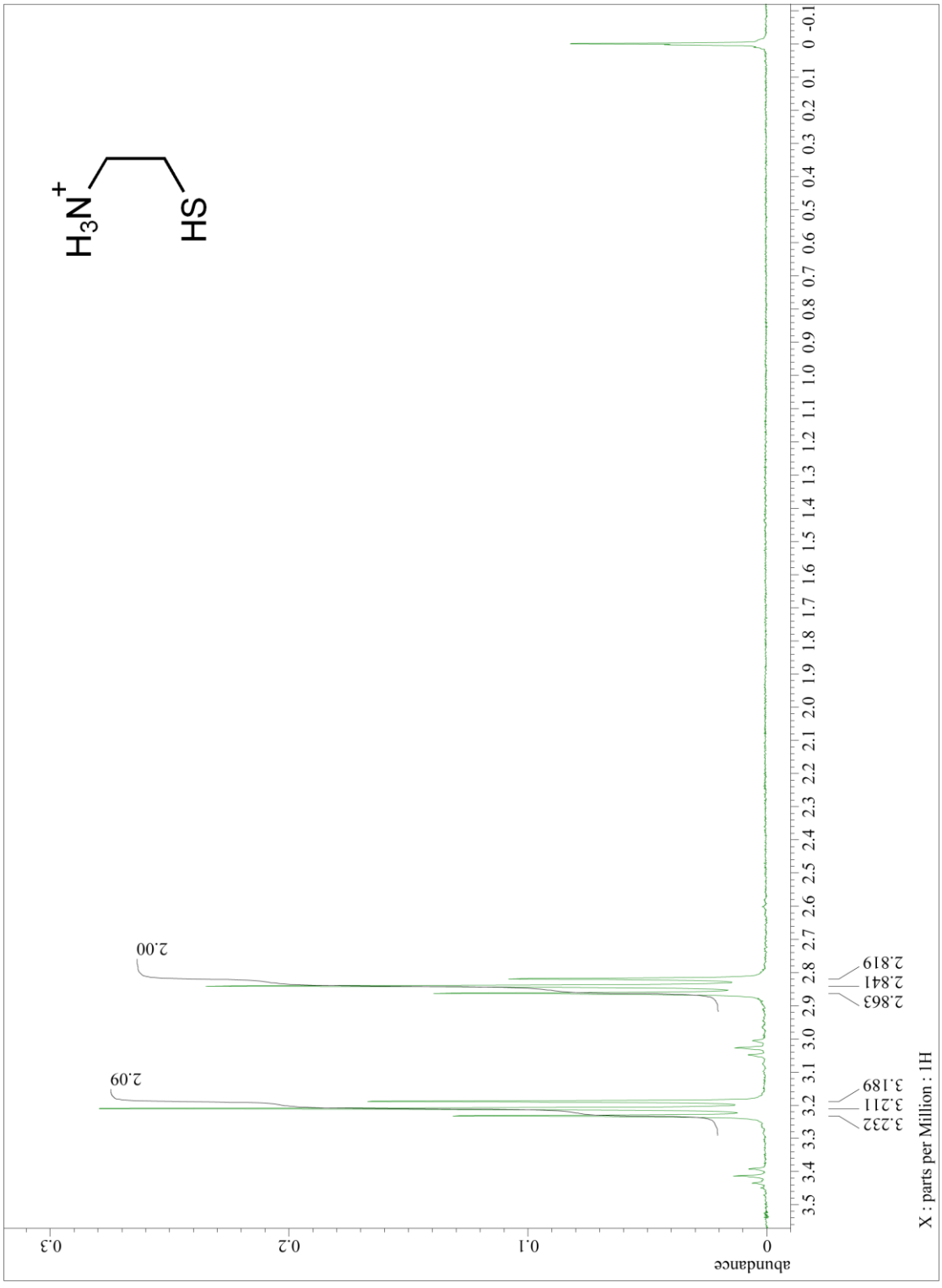
abundance
0.3
0.2
0.1
0
2.09
2.00
3.232
3.211
3.189
2.863
2.841
2.819
X : parts per Million : 1H
HS
H3N+

abundance
0 0.01 0.02 0.03 0.04 0.05 0.06 0.07 0.08 0.09 0.1 0.11 0.12 0.13 0.14 0.15 0.16 0.17 0.18
2.09
2.00
3.5 3.4 3.3 3.2 3.1 3.0 2.9 2.8 2.7 2.6 2.5 2.4 2.3 2.2 2.1 2.0 1.9 1.8 1.7 1.6 1.5 1.4 1.3 1.2 1.1 1.0 0.9 0.8 0.7 0.6 0.5 0.4 0.3 0.2 0.1 0 -0.1
3.385
3.362
3.339
2.670
2.647
2.625
X : parts per Million : 1H
H3N+
OOS

40.0
30.0
20.0
10.0
0
(thousandths)
0.86
3.01
3.00
H3N+
COO−
HS
4.1 4.0 3.9 3.8 3.7 3.6 3.5 3.4 3.3 3.2 3.1 3.0 2.9 2.8 2.7 2.6 2.5 2.4 2.3 2.2 2.1 2.0 1.9 1.8 1.7 1.6 1.5 1.4 1.3 1.2 1.1 1.0 0.9 0.8 0.7 0.6 0.5 0.4 0.3 0.2 0.1 0
4.017
3.702
3.663
1.579
1.554
1.469
1.449
1.183
1.104
X : parts per Million : 1H

## References


1. Bruijnincx, P.C., G. van Koten, and R.J. Klein Gebbink, *Mononuclear non-heme iron enzymes with the 2-His-1-carboxylate facial triad: recent developments in enzymology and modeling studies.* Chem Soc Rev, 2008. **37**(12): p. 2716-44.
2. McCoy, J.G., L.J. Bailey, E. Bitto, C.A. Bingman, D.J. Aceti, B.G. Fox, and G.N. Phillips, Jr., *Structure and mechanism of mouse cysteine dioxygenase.* Proc Natl Acad Sci U S A, 2006. **103**(9): p. 3084-9.
3. Koehntop, K.D., J.P. Emerson, and L. Que, Jr., *The 2-His-1-carboxylate facial triad: a versatile platform for dioxygen activation by mononuclear non-heme iron(II) enzymes.* J Biol Inorg Chem, 2005. **10**(2): p. 87-93.
4. Costas, M., M.P. Mehn, M.P. Jensen, and L. Que, Jr., *Dioxygen activation at mononuclear nonheme iron active sites: enzymes, models, and intermediates.* Chem Rev, 2004. **104**(2): p. 939-86.
5. Solomon, E.I., T.C. Brunold, M.I. Davis, J.N. Kemsley, S.K. Lee, N. Lehnert, F. Neese, A.J. Skulan, Y.S. Yang, and J. Zhou, *Geometric and electronic structure/function correlations in non-heme iron enzymes.* Chem Rev, 2000. **100**(1): p. 235-350.
6. Solomon, E.I., A. Decker, and N. Lehnert, *Non-heme iron enzymes: contrasts to heme catalysis.* Proc Natl Acad Sci U S A, 2003. **100**(7): p. 3589-94.
7. Simmons, C.R., Q. Liu, Q. Huang, Q. Hao, T.P. Begley, P.A. Karplus, and M.H. Stipanuk, *Crystal structure of mammalian cysteine dioxygenase. A novel mononuclear iron center for cysteine thiol oxidation.* J Biol Chem, 2006. **281**(27): p. 18723-33.
8. Guengerich, F.P., *Common and uncommon cytochrome P450 reactions related to metabolism and chemical toxicity.* Chem Res Toxicol, 2001. **14**(6): p. 611-50.

9. Meunier, B., S.P. de Visser, and S. Shaik, *Mechanism of oxidation reactions catalyzed by cytochrome p450 enzymes.* Chem Rev, 2004. **104**(9): p. 3947-80.

10. Munro, A.W., H.M. Girvan, and K.J. McLean, *Variations on a (t)heme--novel mechanisms, redox partners and catalytic functions in the cytochrome P450 superfamily.* Nat Prod Rep, 2007. **24**(3): p. 585-609.

11. Clifton, I.J., M.A. McDonough, D. Ehrismann, N.J. Kershaw, N. Granatino, and C.J. Schofield, *Structural studies on 2-oxoglutarate oxygenases and related double-stranded beta-helix fold proteins.* J Inorg Biochem, 2006. **100**(4): p. 644-69.

12. Abu-Omar, M.M., A. Loaiza, and N. Hontzeas, *Reaction mechanisms of mononuclear non-heme iron oxygenases.* Chem Rev, 2005. **105**(6): p. 2227-52.

13. Hegg, E.L. and L. Que, Jr., *The 2-His-1-carboxylate facial triad--an emerging structural motif in mononuclear non-heme iron(II) enzymes.* Eur J Biochem, 1997. **250**(3): p. 625-9.

14. Que, L., Jr., *One motif--many different reactions.* Nat Struct Biol, 2000. **7**(3): p. 182-4.

15. Blasiak, L.C. and C.L. Drennan, *Structural perspective on enzymatic halogenation.* Acc Chem Res, 2009. **42**(1): p. 147-55.

16. Vaillancourt, F.H., E. Yeh, D.A. Vosburg, S. Garneau-Tsodikova, and C.T. Walsh, *Nature's inventory of halogenation catalysts: oxidative strategies predominate.* Chem Rev, 2006. **106**(8): p. 3364-78.

17. Simmons, C.R., L.L. Hirschberger, M.S. Machi, and M.H. Stipanuk, *Expression, purification, and kinetic characterization of recombinant rat cysteine dioxygenase, a non-heme metalloenzyme necessary for regulation of cellular cysteine levels.* Protein Expr Purif, 2006. **47**(1): p. 74-81.

18. Chai, S.C., A.A. Jerkins, J.J. Banik, I. Shalev, J.L. Pinkham, P.C. Uden, and M.J. Maroney, *Heterologous expression, purification, and characterization of recombinant rat cysteine dioxygenase.* J Biol Chem, 2005. **280**(11): p. 9865-9.

19. Bagley, P.J., L.L. Hirschberger, and M.H. Stipanuk, *Evaluation and modification of an assay procedure for cysteine dioxygenase activity: high-performance liquid chromatography method for measurement of cysteine sulfinate and demonstration of physiological relevance of cysteine dioxygenase activity in cysteine catabolism.* Anal Biochem, 1995. **227**(1): p. 40-8.

20. Neidig, M.L. and E.I. Solomon, *Structure-function correlations in oxygen activating non-heme iron enzymes.* Chem Commun (Camb), 2005(47): p. 5843-63.

21. Price, J.C., E.W. Barr, L.M. Hoffart, C. Krebs, and J.M. Bollinger, Jr., *Kinetic dissection of the catalytic mechanism of taurine:alpha-ketoglutarate dioxygenase (TauD) from Escherichia coli.* Biochemistry, 2005. **44**(22): p. 8138-47.

22. Proshlyakov, D.A., T.F. Henshaw, G.R. Monterosso, M.J. Ryle, and R.P. Hausinger, *Direct detection of oxygen intermediates in the non-heme Fe enzyme taurine/alpha-ketoglutarate dioxygenase.* J Am Chem Soc, 2004. **126**(4): p. 1022-3.

23. Hoffart, L.M., E.W. Barr, R.B. Guyer, J.M. Bollinger, Jr., and C. Krebs, *Direct spectroscopic detection of a C-H-cleaving high-spin Fe(IV) complex in a prolyl-4-hydroxylase.* Proc Natl Acad Sci U S A, 2006. **103**(40): p. 14738-43.

24. Galonic, D.P., E.W. Barr, C.T. Walsh, J.M. Bollinger, Jr., and C. Krebs, *Two interconverting Fe(IV) intermediates in aliphatic chlorination by the halogenase CytC3.* Nat Chem Biol, 2007. **3**(2): p. 113-6.

25. Brown, C.D., M.L. Neidig, M.B. Neibergall, J.D. Lipscomb, and E.I. Solomon, *VTVH-MCD and DFT studies of thiolate bonding to [FeNO]7/[FeO2]8 complexes of isopenicillin N synthase: substrate determination of oxidase versus oxygenase activity in nonheme Fe enzymes.* J Am Chem Soc, 2007. **129**(23): p. 7427-38.

26. Bassan, A., M.R. Blomberg, and P.E. Siegbahn, *A theoretical study of the cis-dihydroxylation mechanism in naphthalene 1,2-dioxygenase.* J Biol Inorg Chem, 2004. **9**(4): p. 439-52.

27. Bollinger, J.M., J.C. Price, L.M. Hoffart, E.W. Barr, and C. Krebs, *Mechanism of taurine: alpha-ketoglutarate dioxygenase (TauD) from Escherichia coli.* Eur J Inorg Chem, 2005(21): p. 4245-4254.

28. Muthukumaran, R.B., P.K. Grzyska, R.P. Hausinger, and J. McCracken, *Probing the iron-substrate orientation for taurine/alpha-ketoglutarate dioxygenase using deuterium electron spin echo envelope modulation spectroscopy.* Biochemistry, 2007. **46**(20): p. 5951-9.

29. Price, J.C., E.W. Barr, B. Tirupati, J.M. Bollinger, Jr., and C. Krebs, *The first direct characterization of a high-valent iron intermediate in the reaction of an alpha-ketoglutarate-dependent dioxygenase: a high-spin FeIV complex in taurine/alpha-ketoglutarate dioxygenase (TauD) from Escherichia coli.* Biochemistry, 2003. **42**(24): p. 7497-508.

30. Riggs-Gelasco, P.J., J.C. Price, R.B. Guyer, J.H. Brehm, E.W. Barr, J.M. Bollinger, Jr., and C. Krebs, *EXAFS spectroscopic evidence for an Fe=O unit in the Fe(IV) intermediate observed during oxygen activation by taurine:alpha-ketoglutarate dioxygenase.* J Am Chem Soc, 2004. **126**(26): p. 8108-9.

31. Trewick, S.C., T.F. Henshaw, R.P. Hausinger, T. Lindahl, and B. Sedgwick, *Oxidative demethylation by Escherichia coli AlkB directly reverts DNA base damage.* Nature, 2002. **419**(6903): p. 174-8.

32. Falnes, P.O., R.F. Johansen, and E. Seeberg, *AlkB-mediated oxidative demethylation reverses DNA damage in Escherichia coli.* Nature, 2002. **419**(6903): p. 178-82.

33. Mishina, Y. and C. He, *Oxidative dealkylation DNA repair mediated by the mononuclear non-heme iron AlkB proteins.* J Inorg Biochem, 2006. **100**(4): p. 670-8.

34. Duncan, T., S.C. Trewick, P. Koivisto, P.A. Bates, T. Lindahl, and B. Sedgwick, *Reversal of DNA alkylation damage by two human dioxygenases.* Proc Natl Acad Sci U S A, 2002. **99**(26): p. 16660-5.

35. Yu, B., W.C. Edstrom, J. Benach, Y. Hamuro, P.C. Weber, B.R. Gibney, and J.F. Hunt, *Crystal structures of catalytic complexes of the oxidative DNA/RNA repair enzyme AlkB.* Nature, 2006. **439**(7078): p. 879-84.

36. Winter, A.D. and A.P. Page, *Prolyl 4-hydroxylase is an essential procollagen-modifying enzyme required for exoskeleton formation and the maintenance of body shape in the nematode Caenorhabditis elegans.* Mol Cell Biol, 2000. **20**(11): p. 4084-93.

37. Bruick, R.K. and S.L. McKnight, *A conserved family of prolyl-4-hydroxylases that modify HIF.* Science, 2001. **294**(5545): p. 1337-40.

38. Berra, E., E. Benizri, A. Ginouves, V. Volmat, D. Roux, and J. Pouyssegur, *HIF prolyl-hydroxylase 2 is the key oxygen sensor setting low steady-state levels of HIF-1alpha in normoxia.* EMBO J, 2003. **22**(16): p. 4082-90.

39. West, C.M., H. van der Wel, and Z.A. Wang, *Prolyl 4-hydroxylase-1 mediates O2 signaling during development of Dictyostelium.* Development, 2007. **134**(18): p. 3349-58.

40. Lee, K.A., J.D. Lynd, S. O'Reilly, M. Kiupel, J.J. McCormick, and J.J. LaPres, *The biphasic role of the hypoxia-inducible factor prolyl-4-hydroxylase, PHD2, in modulating tumor-forming potential.* Mol Cancer Res, 2008. **6**(5): p. 829-42.

41. Gorres, K.L., R. Edupuganti, G.R. Krow, and R.T. Raines, *Conformational preferences of substrates for human prolyl 4-hydroxylase.* Biochemistry, 2008. **47**(36): p. 9447-55.

42. Lee, D.W., S. Rajagopalan, A. Siddiq, R. Gwiazda, L. Yang, M.F. Beal, R.R. Ratan, and J.K. Andersen, *Inhibition of prolyl hydroxylase protects against 1-methyl-4-phenyl-*

*1,2,3,6-tetrahydropyridine-induced neurotoxicity: model for the potential involvement of the hypoxia-inducible factor pathway in Parkinson disease.* J Biol Chem, 2009. **284**(42): p. 29065-76.

43. Boyd, D.R. and T.D. Bugg, *Arene cis-dihydrodiol formation: from biology to application.* Org Biomol Chem, 2006. **4**(2): p. 181-92.

44. Kovaleva, E.G., M.B. Neibergall, S. Chakrabarty, and J.D. Lipscomb, *Finding intermediates in the O2 activation pathways of non-heme iron oxygenases.* Acc Chem Res, 2007. **40**(7): p. 475-83.

45. Hayaishi, O., *Crystalline oxygenases of pseudomonads.* Bacteriol Rev, 1966. **30**(4): p. 720-31.

46. Vaillancourt, F.H., J.T. Bolin, and L.D. Eltis, *The ins and outs of ring-cleaving dioxygenases.* Crit Rev Biochem Mol Biol, 2006. **41**(4): p. 241-67.

47. Han, S., L.D. Eltis, K.N. Timmis, S.W. Muchmore, and J.T. Bolin, *Crystal structure of the biphenyl-cleaving extradiol dioxygenase from a PCB-degrading pseudomonad.* Science, 1995. **270**(5238): p. 976-80.

48. Spence, E.L., M. Kawamukai, J. Sanvoisin, H. Braven, and T.D. Bugg, *Catechol dioxygenases from Escherichia coli (MhpB) and Alcaligenes eutrophus (MpcI): sequence analysis and biochemical properties of a third family of extradiol dioxygenases.* J Bacteriol, 1996. **178**(17): p. 5249-56.

49. Kovaleva, E.G. and J.D. Lipscomb, *Crystal structures of Fe2+ dioxygenase superoxo, alkylperoxo, and bound product intermediates.* Science, 2007. **316**(5823): p. 453-7.

50. Sanvoisin, J., G.J. Langley, and T.D.H. Bugg, *Mechanism of Extradiol Catechol Dioxygenases - Evidence for a Lactone Intermediate in the 2,3-Dihydroxyphenylpropionate 1,2-Dioxygenase Reaction.* J Am Chem Soc, 1995. **117**(29): p. 7836-7837.

51. Ohlendorf, D.H., J.D. Lipscomb, and P.C. Weber, *Structure and assembly of protocatechuate 3,4-dioxygenase.* Nature, 1988. **336**(6197): p. 403-5.

52. Andersson, K.K., D.D. Cox, L. Que, Jr., T. Flatmark, and J. Haavik, *Resonance Raman studies on the blue-green-colored bovine adrenal tyrosine 3-monooxygenase (tyrosine hydroxylase). Evidence that the feedback inhibitors adrenaline and noradrenaline are coordinated to iron.* J Biol Chem, 1988. **263**(35): p. 18621-6.

53. Orville, A.M., N. Elango, J.D. Lipscomb, and D.H. Ohlendorf, *Structures of competitive inhibitor complexes of protocatechuate 3,4-dioxygenase: multiple exogenous ligand binding orientations within the active site.* Biochemistry, 1997. **36**(33): p. 10039-51.

54. Orville, A.M., J.D. Lipscomb, and D.H. Ohlendorf, *Crystal structures of substrate and substrate analog complexes of protocatechuate 3,4-dioxygenase: endogenous Fe3+ ligand displacement in response to substrate binding.* Biochemistry, 1997. **36**(33): p. 10052-66.

55. Mayer, R.J. and L. Que, Jr., *18O studies of pyrogallol cleavage by catechol 1,2-dioxygenase.* J Biol Chem, 1984. **259**(21): p. 13056-60.

56. Xin, M. and T.D. Bugg, *Evidence from mechanistic probes for distinct hydroperoxide rearrangement mechanisms in the intradiol and extradiol catechol dioxygenases.* J Am Chem Soc, 2008. **130**(31): p. 10422-30.

57. Gibson, D.T., S.M. Resnick, K. Lee, J.M. Brand, D.S. Torok, L.P. Wackett, M.J. Schocken, and B.E. Haigler, *Desaturation, dioxygenation, and monooxygenation reactions catalyzed by naphthalene dioxygenase from Pseudomonas sp. strain 9816-4.* J Bacteriol, 1995. **177**(10): p. 2615-21.

58. Herman, P.L., M. Behrens, S. Chakraborty, B.M. Chrastil, J. Barycki, and D.P. Weeks, *A three-component dicamba O-demethylase from Pseudomonas maltophilia, strain DI-6:*

*gene isolation, characterization, and heterologous expression.* J Biol Chem, 2005. **280**(26): p. 24759-67.

59. Lee, J. and H. Zhao, *Mechanistic studies on the conversion of arylamines into arylnitro compounds by aminopyrrolnitrin oxygenase: identification of intermediates and kinetic studies.* Angew Chem Int Ed Engl, 2006. **45**(4): p. 622-5.

60. Martins, B.M., T. Svetlitchnaia, and H. Dobbek, *2-Oxoquinoline 8-monooxygenase oxygenase component: active site modulation by Rieske-[2Fe-2S] center oxidation/reduction.* Structure, 2005. **13**(5): p. 817-24.

61. Haigler, B.E. and D.T. Gibson, *Purification and properties of ferredoxinNAP, a component of naphthalene dioxygenase from Pseudomonas sp. strain NCIB 9816.* J Bacteriol, 1990. **172**(1): p. 465-8.

62. Haigler, B.E. and D.T. Gibson, *Purification and properties of NADH-ferredoxinNAP reductase, a component of naphthalene dioxygenase from Pseudomonas sp. strain NCIB 9816.* J Bacteriol, 1990. **172**(1): p. 457-64.

63. Ensley, B.D. and B.E. Haigler, *Naphthalene dioxygenase from Pseudomonas NCIB 9816.* Methods Enzymol, 1990. **188**: p. 46-52.

64. Suen, W.C. and D.T. Gibson, *Isolation and preliminary characterization of the subunits of the terminal component of naphthalene dioxygenase from Pseudomonas putida NCIB 9816-4.* J Bacteriol, 1993. **175**(18): p. 5877-81.

65. Ferraro, D.J., L. Gakhar, and S. Ramaswamy, *Rieske business: structure-function of Rieske non-heme oxygenases.* Biochem Biophys Res Commun, 2005. **338**(1): p. 175-90.

66. Pinto, A., M. Tarasev, and D.P. Ballou, *Substitutions of the "bridging" aspartate 178 result in profound changes in the reactivity of the Rieske center of phthalate dioxygenase.* Biochemistry, 2006. **45**(30): p. 9032-41.

67. Tarasev, M., A. Pinto, D. Kim, S.J. Elliott, and D.P. Ballou, *The "bridging" aspartate 178 in phthalate dioxygenase facilitates interactions between the Rieske center and the iron(II)--mononuclear center.* Biochemistry, 2006. **45**(34): p. 10208-16.

68. Karlsson, A., J.V. Parales, R.E. Parales, D.T. Gibson, H. Eklund, and S. Ramaswamy, *Crystal structure of naphthalene dioxygenase: side-on binding of dioxygen to iron.* Science, 2003. **299**(5609): p. 1039-42.

69. Kauppi, B., K. Lee, E. Carredano, R.E. Parales, D.T. Gibson, H. Eklund, and S. Ramaswamy, *Structure of an aromatic-ring-hydroxylating dioxygenase-naphthalene 1,2-dioxygenase.* Structure, 1998. **6**(5): p. 571-86.

70. Chen, K., M. Costas, J. Kim, A.K. Tipton, and L. Que, Jr., *Olefin cis-dihydroxylation versus epoxidation by non-heme iron catalysts: two faces of an Fe(III)-OOH coin.* J Am Chem Soc, 2002. **124**(12): p. 3026-35.

71. Goodwill, K.E., C. Sabatier, C. Marks, R. Raag, P.F. Fitzpatrick, and R.C. Stevens, *Crystal structure of tyrosine hydroxylase at 2.3 A and its implications for inherited neurodegenerative diseases.* Nat Struct Biol, 1997. **4**(7): p. 578-85.

72. Kobe, B., I.G. Jennings, C.M. House, B.J. Michell, K.E. Goodwill, B.D. Santarsiero, R.C. Stevens, R.G. Cotton, and B.E. Kemp, *Structural basis of autoregulation of phenylalanine hydroxylase.* Nat Struct Biol, 1999. **6**(5): p. 442-8.

73. Wang, L., H. Erlandsen, J. Haavik, P.M. Knappskog, and R.C. Stevens, *Three-dimensional structure of human tryptophan hydroxylase and its implications for the biosynthesis of the neurotransmitters serotonin and melatonin.* Biochemistry, 2002. **41**(42): p. 12569-74.

74. Pavon, J.A. and P.F. Fitzpatrick, *Insights into the catalytic mechanisms of phenylalanine and tryptophan hydroxylase from kinetic isotope effects on aromatic hydroxylation.* Biochemistry, 2006. **45**(36): p. 11030-7.

75. Andersen, O.A., T. Flatmark, and E. Hough, *High resolution crystal structures of the catalytic domain of human phenylalanine hydroxylase in its catalytically active Fe(II) form and binary complex with tetrahydrobiopterin.* J Mol Biol, 2001. **314**(2): p. 279-91.

76. Erlandsen, H., J.Y. Kim, M.G. Patch, A. Han, A. Volner, M.M. Abu-Omar, and R.C. Stevens, *Structural comparison of bacterial and human iron-dependent phenylalanine hydroxylases: similar fold, different stability and reaction rates.* J Mol Biol, 2002. **320**(3): p. 645-61.

77. Baldwin, J.E. and M. Bradley, *Isopenicillin N synthase: mechanistic studies.* Chem Rev, 1990. **90**(7): p. 1079-1088.

78. Roach, P.L., I.J. Clifton, C.M. Hensgens, N. Shibata, C.J. Schofield, J. Hajdu, and J.E. Baldwin, *Structure of isopenicillin N synthase complexed with substrate and the mechanism of penicillin formation.* Nature, 1997. **387**(6635): p. 827-30.

79. Burzlaff, N.I., P.J. Rutledge, I.J. Clifton, C.M. Hensgens, M. Pickford, R.M. Adlington, P.L. Roach, and J.E. Baldwin, *The reaction cycle of isopenicillin N synthase observed by X-ray diffraction.* Nature, 1999. **401**(6754): p. 721-4.

80. Roach, P.L., I.J. Clifton, C.M. Hensgens, N. Shibata, A.J. Long, R.W. Strange, S.S. Hasnain, C.J. Schofield, J.E. Baldwin, and J. Hajdu, *Anaerobic crystallisation of an isopenicillin N synthase.Fe(II).substrate complex demonstrated by X-ray studies.* Eur J Biochem, 1996. **242**(3): p. 736-40.

81. Pirrung, M.C., *Histidine kinases and two-component signal transduction systems.* Chem Biol, 1999. **6**(6): p. R167-75.

82. Zhang, Z., J.S. Ren, I.J. Clifton, and C.J. Schofield, *Crystal structure and mechanistic implications of 1-aminocyclopropane-1-carboxylic acid oxidase--the ethylene-forming enzyme.* Chem Biol, 2004. **11**(10): p. 1383-94.

83. Rocklin, A.M., K. Kato, H.W. Liu, L. Que, Jr., and J.D. Lipscomb, *Mechanistic studies of 1-aminocyclopropane-1-carboxylic acid oxidase: single turnover reaction.* J Biol Inorg Chem, 2004. **9**(2): p. 171-82.

84. Brunhuber, N.M., J.L. Mort, R.E. Christoffersen, and N.O. Reich, *Steady-state kinetic mechanism of recombinant avocado ACC oxidase: initial velocity and inhibitor studies.* Biochemistry, 2000. **39**(35): p. 10730-8.

85. Thrower, J.S., R. Blalock, 3rd, and J.P. Klinman, *Steady-state kinetics of substrate binding and iron release in tomato ACC oxidase.* Biochemistry, 2001. **40**(32): p. 9717-24.

86. Devlin, T.M., *Text book of biochemistry: with clinical correlations*. sixth edition ed. 2005: Wiley-Liss.

87. Lippard, S.J.B., J. M., *Principles of Bioinorganic Chemistry*. 1994.

88. Bulaj, G., T. Kortemme, and D.P. Goldenberg, *Ionization-reactivity relationships for cysteine thiols in polypeptides.* Biochemistry, 1998. **37**(25): p. 8965-72.

89. Baker, D.H. and G.L. Czarnecki-Maulden, *Pharmacologic role of cysteine in ameliorating or exacerbating mineral toxicities.* J Nutr, 1987. **117**(6): p. 1003-10.

90. Kearney, E.B. and W.C. Kenny, *Covalently bound Flavin Coenzymes.* Horiz Biochem Biophys, 1974. **1**: p. 62-96.

91. Huxtable, R.J., *Physiological actions of taurine.* Physiol Rev, 1992. **72**(1): p. 101-63.

92. Powis, G. and W.R. Montfort, *Properties and biological activities of thioredoxins.* Annu Rev Pharmacol Toxicol, 2001. **41**: p. 261-95.

93. Dominy, J.E., Jr., C.R. Simmons, L.L. Hirschberger, J. Hwang, R.M. Coloso, and M.H. Stipanuk, *Discovery and characterization of a second mammalian thiol dioxygenase, cysteamine dioxygenase.* J Biol Chem, 2007. **282**(35): p. 25189-98.

94. Lombardi.Jb, P. Turini, D.R. Biggs, and T.P. Singer, *Cysteine Oxygenase .1. General Properties.* Physiol Chem Phys, 1969. **1**(1): p. 1-&.

95. Ewetz, L. and B. Sorbo, *Characteristics of the cysteinesulfinate-forming enzyme system in rat liver.* Biochim Biophys Acta, 1966. **128**(2): p. 296-305.

96. Yamaguchi, K., Y. Hosokawa, N. Kohashi, Y. Kori, S. Sakakibara, and I. Ueda, *Rat liver cysteine dioxygenase (cysteine oxidase). Further purification, characterization, and analysis of the activation and inactivation.* J Biochem, 1978. **83**(2): p. 479-91.

97. Yamaguchi, K. and Y. Hosokawa, *Cysteine dioxygenase.* Methods Enzymol, 1987. **143**: p. 395-403.

98. Ye, S., X. Wu, L. Wei, D. Tang, P. Sun, M. Bartlam, and Z. Rao, *An insight into the mechanism of human cysteine dioxygenase. Key roles of the thioether-bonded tyrosine-cysteine cofactor.* J Biol Chem, 2007. **282**(5): p. 3391-402.

99. Dominy, J.E., Jr., J. Hwang, S. Guo, L.L. Hirschberger, S. Zhang, and M.H. Stipanuk, *Synthesis of amino acid cofactor in cysteine dioxygenase is regulated by substrate and represents a novel post-translational regulation of activity.* J Biol Chem, 2008. **283**(18): p. 12188-201.

100. Woo, E.J., J.M. Dunwell, P.W. Goodenough, A.C. Marvier, and R.W. Pickersgill, *Germin is a manganese containing homohexamer with oxalate oxidase and superoxide dismutase activities.* Nat Struct Biol, 2000. **7**(11): p. 1036-40.

101. Ito, N., S.E. Phillips, C. Stevens, Z.B. Ogel, M.J. McPherson, J.N. Keen, K.D. Yadav, and P.F. Knowles, *Novel thioether bond revealed by a 1.7 A crystal structure of galactose oxidase.* Nature, 1991. **350**(6313): p. 87-90.

102. Schnell, R., T. Sandalova, U. Hellman, Y. Lindqvist, and G. Schneider, *Siroheme- and [Fe4-S4]-dependent NirA from Mycobacterium tuberculosis is a sulfite reductase with a covalent Cys-Tyr bond in the active site.* J Biol Chem, 2005. **280**(29): p. 27319-28.

103. Diaz, A., E. Horjales, E. Rudino-Pinera, R. Arreola, and W. Hansberg, *Unusual Cys-Tyr covalent bond in a large catalase.* J Mol Biol, 2004. **342**(3): p. 971-85.

104. Pierce, B.S., J.D. Gardner, L.J. Bailey, T.C. Brunold, and B.G. Fox, *Characterization of the nitrosyl adduct of substrate-bound mouse cysteine dioxygenase by electron paramagnetic resonance: electronic structure of the active site and mechanistic implications.* Biochemistry, 2007. **46**(29): p. 8569-78.

105. Guionrain, M.C., C. Portemer, and F. Chatagner, *Rat-Liver Cysteine Sulfinate Decarboxylase - Purification, New Appraisal of Molecular-Weight and Determination of Catalytic Properties.* Biochimica Et Biophysica Acta, 1975. **384**(1): p. 265-276.

106. Waditee, R. and A. Incharoensakdi, *Purification and kinetic properties of betaine-homocysteine methyltransferase from Aphanothece halophytica.* Curr Microbiol, 2001. **43**(2): p. 107-11.

107. Skovby, F., J.P. Kraus, and L.E. Rosenberg, *Biosynthesis of human cystathionine beta-synthase in cultured fibroblasts.* J Biol Chem, 1984. **259**(1): p. 583-7.

108. Crawford, J.A., W. Li, and B.S. Pierce, *Single turnover of substrate-bound ferric cysteine dioxygenase with superoxide anion: enzymatic reactivation, product formation, and a transient intermediate.* Biochemistry, 2011. **50**(47): p. 10241-53.

109. Whittaker, J.W., *The radical chemistry of galactose oxidase.* Arch Biochem Biophys, 2005. **433**(1): p. 227-39.

110. Weinstein, C.L., R.H. Haschemeyer, and O.W. Griffith, *In vivo studies of cysteine metabolism. Use of D-cysteinesulfinate, a novel cysteinesulfinate decarboxylase inhibitor, to probe taurine and pyruvate synthesis.* J Biol Chem, 1988. **263**(32): p. 16568-79.

111. Pean, A.R., R.B. Parsons, R.H. Waring, A.C. Williams, and D.B. Ramsden, *Toxicity of sulphur-containing compounds to neuronal cell lines.* J Neurol Sci, 1995. **129 Suppl**: p. 107-8.

112. Parsons, R.B., R.H. Waring, D.B. Ramsden, and A.C. Williams, *In vitro effect of the cysteine metabolites homocysteic acid, homocysteine and cysteic acid upon human neuronal cell lines.* Neurotoxicology, 1998. **19**(4-5): p. 599-603.

113. Perry, T.L., M.G. Norman, V.W. Yong, S. Whiting, J.U. Crichton, S. Hansen, and S.J. Kish, *Hallervorden-Spatz disease: cysteine accumulation and cysteine dioxygenase deficiency in the globus pallidus.* Ann Neurol, 1985. **18**(4): p. 482-9.

114. Emery, P., H. Bradley, V. Arthur, E. Tunn, and R. Waring, *Genetic factors influencing the outcome of early arthritis--the role of sulphoxidation status.* Br J Rheumatol, 1992. **31**(7): p. 449-51.

115. Yang, Y., Y.C. Fan, S. Gao, C.Y. Dou, J.J. Zhang, F.K. Sun, and K. Wang, *Methylated cysteine dioxygenase-1 gene promoter in the serum is a potential biomarker for hepatitis B virus-related hepatocellular carcinoma.* Tohoku J Exp Med, 2014. **232**(3): p. 187-94.

116. Hagiwara, A., S. Ishizaki, K. Takehana, S. Fujitani, I. Sonaka, H. Satsu, and M. Shimizu, *Branched-chain amino acids inhibit the TGF-beta-induced down-regulation of taurine biosynthetic enzyme cysteine dioxygenase in HepG2 cells.* Amino Acids, 2014.

117. Stipanuk, M.H., *Sulfur amino acid metabolism: pathways for production and removal of homocysteine and cysteine.* Annu Rev Nutr, 2004. **24**: p. 539-77.

118. Soerbo, B. and L. Ewetz, *The Enzymatic Oxidation of Cysteine to Cysteinesulfinate in Rat Liver.* Biochem Biophys Res Commun, 1965. **18**: p. 359-63.

119. Lombardi.Jb, T.P. Singer, and P.D. Boyer, *Cysteine Oxygenase .2. Studies on Mechanism of Reaction with 18oxygen.* J Biol Chem, 1969. **244**(5): p. 1172-&.

120. Stipanuk, M.H., C.R. Simmons, P.A. Karplus, and J.E. Dominy, Jr., *Thiol dioxygenases: unique families of cupin proteins.* Amino Acids, 2011. **41**(1): p. 91-102.

121. Stipanuk, M.H., L.L. Hirschberger, M.P. Londono, C.L. Cresenzi, and A.F. Yu, *The ubiquitin-proteasome system is responsible for cysteine-responsive regulation of cysteine dioxygenase concentration in liver.* Am J Physiol Endocrinol Metab, 2004. **286**(3): p. E439-48.

122. Deth, R., C. Muratore, J. Benzecry, V.A. Power-Charnitsky, and M. Waly, *How environmental and genetic factors combine to cause autism: A redox/methylation hypothesis.* Neurotoxicology, 2008. **29**(1): p. 190-201.

123. James, S.J., P. Cutler, S. Melnyk, S. Jernigan, L. Janak, D.W. Gaylor, and J.A. Neubrander, *Metabolic biomarkers of increased oxidative stress and impaired methylation capacity in children with autism.* Am J Clin Nutr, 2004. **80**(6): p. 1611-1617.

124. Gordon, C., H. Bradley, R.H. Waring, and P. Emery, *Abnormal Sulfur Oxidation in Systemic Lupus-Erythematosus.* Lancet, 1992. **339**(8784): p. 25-26.

125. Simmons, C.R., L.L. Hirschberger, M.S. Machi, and M.H. Stipanuk, *Expression, purification, and kinetic characterization of recombinant rat cysteine dioxygenase, a non-heme metalloenzyme necessary for regulation of cellular cysteine levels.* Protein Expression and Purification, 2006. **47**(1): p. 74-81.

126. Heafield, M.T., S. Fearn, G.B. Steventon, R.H. Waring, A.C. Williams, and S.G. Sturman, *Plasma Cysteine and Sulfate Levels in Patients with Motor-Neuron, Parkinsons and Alzheimers-Disease.* Neuroscience Letters, 1990. **110**(1-2): p. 216-220.

127. Straganz, G.D. and B. Nidetzky, *Variations of the 2-His-1-carboxylate theme in mononuclear non-heme FeII oxygenases.* Chembiochem, 2006. **7**(10): p. 1536-48.

128. Keszei, A.P., L.J. Schouten, A.L. Driessen, C.J. Huysentruyt, Y.C. Keulemans, R.A. Goldbohm, and P.A. van den Brandt, *Vegetable, fruit and nitrate intake in relation to the risk of Barrett's oesophagus in a large Dutch cohort.* Br J Nutr, 2014. **111**(8): p. 1452-62.

129. Diebold, A.R., M.L. Neidig, G.R. Moran, G.D. Straganz, and E.I. Solomon, *The three-his triad in Dke1: comparisons to the classical facial triad.* Biochemistry, 2010. **49**(32): p. 6945-52.

130. Straganz, G.D., A.R. Diebold, S. Egger, B. Nidetzky, and E.I. Solomon, *Kinetic and CD/MCD spectroscopic studies of the atypical, three-His-ligated, non-heme Fe2+ center in diketone dioxygenase: the role of hydrophilic outer shell residues in catalysis.* Biochemistry, 2010. **49**(5): p. 996-1004.

131. Ito, N., S.E.V. Phillips, C. Stevens, Z.B. Ogel, M.J. Mcpherson, J.N. Keen, K.D.S. Yadav, and P.F. Knowles, *Novel Thioether Bond Revealed by a 1.7-a Crystal-Structure of Galactose-Oxidase.* Nature, 1991. **350**(6313): p. 87-90.

132. Schnell, R., T. Sandalova, U. Hellman, Y. Lindqvist, and G. Schneider, *Siroheme- and [Fe-4-S-4]-dependent NirA from Mycobacterium tuberculosis is a sulfite reductase with a covalent Cys-Tyr bond in the active site.* J Biol Chem, 2005. **280**(29): p. 27319-27328.

133. Whittaker, J.W., *Free radical catalysis by galactose oxidase.* Chemical Reviews, 2003. **103**(6): p. 2347-2363.

134. Kumar, D., W. Thiel, and S.P. de Visser, *Theoretical study on the mechanism of the oxygen activation process in cysteine dioxygenase enzymes.* J Am Chem Soc, 2011. **133**(11): p. 3869-82.

135. de Visser, S.P. and G.D. Straganz, *Why Do Cysteine Dioxygenase Enzymes Contain a 3-His Ligand Motif Rather than a 2His/1Asp Motif Like Most Nonheme Dioxygenases?* J Phys Chem A, 2009. **113**(9): p. 1835-1846.

136. Aluri, S. and S.P. de Visser, *The mechanism of cysteine oxygenation by cysteine dioxygenase enzymes.* J Am Chem Soc, 2007. **129**(48): p. 14846-7.

137. Fujimori, D.G., E.W. Barr, M.L. Matthews, G.M. Koch, J.R. Yonce, C.T. Walsh, J.M. Bollinger, Jr., C. Krebs, and P.J. Riggs-Gelasco, *Spectroscopic evidence for a high-spin Br-Fe(IV)-oxo intermediate in the alpha-ketoglutarate-dependent halogenase CytC3 from Streptomyces.* J Am Chem Soc, 2007. **129**(44): p. 13408-9.

138. Lange, S.J., H. Miyake, and L. Que, *Evidence for a nonheme Fe(IV)=O species in the intramolecular hydroxylation of a phenyl moiety.* J Am Chem Soc, 1999. **121**(26): p. 6330-6331.

139. Lim, M.H., J.U. Rohde, A. Stubna, M.R. Bukowski, M. Costas, R.Y.N. Ho, E. Munck, W. Nam, and L. Que, *An Fe-IV = O complex of a tetradentate tripodal nonheme ligand.* Proc Natl Acad Sci U S A, 2003. **100**(7): p. 3665-3670.

140. Tyler, L.A., J.C. Noveron, M.M. Olmstead, and P.K. Mascharak, *Oxidation of metal-bound thiolato sulfur centers in Fe(III) and Co(III) complexes with carboxamido nitrogens and thiolato sulfurs as donors: Relevance to the active sites of nitrile hydratases.* Inorg Chem, 1999. **38**(4): p. 616-+.

141. Kung, I., D. Schweitzer, J. Shearer, W.D. Taylor, H.L. Jackson, S. Lovell, and J.A. Kovacs, *How do oxidized thiolate ligands affect the electronic and reactivity properties of a nitrile hydratase model compound?* J Am Chem Soc, 2000. **122**(34): p. 8299-8300.

142. Buonomo, R.M., I. Font, M.J. Maguire, J.H. Reibenspies, T. Tuntulani, and M.Y. Darensbourg, *Study of Sulfinate and Sulfenate Complexes Derived from the Oxygenation of Thiolate Sulfur in [1,5-Bis(2-Mercapto-2-Methylpropyl)-1,5-Diazatyclooctanato(2-)]Nickel(Ii) (Vol 117, Pg 963, 1995).* J Am Chem Soc, 1995. **117**(19): p. 5427-5427.

143. Dey, A., M. Chow, K. Taniguchi, P. Lugo-Mas, S. Davin, M. Maeda, J.A. Kovacs, M. Odaka, K.O. Hodgson, B. Hedman, and E.I. Solomon, *Sulfur K-Edge XAS and DFT calculations on nitrile hydratase: Geometric and electronic structure of the non-heme iron active site.* J Am Chem Soc, 2006. **128**(2): p. 533-541.

144. Simmons, C.R., K. Krishnamoorthy, S.L. Granett, D.J. Schuller, J.E. Dominy, Jr., T.P. Begley, M.H. Stipanuk, and P.A. Karplus, *A putative Fe2+-bound persulfenate intermediate in cysteine dioxygenase.* Biochemistry, 2008. **47**(44): p. 11390-2.

145. Maroney, M.J., S.B. Choudhury, P.A. Bryngelson, S.A. Mirza, and M.J. Sherrod, *Theoretical Study of the Oxidation of Nickel Thiolate Complexes by O(2).* Inorg Chem, 1996. **35**(4): p. 1073-1076.

146. Mirza, S.A., M.A. Pressler, M. Kumar, R.O. Day, and M.J. Maroney, *Oxidation of Nickel Thiolate Ligands by Dioxygen.* Inorg Chem, 1993. **32**(6): p. 977-987.

147. Kovaleva, E.G. and J.D. Lipscomb, *Crystal structures of Fe2+ dioxygenase superoxo, alkylperoxo, and bound product intermediates.* Science, 2007. **316**(5823): p. 453-457.

148. Rocklin, A.M., D.L. Tierney, V. Kofman, N.M. Brunhuber, B.M. Hoffman, R.E. Christoffersen, N.O. Reich, J.D. Lipscomb, and L. Que, Jr., *Role of the nonheme Fe(II) center in the biosynthesis of the plant hormone ethylene.* Proc Natl Acad Sci U S A, 1999. **96**(14): p. 7905-9.

149. Hirao, H. and K. Morokuma, *Ferric Superoxide and Ferric Hydroxide Are Used in the Catalytic Mechanism of Hydroxyethylphosphonate Dioxygenase: A Density Functional Theory Investigation.* J Am Chem Soc, 2010. **132**(50): p. 17901-17909.

150. Mbughuni, M.M., M. Chakrabarti, J.A. Hayden, E.L. Bominaar, M.P. Hendrich, E. Munck, and J.D. Lipscomb, *Trapping and spectroscopic characterization of an Fe-III-superoxo intermediate from a nonheme mononuclear iron-containing enzyme.* Proc Natl Acad Sci U S A, 2010. **107**(39): p. 16788-16793.

151. Emerson, J.P., E.G. Kovaleva, E.R. Farquhar, J.D. Lipscomb, and L. Que, *Swapping metals in Fe- and Mn-dependent dioxygenases: Evidence for oxygen activation without a change in metal redox state.* Proc Natl Acad Sci U S A, 2008. **105**(21): p. 7347-7352.

152. Gunderson, W.A., A.I. Zatsman, J.P. Emerson, E.R. Farquhar, L. Que, J.D. Lipscomb, and M.P. Hendrich, *Electron Paramagnetic Resonance Detection of Intermediates in the Enzymatic Cycle of an Extradiol Dioxygenase.* J Am Chem Soc, 2008. **130**(44): p. 14465-+.

153. Gardner, J.D., B.S. Pierce, B.G. Fox, and T.C. Brunold, *Spectroscopic and Computational Characterization of Substrate-Bound Mouse Cysteine Dioxygenase: Nature of the Ferrous and Ferric Cysteine Adducts and Mechanistic Implications.* Biochemistry, 2010. **49**(29): p. 6033-6041.

154. Fridovich, I., *Quantitative aspects of the production of superoxide anion radical by milk xanthine oxidase.* J Biol Chem, 1970. **245**(16): p. 4053-7.

155. McCord, J.M. and I. Fridovich, *The reduction of cytochrome c by milk xanthine oxidase.* J Biol Chem, 1968. **243**(21): p. 5753-60.

156. McCord, J.M. and I. Fridovich, *Superoxide dismutase. An enzymic function for erythrocuprein (hemocuprein).* J Biol Chem, 1969. **244**(22): p. 6049-55.

157. Crack, J.C., J. Green, M.R. Cheesman, N.E. Le Brun, and A.J. Thomson, *Superoxide-mediated amplification of the oxygen-induced switch from [4Fe-4S] to [2Fe-2S] clusters in the transcriptional regulator FNR.* Proc Natl Acad Sci U S A, 2007. **104**(7): p. 2092-7.

158. Abragam, A.a.B., B., *Electron Paramagnetic Resonance of Transition Ions*, in *International Series of Monographs on Physics*. 1970.

159. Kwiatkowski, L.D., M. Adelman, R. Pennelly, and D.J. Kosman, *Kinetic mechanism of the Cu(II) enzyme galactose oxidase.* J Inorg Biochem, 1981. **14**(3): p. 209-22.

160. Niviere, V., M. Asso, C.O. Weill, M. Lombard, B. Guigliarelli, V. Favaudon, and C. Houee-Levin, *Superoxide reductase from Desulfoarculus baarsii: identification of protonation steps in the enzymatic mechanism.* Biochemistry, 2004. **43**(3): p. 808-18.

161. Whittaker, M.M., P.J. Kersten, D. Cullen, and J.W. Whittaker, *Identification of catalytic residues in glyoxal oxidase by targeted mutagenesis.* J Biol Chem, 1999. **274**(51): p. 36226-32.

162. Ghiladi, R.A., K.F. Medzihradszky, F.M. Rusnak, and P.R. de Montellano, *Correlation between isoniazid resistance and superoxide reactivity in Mycobacterium tuberculosis KatG.* J Am Chem Soc, 2005. **127**(38): p. 13428-13442.

163. Kono, Y. and I. Fridovich, *Superoxide Radical Inhibits Catalase.* J Biol Chem, 1982. **257**(10): p. 5751-5754.

164. Shimizu, N., K. Kobayashi, and K. Hayashi, *The Reaction of Superoxide Radical with Catalase - Mechanism of the Inhibition of Catalase by Superoxide Radical.* J Biol Chem, 1984. **259**(7): p. 4414-4418.

165. Sawyer, D.T. and J.S. Valentine, *How Super Is Superoxide.* Accounts of Chemical Research, 1981. **14**(12): p. 393-400.

166. Wood, P.M., *The 2 Redox Potentials for Oxygen Reduction to Superoxide.* Trends Biochem Sci, 1987. **12**(7): p. 250-251.

167. Granum, D.M., P.J. Riedel, J.A. Crawford, T.K. Mahle, C.M. Wyss, A.K. Begej, N. Arulsamy, B.S. Pierce, and M.P. Mehn, *Synthesis and Characterization of Sterically Encumbered beta-Ketoiminate Complexes of Iron(II) and Zinc(II).* Dalton Transactions, 2011. **40**(22): p. 5881-5890.

168. Clay, M.D., J.P. Emerson, E.D. Coulter, D.M. Kurtz, Jr., and M.K. Johnson, *Spectroscopic characterization of the [Fe(His)(4)(Cys)] site in 2Fe-superoxide reductase from Desulfovibrio vulgaris.* J Biol Inorg Chem, 2003. **8**(6): p. 671-82.

169. Chai, S.C., J.R. Bruyere, and M.J. Maroney, *Probes of the catalytic site of cysteine dioxygenase.* J Biol Chem, 2006. **281**(23): p. 15774-9.

170. Sakakibara, S., K. Yamaguchi, Y. Hosokawa, N. Kohashi, I. Ueda, and Y. Sakamoto, *Purification and Some Properties of Rat-Liver Cysteine Oxidase (Cysteine Dioxygenase).* Biochim Biophys Acta, 1976. **422**(2): p. 273-279.

171. Denisov, I.G., P.J. Mak, T.M. Makris, S.G. Sligar, and J.R. Kincaid, *Resonance Raman characterization of the peroxo and hydroperoxo intermediates in cytochrome P450.* J Phys Chem A, 2008. **112**(50): p. 13172-9.

172. Galinato, M.G., T. Spolitak, D.P. Ballou, and N. Lehnert, *Elucidating the role of the proximal cysteine hydrogen-bonding network in ferric cytochrome P450cam and corresponding mutants using magnetic circular dichroism spectroscopy.* Biochemistry, 2011. **50**(6): p. 1053-69.

173. Hirotsu, S., G.C. Chu, M. Unno, D.S. Lee, T. Yoshida, S.Y. Park, Y. Shiro, and M. Ikeda-Saito, *The crystal structures of the ferric and ferrous forms of the heme complex of HmuO, a heme oxygenase of Corynebacterium diphtheriae.* J Biol Chem, 2004. **279**(12): p. 11937-47.

174. Xing, G., Y. Diao, L.M. Hoffart, E.W. Barr, K.S. Prabhu, R.J. Arner, C.C. Reddy, C. Krebs, and J.M. Bollinger, Jr., *Evidence for C-H cleavage by an iron-superoxide complex in the glycol cleavage reaction catalyzed by myo-inositol oxygenase.* Proc Natl Acad Sci U S A, 2006. **103**(16): p. 6130-5.

175. Saleh, L., C. Krebs, B.A. Ley, S. Naik, B.H. Huynh, and J.M. Bollinger, *Use of a chemical trigger for electron transfer to characterize a precursor to cluster X in assembly of the iron-radical cofactor of Escherichia coli ribonucleotide reductase.* Biochemistry, 2004. **43**(20): p. 5953-5964.

176. Saleh, L., B.A. Kelch, B.A. Pathickal, J. Baldwin, B.A. Ley, and J.M. Bollinger, *Mediation by indole analogues of electron transfer during oxygen activation in variants of Escherichia coli ribonucleotide reductase R2 lacking the electron-shuttling tryptophan 48.* Biochemistry, 2004. **43**(20): p. 5943-5952.

177. Grzyska, P.K., T.A. Muller, M.G. Campbell, and R.P. Hausinger, *Metal ligand substitution and evidence for quinone formation in taurine/alpha-ketoglutarate dioxygenase.* J Inorg Biochem, 2007. **101**(5): p. 797-808.

178. Vojtechovsky, J., K. Chu, J. Berendzen, R.M. Sweet, and I. Schlichting, *Crystal structures of myoglobin-ligand complexes at near-atomic resolution.* Biophys J, 1999. **77**(4): p. 2153-2174.

179. Mukherjee, A., M.A. Cranswick, M. Chakrabarti, T.K. Paine, K. Fujisawa, E. Munck, and L. Que, *Oxygen Activation at Mononuclear Nonheme Iron Centers: A Superoxo Perspective.* Inorg Chem, 2010. **49**(8): p. 3618-3628.

180. Roelfes, G., V. V, K. Chen, R.Y.N. Ho, J.U. Rohde, C. Zondervan, R.M. la Crois, E.P. Schudde, M. Lutz, A.L. Spek, R. Hage, B.L. Feringa, E. Munck, and L. Que, *End-on and side-on peroxo derivatives of non-heme iron complexes with pentadentate ligands: Models for putative intermediates in biological iron/dioxygen chemistry.* Inorg Chem, 2003. **42**(8): p. 2639-2653.

181. van der Donk, W.A., C. Krebs, and J.M. Bollinger, *Substrate activation by iron superoxo intermediates.* Curr Opin Struct Biol, 2010. **20**(6): p. 673-683.

182. Reddie, K.G. and K.S. Carroll, *Expanding the functional diversity of proteins through cysteine oxidation.* Curr Opin Chem Biol, 2008. **12**(6): p. 746-754.

183. Winyard, P.G., C.J. Moody, and C. Jacob, *Oxidative activation of antioxidant defence.* Trends Biochem Sci, 2005. **30**(8): p. 453-461.

184. Trachootham, D., J. Alexandre, and P. Huang, *Targeting cancer cells by ROS-mediated mechanisms: a radical therapeutic approach?* Nat Rev Drug Discov, 2009. **8**(7): p. 579-591.

185. Bhave, D.P., W.B. Muse, 3rd, and K.S. Carroll, *Drug targets in mycobacterial sulfur metabolism.* Infect Disord Drug Targets, 2007. **7**(2): p. 140-58.

186. Dominy, J.E., Jr., C.R. Simmons, P.A. Karplus, A.M. Gehring, and M.H. Stipanuk, *Identification and characterization of bacterial cysteine dioxygenases: a new route of cysteine degradation for eubacteria.* J Bacteriol, 2006. **188**(15): p. 5561-9.

187. Adams, M.A., V.K. Singh, B.O. Keller, and Z.C. Jia, *Structural and biochemical characterization of gentisate 1,2-dioxygenase from Escherichia coli O157 : H7.* Mol Microbiol, 2006. **61**(6): p. 1469-1484.

188. Krebs, C., D. Galonic Fujimori, C.T. Walsh, and J.M. Bollinger, Jr., *Non-heme Fe(IV)-oxo intermediates.* Acc Chem Res, 2007. **40**(7): p. 484-92.

189. Kurtz, D.M., Jr., *Avoiding high-valent iron intermediates: superoxide reductase and rubrerythrin.* J Inorg Biochem, 2006. **100**(4): p. 679-93.

190. Matthews, M.L., C.M. Krest, E.W. Barr, F.H. Vaillancourt, C.T. Walsh, M.T. Green, C. Krebs, and J.M. Bollinger, *Substrate-triggered formation and remarkable stability of the C-H bond-cleaving chloroferryl intermediate in the aliphatic halogenase, SyrB2.* Biochemistry, 2009. **48**(20): p. 4331-43.

191. Makris, T.M., M. Chakrabarti, E. Munck, and J.D. Lipscomb, *A family of diiron monooxygenases catalyzing amino acid beta-hydroxylation in antibiotic biosynthesis.* Proc Natl Acad Sci U S A, 2010. **107**(35): p. 15391-6.

192. Diaz, A., E. Horjales, E. Rudino-Pinera, R. Arreola, and W. Hansberg, *Unusual Cys-Tyr covalent bond in a large catalase.* Journal of Molecular Biology, 2004. **342**(3): p. 971-985.

193. Koehntop, K.D., S. Marimanikkuppam, M.J. Ryle, R.P. Hausinger, and L. Que, Jr., *Self-hydroxylation of taurine/alpha-ketoglutarate dioxygenase: evidence for more than one oxygen activation mechanism.* J Biol Inorg Chem, 2006. **11**(1): p. 63-72.

194. Ryle, M.J., K.D. Koehntop, A. Liu, L. Que, Jr., and R.P. Hausinger, *Interconversion of two oxidized forms of taurine/alpha-ketoglutarate dioxygenase, a non-heme iron hydroxylase: evidence for bicarbonate binding.* Proc Natl Acad Sci U S A, 2003. **100**(7): p. 3790-5.

195. Ge, Y., B.G. Lawhorn, M. ElNaggar, S.K. Sze, T.P. Begley, and F.W. McLafferty, *Detection of four oxidation sites in viral prolyl-4-hydroxylase by top-down mass spectrometry.* Protein Sci, 2003. **12**(10): p. 2320-6.

196. Farquhar, E.R., K.D. Koehntop, J.P. Emerson, and L. Que, Jr., *Post-translational self-hydroxylation: a probe for oxygen activation mechanisms in non-heme iron enzymes.* Biochem Biophys Res Commun, 2005. **338**(1): p. 230-9.

197. Myllyla, R., K. Majamaa, V. Gunzler, H.M. Hanauskeabel, and K.I. Kivirikko, *Ascorbate Is Consumed Stoichiometrically in the Uncoupled Reactions Catalyzed by Prolyl 4-Hydroxylase and Lysyl Hydroxylase.* J Biol Chem, 1984. **259**(9): p. 5403-5405.

198. Siakkou, E., M.T. Rutledge, S.M. Wilbanks, and G.N. Jameson, *Correlating crosslink formation with enzymatic activity in cysteine dioxygenase.* Biochim Biophys Acta, 2011. **1814**(12): p. 2003-9.

199. Mbughuni, M.M., M. Chakrabarti, J.A. Hayden, E.L. Bominaar, M.P. Hendrich, E. Munck, and J.D. Lipscomb, *Trapping and spectroscopic characterization of an FeIII-superoxo intermediate from a nonheme mononuclear iron-containing enzyme.* Proc Natl Acad Sci U S A, 2010. **107**(39): p. 16788-93.

200. Hayden, J.A., E.R. Farquhar, L. Que, J.D. Lipscomb, and M.P. Hendrich, *NO binding to Mn-substituted homoprotocatechuate 2,3-dioxygenase: relationship to O-2 reactivity.* J Biol Inorg Chem, 2013. **18**(7): p. 717-728.

201. Groce, S.L. and J.D. Lipscomb, *Conversion of extradiol aromatic ring-cleaving homoprotocatechuate 2,3-dioxygenase into an intradiol cleaving enzyme.* J Am Chem Soc, 2003. **125**(39): p. 11780-11781.

202. Lee, C.T., W.T. Yang, and R.G. Parr, *Development of the Colle-Salvetti Correlation-Energy Formula into a Functional of the Electron-Density.* Physical Review B, 1988. **37**(2): p. 785-789.

203. Becke, A.D., *Density-Functional Thermochemistry .3. The Role of Exact Exchange.* J Chem Phys, 1993. **98**(7): p. 5648-5652.

204. Hehre, W.J., Ditchfie.R, and J.A. Pople, *Self-Consistent Molecular-Orbital Methods .12. Further Extensions of Gaussian-Type Basis Sets for Use in Molecular-Orbital Studies of Organic-Molecules.* Journal of Chemical Physics, 1972. **56**(5): p. 2257-&.

205. Schafer, A., H. Horn, and R. Ahlrichs, *Fully Optimized Contracted Gaussian-Basis Sets for Atoms Li to Kr.* J Chem Phys, 1992. **97**(4): p. 2571-2577.

206. Cornell, W.D., P. Cieplak, C.I. Bayly, I.R. Gould, K.M. Merz, D.M. Ferguson, D.C. Spellmeyer, T. Fox, J.W. Caldwell, and P.A. Kollman, *A 2nd Generation Force-Field for the Simulation of Proteins, Nucleic-Acids, and Organic-Molecules.* J Am Chem Soc, 1995. **117**(19): p. 5179-5197.

207. Word, J.M., S.C. Lovell, J.S. Richardson, and D.C. Richardson, *Asparagine and glutamine: Using hydrogen atom contacts in the choice of side-chain amide orientation.* J Mol Biol, 1999. **285**(4): p. 1735-1747.

208. Adamo, C. and V. Barone, *Toward reliable density functional methods without adjustable parameters: The PBE0 model.* J Chem Phys, 1999. **110**(13): p. 6158-6170.

209. Neese, F., *Prediction and interpretation of the Fe-57 isomer shift in Mossbauer spectra by density functional theory.* Inorg Chim Acta, 2002. **337**: p. 181-192.

210. Wachters, A.J., *Gaussian Basis Set for Molecular Wavefunctions Containing Third-Row Atoms.* J Chem Phys, 1970. **52**(3): p. 1033-&.

211. Hendrich, M.P. and P.G. Debrunner, *Integer-spin electron paramagnetic resonance of iron proteins.* Biophys J, 1989. **56**(3): p. 489-506.

212. Taylor, C.P., *The EPR of low spin heme complexes. Relation of the t2g hole model to the directional properties of the g tensor, and a new method for calculating the ligand field parameters.* Biochim Biophys Acta, 1977. **491**(1): p. 137-48.

213. Clay, M.D., F.E. Jenney, Jr., P.L. Hagedoorn, G.N. George, M.W. Adams, and M.K. Johnson, *Spectroscopic studies of Pyrococcus furiosus superoxide reductase: implications for active-site structures and the catalytic mechanism.* J Am Chem Soc, 2002. **124**(5): p. 788-805.

214. Popescu, V.C., E. Munck, B.G. Fox, Y. Sanakis, J.G. Cummings, I.M. Turner, Jr., and M.J. Nelson, *Mossbauer and EPR studies of the photoactivation of nitrile hydratase.* Biochemistry, 2001. **40**(27): p. 7984-91.

215. Neese, F., *Prediction of electron paramagnetic resonance g values using coupled perturbed Hartree-Fock and Kohn-Sham theory.* J Chem Phys, 2001. **115**(24): p. 11080-11096.

216. Seo, D.K., *Density functional perturbational orbital theory of spin polarization in electronic systems. I. Formalism.* J Chem Phys, 2006. **125**(15).

217. Sono, M., M.P. Roach, E.D. Coulter, and J.H. Dawson, *Heme-containing oxygenases.* Chem Rev, 1996. **96**(7): p. 2841-2887.

218. Gordon, C., H. Bradley, R.H. Waring, and P. Emery, *Abnormal sulphur oxidation in systemic lupus erythematosus.* Lancet, 1992. **339**(8784): p. 25-6.

219. Heafield, M.T., S. Fearn, G.B. Steventon, R.H. Waring, A.C. Williams, and S.G. Sturman, *Plasma cysteine and sulphate levels in patients with motor neurone, Parkinson's and Alzheimer's disease.* Neurosci Lett, 1990. **110**(1-2): p. 216-20.

220. Li, W., E.J. Blaesi, M.D. Pecore, J.K. Crowell, and B.S. Pierce, *Second-sphere interactions between the C93-Y157 cross-link and the substrate-bound Fe site influence the O(2) coupling efficiency in mouse cysteine dioxygenase.* Biochemistry, 2013. **52**(51): p. 9104-19.

221. Li, W., E.J. Blaesi, M.D. Pecore, J.K. Crowell, and B.S. Pierce, *Second-sphere interactions between the C93-Y157 cross-link and the substrate-bound Fe site influence the O2 coupling efficiency in mouse cysteine dioxygenase.* Biochemistry, 2013. **52**(51): p. 9104-19.

222. Bruland, N., J.H. Wubbeler, and A. Steinbuchel, *3-mercaptopropionate dioxygenase, a cysteine dioxygenase homologue, catalyzes the initial step of 3-mercaptopropionate catabolism in the 3,3-thiodipropionic acid-degrading bacterium variovorax paradoxus.* J Biol Chem, 2009. **284**(1): p. 660-72.

223. Brandt, U., C. Waletzko, B. Voigt, M. Hecker, and A. Steinbuchel, *Mercaptosuccinate metabolism in Variovorax paradoxus strain B4-a proteomic approach.* Appl Microbiol Biotechnol, 2014. **98**(13): p. 6039-50.

224. Lombardini, J.B., T.P. Singer, and P.D. Boyer, *Cystein oxygenase. II. Studies on the mechanism of the reaction with 18oxygen.* J Biol Chem, 1969. **244**(5): p. 1172-5.

225. Misra, C.H., *In vitro study of cysteine oxidase in rat brain.* Neurochem Res, 1983. **8**(11): p. 1497-508.

226. Glasoe, P.K. and F.A. Long, *Use of Glass Electrodes to Measure Acidities in Deuterium Oxide.* J Phys Chem, 1960. **64**(1): p. 188-190.

227. Greenfield, N.J., *Using circular dichroism spectra to estimate protein secondary structure.* Nat. Protocols, 2007. **1**(6): p. 2876-2890.

228. Yost, R.A. and D.D. Fetterolf, *Tandem mass spectrometry (MS/MS) instrumentation.* Mass Spectrom Rev., 1983. **2**(1): p. 1-45.

229. Kasperova, A., J. Kunert, M. Horynova, E. Weigl, M. Sebela, R. Lenobel, and M. Raska, *Isolation of recombinant cysteine dioxygenase protein from Trichophyton mentagrophytes.* Mycoses, 2011. **54**(5): p. e456-62.

230. Driggers, C.M., R.B. Cooley, B. Sankaran, L.L. Hirschberger, M.H. Stipanuk, and P.A. Karplus, *Cysteine dioxygenase structures from pH4 to 9: consistent cys-persulfenate formation at intermediate pH and a Cys-bound enzyme at higher pH.* J Mol Biol, 2013. **425**(17): p. 3121-36.

231. Siakkou, E., S.M. Wilbanks, and G.N. Jameson, *Simplified cysteine dioxygenase activity assay allows simultaneous quantitation of both substrate and product.* Anal Biochem, 2010. **405**(1): p. 127-31.

232. Heron, S., M.G. Maloumbi, M. Dreux, E. Verette, and A. Tchapla, *Method development for a quantitative analysis performed without any standard using an evaporative light-scattering detector.* J Chromatogr A, 2007. **1161**(1-2): p. 152-6.

233. Bantan-Polak, T., M. Kassai, and K.B. Grant, *A comparison of fluorescamine and naphthalene-2,3-dicarboxaldehyde fluorogenic reagents for microplate-based detection of amino acids.* Anal Biochem, 2001. **297**(2): p. 128-36.

234. Hillas, P.J. and P.F. Fitzpatrick, *A mechanism for hydroxylation by tyrosine hydroxylase based on partitioning of substituted phenylalanines.* Biochemistry, 1996. **35**(22): p. 6969-75.

235. Solomon, E.I., T.C. Brunold, M.I. Davis, J.N. Kemsley, S.-K. Lee, N. Lehnert, F. Neese, A.J. Skulan, Y.-S. Yang, and J. Zhou, *Geometric and Electronic Structure/Function Correlations in Non-Heme Iron Enzymes.* Chem Rev., 2000. **100**(1): p. 235-349.

236. Solomon, E.I., A. Decker, and N. Lehnert, *Non-heme iron enzymes: contrasts to heme catalysis.* Proc Natl Acad Sci USA., 2003. **100**(7): p. 3589-94.

237. Costas, M., M.P. Mehn, M.P. Jensen, and L.J. Que, *Dioxygen Activation at Mononuclear Nonheme Iron Active Sites: Enzymes, Models, and Intermediates.* Chem Rev., 2004. **104**(2): p. 939-986.

238. Easson, L.H. and E. Stedman, *Studies on the relationship between chemical constitution and physiological action: Molecular dissymmetry and physiological activity.* Biochem J, 1933. **27**(4): p. 1257-66.

239. Kelley, L.A. and M.J. Sternberg, *Protein structure prediction on the Web: a case study using the Phyre server.* Nat Protoc, 2009. **4**(3): p. 363-71.

240. Himo, F., L. Noodleman, M.R.A. Blomberg, and P.E.M. Siegbahn, *Relative acidities of ortho-substituted phenols, as models for modified tyrosines in proteins.* J Phys Chem A, 2002. **106**(37): p. 8757-8761.

## Biographical Information

Wei Li graduated from Tianjin University with a M.S. degree in Pharmaceutical Science. In college, he worked on method development for Interferon-$\alpha$ expression and purification in Dr. Jinfeng Wang's Lab. In 2009, he became a graduate student in University of Texas at Arlington and joined Dr. Pierce' group. Over the five years since joining the Pierce group, he has been working on mechanistical characterization of a non-heme mononuclear iron metalloenzyme cysteine dioxygenase (CDO). Much of the work has focused on characterizing the steady-state kinetics of this enzyme and active site variants to better understand the role of second-sphere interactions in regulating efficient catalysis. Additionally, spectroscopic measurements were made using electron paramagnetic resonance (EPR) to correlate changes in enzymatic activity and efficiency to the electronic structure of the iron active site.